The structure of laser excited molecules in solution studied by Time Resolved X-ray Diffraction

Manuela Lo Russo

THESE DE DOCTORAT DE L'UNIVERSITE JOSEPH FOURIER

Spécialité

PHYSIQUE

présentée par

M.lle Manuela LO RUSSO

Pour obtenir le grade de

DOCTEUR de l'UNIVERSITE JOSEPH FOURIER

La structure des molécules excitées par laser en solution étudiée par la diffraction rayon-X résolue dans le temps

soutenue devant le jury composé de:

Savo Bratos	Président
Eric Collet	Examinateur
Hans Peter Trommsdorff	Examinateur
Rodolphe Vuilleumier	Rapporteur
Martin Meedom Nielsen	Rapporteur
Michael Wulff	Directeur de thèse

THESE PREPAREE AU SEIN DU LABORATOIRE:
EUROPEAN SYNCHROTRON RADIATION FACILITY - GRENOBLE

The structure of laser excited molecules in solution studied by Time Resolved X-ray Diffraction

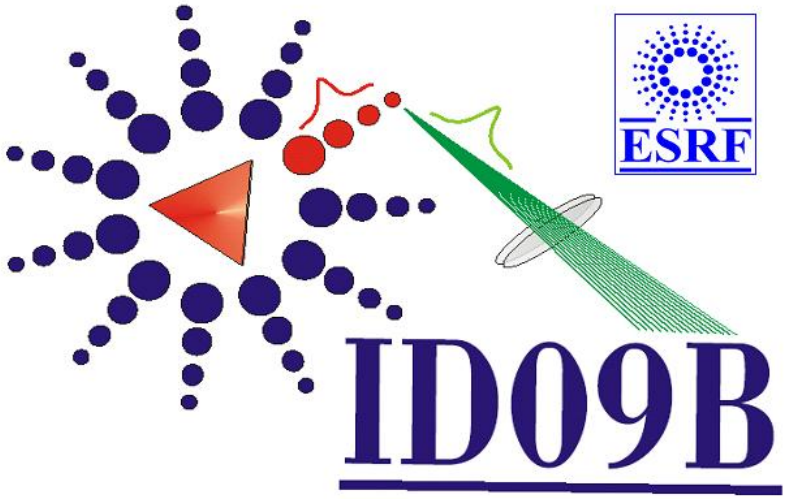

Manuela Lo Russo

"Multa videbis enim plagis ibi percita caecis
commutare viam retroque repulsa reverti
nunc huc nunc illuc in cunctas undique partis.
Scilicet hic a principiis est omnibus error."
Titus Lucretius Carus, De rerum natura, Liber II.

Contents

Abstract

In this thesis we investigate the reaction dynamics of photo-excited Br_2 in CCl_4, HgI_2 and $HgBr_2$ in CH_3OH. We show how it is experimentally possible, by means of Time Resolved X-ray Diffraction, to identify the transient molecular structures formed in solution after the ultrafast laser excitation of the solute molecules and follow in time their rearrangements with a resolution of 100ps. We are able to discriminate the main relaxation and recombination pathways of the reactions, which in liquid phase are determined by the solvent environment: the information contained in the diffraction patterns allows us also to study the solvent response to the heating induced during the solute rearrangements. Supporting the Time Resolved data with Molecular Dynamics simulations, static diffraction data and the experimental study of the pure solvent response to ultrafast heating, the comprehensive reaction dynamics of the molecules in solution spanning from ps up to μs is reconstructed.

Résumé

Dans cette thèse, nous avons étudié la dynamique des réactions de molécules photo-excitées de Br_2, HgI_2 et $HgBr_2$ en solution. La technique de la Diffraction Rayon-X résolue dans le temps nous a permis d'identifier et de suivre en temps, avec une résolution de 100ps, les structures moléculaires qui se forment après l'excitation ultrarapide du soluté par un laser de pompe. Nous avons pu identifier les parcours de recombinaison et relaxation du soluté, déterminés par la présence du solvant: les informations contenues dans les signaux de diffraction nous ont aussi permis d'étudier la réponse du solvant à l'échauffement provoqué par la réorganisation du soluté. Avec l'aide des simulations de la Dynamique Moléculaire, des expériences de diffraction statique, et la mesure de la réponse du solvant au réchauffement impulsif provoqué par radiation infrarouge, nous avons pu reconstruire la dynamique des réactions en solution dans une fenêtre temporelle à partir des ps jusqu'aux μs.

Abstract

Introduction

A short introduction is given to set this thesis work in its scientific background and to state the motivations which drove this project carried out on the ID09B beamline at the European Synchrotron Radiation Facility. The subject of the work is the study of the time dependent structures of small molecules in solution during photo-induced chemical reactions triggered by a femtosecond laser through the Time Resolved X-ray Diffraction experimental technique. This thesis reports the results of the investigations on the relaxation and recombination processes of photo-excited di-atomic and tri-atomic molecules in solution such as Br_2 in CCl_4, $HgBr_2$ and HgI_2 in CH_3OH, with a time resolution of about 100ps. The major aims of this work are summarized in this introduction. Presenting the study of the reaction dynamics of the chosen molecules we will show that thanks to this experimental technique, and a close interplay between experiment and modelling, it is possible to

- follow in time photo-induced chemical reactions in solution with a time resolution of about 100ps;
- identify the transient molecular structures formed in the solution after the excitation and follow in time their rearrangements in terms of concentrations of the species;
- discriminate the main relaxation and recombination pathways of the reactions;
- obtain information on the time scale of the processes;
- study the solvent response to the heating induced during the solute rearrangements.

Introduction

Cette courte introduction veut d'abord rappeler le contexte scientifique dans lequel s'inscrit ce travail de thèse en donnant les motivations qui ont suggéré ce projet mené au sein du laboratoire ID09B à l'ESRF, European Synchrotron Radiation Facility. Le sujet du travail consiste en une étude de l'évolution dans le temps de la structure des petites molécules en solution pendant des reactions chimiques. Les réactions sont provoquées par laser avant que les mouvements atomiques des molécules soient observés par diffraction de rayons-X. Nous allons présenter dans cette thèse les résultats des

investigations conduites sur les photoréactions concernant des molécules di- et tri-atomiques avec une résolution temporelle de 100 picosecondes environ: Br_2 dans CCl_4, $HgBr_2$ et HgI_2 dans CH_3OH. En présentant l'étude des réactions de photodissociation des molécules indiquées, nous allons montrer à l'aide de la technique de la diffraction rayon-X et appuyé sur la modélisation théorique comment il est possible:

- de suivre les mouvements atomiques au cours de réactions photoinduites avec une résolution actuelle d'environ 100ps;
- d'identifier les structures moléculaires transitoires qui se forment dans la solution après l'excitation laser et en suivre l'évolution en observant la concentration de différentes espèces;
- de distinguer le principal parcours de relaxation et recombinaison;
- d'obtenir des informations sur les échelles temporelles des processus;
- d'étudier la réponse du solvant au réchauffement provoqué par la réorganisation structurale du soluté.

Introduction

The intimate need of understanding life and exploring its phenomena and its different expressions, is innate in human beings and it constitutes one of the deepest aspects of its nature.

It could be surprising that in this attempt of explaining the origin of life, twenty-four centuries ago, the Greek philosopher Democritus and his teacher Leucippus introduced the idea of the atom, as the matter's invisible and elementary entity. In Democritus' beliefs, bodies are constituted by aggregations of atoms. A thing comes into being when the atoms that make it up are appropriately associated, and it passes away when these parts disperse. Life and death are thus determined by the atomic motions and by the aggregation and breakup of these particles.

Even though the ancient Greek philosophy introduced atoms and their motions starting from purely philosophical speculations, while, over the centuries, science established a completely different concept of the atom, it is striking and extremely fascinating to see how our scientific knowledges and our comprehension of nature has been, and still is, deeply related to the idea of the atom, to the point that Richard Feynman states that the most important scientific knowledge we possess, summarised in one sentence, is "everything is made of atoms."

Nowadays, the scientific discoveries of the twentieth century made possible to "see" atoms and observe their motion. Indeed, thanks to the properties of X-rays, the new type of radiation first studied by Röngten in 1895, and that Von Laue demonstrated to be electromagnetic waves with wavelengths of the order of the atoms' size, a spatial resolution down to the scale of atomic distance (Å) has been achieved. From this discovery up to the advent, about 20 years ago, of third generation synchrotrons, where intense X-ray beams can be produced, scientific progress has been impressively fast, leading to the possibility of investigating and experimentally observing the aggregations and the different dispositions of atoms in matter.

From the fifties then, the development of fast lasers and fast detectors brought the time resolution down to the scale of the atomic motions (fs).

Combining the two achieved resolutions, femtochemistry introduced the possibility of "the observation of the very act that brings about chemistry, the making and breaking of bonds on their actual time and length scales" as Ahmed H. Zewail stated in his Nobel lecture in 1999. It became possible to reach the dream of "filming" how matter changes and rearranges, how atoms move during chemical reactions, the very fast processes taking place in nature that lie at the basis of life.

Life as we know it, probably evolved in the liquid phase and our bodies are kept alive

by chemical reactions occurring in liquids. This is one of the reasons why solution phase chemistry is such an interesting field of research: there are many fascinating details of the liquid behaviour in general, covering thermodynamics, structure and motion; the majority of life processes takes place in solution, and it cannot be forgotten, these days, also the importance of industrial processes, most of which take place in solution as well.

Combining the pulsed structure and the high intensity of the X-ray beam produced at the European Synchrotron Radiation Facility of Grenoble with an ultrafast optical laser in a pump and probe set-up, the ID09B beamline is designed to be the research facility in this field, with the aim of visualising atomic motions, transient species, structural molecular rearrangements happening during an optically triggered chemical reaction, in real time, both in crystalline and liquid phase.

Joining the ID09B team, under the supervision of Michael Wulff, I had the opportunity of carrying out an experimental studies of the time dependent structures of small molecules in solution during photo-induced chemical reactions triggered by a femtosecond laser.

This thesis reports the result of the investigations on the relaxation and recombination processes of photo-excited diatomic and triatomic molecules in solution such as Br_2 in CCl_4, $HgBr_2$ and HgI_2 in CH_3OH, with a time resolution of about 100ps.

Compared to the deep motivations that drive all research and compared to the richness of the field in which we dare to venture, the present thesis can only be an infinitesimal contribution, focused on consolidating time resolved X-ray diffraction as a fundamental tool to visualise atomic motion in solutions.

Through the study of the reaction dynamics of the chosen molecules we will show that thanks to this technique it is possible to

- follow in time photo-induced chemical reactions in solution with a time resolution of about 100ps;
- identify the transient molecular structures formed in the solution after the excitation and follow in time their rearrangements in terms of concentrations of the species;
- discriminate the main relaxation and recombination pathways of the reactions;
- obtain information on the time scale of the processes;
- study the solvent response to the heating induced during the solute rearrangements.

In particular, the comparisons between similar molecules will allow us to demonstrate the structural sensitivity of the technique.

In this thesis we will start by explaining our motivations in the choice of the molecules, and the physical and chemical processes we aim to understand, before going into details about the theoretical background behind diffraction and into the description of the experimental technique, the used set-up, the data collection strategy. Of course we do not want to make a complete and general overview, which will definitely

go beyond the aim of this work. Instead we will try make it clear, with some theoretical recalls and some experimental details, which information is experimentally accessible from this technique. The tools required to extract this information from the raw data will then be introduced before showing and discussing the achieved results.

Chapter 1

The aim of this work was to perform a systematic study of the reaction dynamics of photo-excited Br_2, HgI_2, $HgBr_2$ in solution, chosen as simple prototypes of di- and tri-atomic molecules. In this chapter we present the physical and chemical processes that will be studied in this thesis. We stress the role played by the solvent in the rearrangements dynamics and the time scales involved in the excitation, dissociation, recombination and relaxation phenomena. We used for these studies single pulse X-ray diffraction with synchrotron radiation, one of the major experimental methods available which allows us a direct observation of temporally varying molecular structures during a photo-induced chemical reaction.

Résumé du chapitre 1

Le but de ce travail a été de développer une étude systématique de la dynamique de réactions de molécules photo-excitées en solution. Br_2, HgI_2 et $HgBr_2$ ont été choisis comme prototype de simples molécules di- et triatomiques. Dans ce premier chapitre, nous allons présenter les processus physiques et chimiques qui seront étudiés dans cette thèse. Une attention particulière est dédiée au rôle joué par le solvant pendant la dynamique de réorganisation structurale des molécules et aussi aux échelles temporelles impliquées dans les phénomènes d'excitation, dissociation, recombinaison et relaxation. La méthode expérimentale de diffraction des rayons X résolue en temps a été appliquée pour ces études, car cette technique nous permet l'observation directe de la variation temporelle des structures moléculaires au cours d'une réaction chimique provoquée par photo-excitation.

Chapter 1

Visualising atomic motions in solution: motivation, state of the art, physical and chemical processes

In their paper entitled "Visualising Chemical Reactions in Solution by Picosecond X-ray Diffraction" [1] from 2004, Plech et al. presented a time-resolved X-ray diffraction study of the recombination of photodissociated I_2 in CCl_4. In this work they state: "The main result of this research, realized with an unprecedented spatial and temporal resolution, is the detection of temporally varying atom-atom distribution functions at times longer than 100 ps. This is the best we were able to do to "film" atomic motions in liquids." They gave indeed, with their results, an important contribution to the great challenge represented by the direct observation of temporally varying molecular structures during a chemical reaction, using single-pulse X-ray diffraction with synchrotron radiation, one of the major experimental methods available to reach this goal. They also affirm: "Although this technique is still in an early stage of development, it has already provided a number of important results [2, 3, 4, 5, 6]. Recent studies of the structural dynamics of the myoglobin complex MbCO are particularly spectacular [7, 8]."
The present thesis project started inspired by this work, with the aim of consolidating the experimental technique of time resolved X-ray diffraction as a fundamental tool to visualise atomic motion in solutions. Other important results have been achieved after the iodine study including the dynamics of more complicated molecular species such as $C_2H_4I_2$ [9].

Nevertheless I want to present here a simple but systematic study of the relaxation and recombination of di and tri-atomic molecules in solution, by time resolved diffraction and establish the computational methods to analyse the data. For this reason, we started with the study of the relaxation process of photoexcited Br_2 in CCl_4, a simple diatomic halide molecule in a non polar solvent, very similar to the above mentioned I_2 in CCl_4. So, by simply making the atomic substitution $I_2 \rightarrow Br_2$, we want to

elucidate which differences we can resolve in these two processes giving immediately the achievable resolution, in time and in space with the state of the art experimental and computational techniques. From these diatomic molecules we will then move on to study the recombination dynamics of two photo-excited triatomic species, HgI_2 and $HgBr_2$ dissolved in CH_3OH. In these cases we will focus more on the role of the solvent. We will show as a result of these studies how it is possible to discriminate between different plausible recombination channels after photo-dissociation, with the particular aim of comparing the diffusion time scales for equivalent atoms and molecules. In order to understand how we can get this information from the experimental data, we will give in the next chapters a brief introduction to laser dissociation of a molecule in solution, the theory of diffraction from a non crystalline sample and the experimental technique before presenting the data, the analysis and conclusions.

1.1 Br_2 in CCl_4

As it has been observed for I_2 in CCl_4, the photodissociation of an I_2 molecule generates a pair of non-bonded atoms. Two outcomes are then possible. The solvent can trap the atoms and force them to recombine in a process that is usually called geminate recombination. Alternatively, the atoms may escape the solvent cage and recombine with other partners: this process is usually called non-geminate recombination. Thanks to the simplicity of this process, the photodissociation and recombination dynamics of diatomic molecules, especially the molecular halogens, have been considered as prototype of a "simple" chemical reactions, and consequently have been a subject of considerable interest for many years [11, 12, 13]. Its simplicity makes this reaction an excellent choice for studying the dynamics of the solvent cage effect, which leads to efficient geminate recombination. Due to the larger optical extinction coefficient of I_2 in the visible (about five times larger than that of Br_2), most of the studies in liquids focused on molecular iodine, whereas only few studies were made on molecular bromine [14, 15, 16]. From the quantum chemical calculations of the molecular wavefunctions and energies we know that Br_2, as well as I_2 does, possesses a large number of electronic states [17, 16], as shown in Fig. 1.1.

The states X, A, A', and B of Br_2 are attractive; the others, including the low-lying state $^1\Pi_{1u}$ are repulsive. Looking at these energy curves we want to describe those processes that can be triggered by a laser pulse and those that can be observed by time resolved X-ray diffraction, stressing the time scales for each phenomenon. In general, when we excite a molecule by an ultrafast (from hundreds of fs to some ps) laser pulse, the molecule breaks into non-bonded atoms or forms a hot molecule with a bigger bondlength. In fact, the bond breakage takes typically 10-30fs after which the molecules predissociates in 100-300fs in the solvent cage. The hot atoms then thermalize with the solvent in 1-2 ps [10, 11, 16]. Through fast geminate recombination, the hot molecules can relax back to the ground state which takes from tenth to hundreds of ps. During the relaxation from excited states to the ground state, the molecule will release heat to the surrounding solvent: at the beginning we have formed only hot spots in the solvent, which cool down through thermal conduction. The temperature

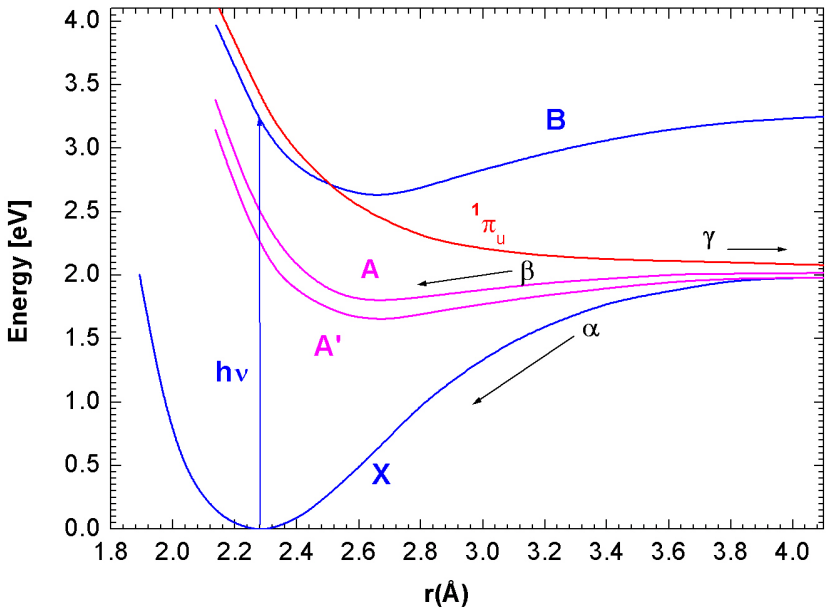

Figure 1.1: Low lying electronic energy surfaces of Br_2: the states X, A/A', and B are attractive, whereas the state $^1\Pi_{1u}$ is repulsive. The process α, β, and γ denote vibrational cooling along the X potential, geminate recombination through the state A/A', and nongeminate recombination, respectively.

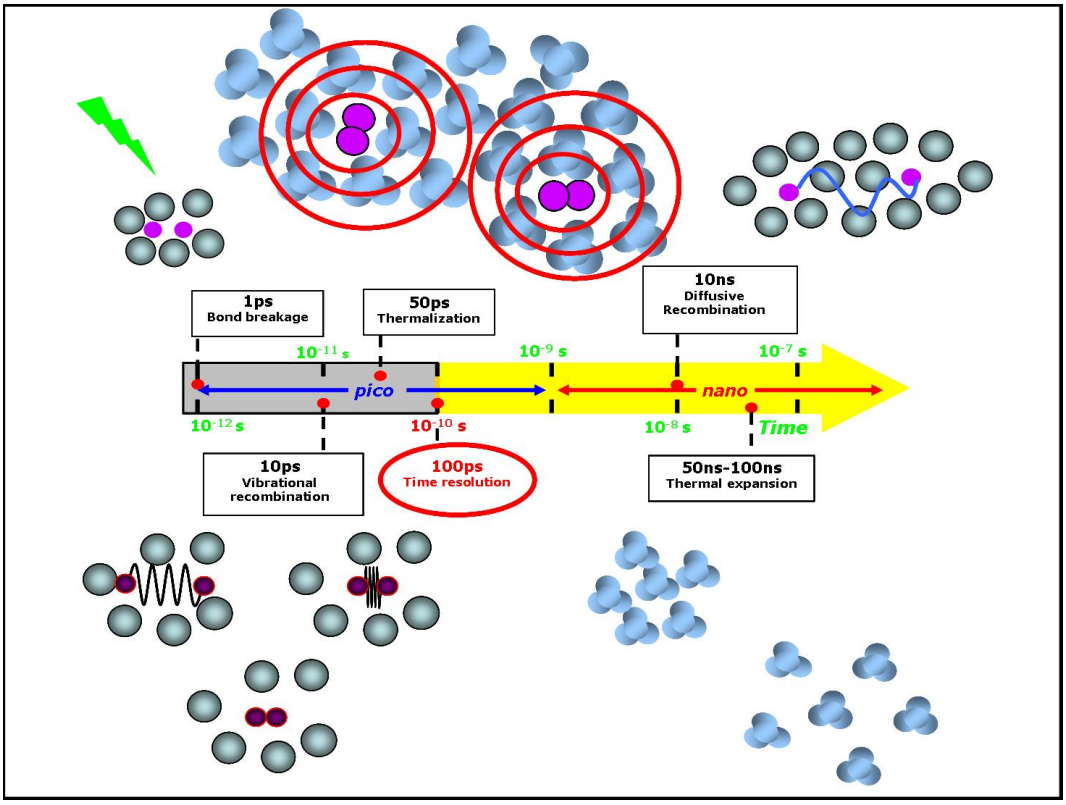

Figure 1.2: Schematic and naïve representation of the processes following the photoexcitation of a molecule in solution and their time scales.

distribution in the solvent is thus highly non uniform just after predissociation, but becomes locally uniform in about 50 ps at typical solute concentrations. Only after this time scale from the excitation it is meaningful to talk of temperature, i.e. when a new thermal equilibrium in the system has been reached, at a higher temperature. Our time resolution is limited to ∼100 ps, from the temporal width of the X-ray pulse. This means that we are blind to bond breakage dynamics and that the recombination dynamics and the thermal smearing in the solvent are on the borderline of being resolved. What we can determine, once the thermal equilibrium is reached, is the atomic composition and structure of the reaction products, and to follow the diffusive recombination (tenth of ns) of the possible transient structures formed in solution, studying how the concentration of these species evolve with time until the end of the reaction, understanding if it is a completely reversible process or not and how the system then changes its density due to thermal expansion, on the scale of time of the pressure wave propagation in the solvent (typically hundreds of ns), in order to accommodate the new temperature in a new volume.

In the specific case of Br_2 in CCl_4 after the excitation with a 150 fs, 400 nm laser pulse, hot bromine Br_2^* molecules, with a "bond length" of more than 4Å, are formed in less than 1 ps. After the excitation the Br_2^* molecules start to release energy to the solvent while relaxing into the ground state. As we already mentioned, this process can take place in two different ways. The solvent molecules can trap the Br atoms and hereby foster the formation of hot Br_2^* in the X^* state, which in turn relaxes via

vibrational cooling ($\tau_\alpha \sim 140ps$), or form Br_2^* molecules in the quasi stable state A/A' which eventually relaxes into the ground state in 5.5ns ($\tau_\beta \sim 5.5ns$). In these two cases, the original partners recombine directly, a process known as geminate recombination. But in some Br_2^* molecules, the Br atoms escape the solvent cage; i.e. they dissociate completely. These Br atoms recombine with new partners in a diffusive way, which takes much longer than direct recombination, $\tau_\gamma \sim 25ns$ [15, 18, 19]. As we already said, due to the important role of the solvent in the recombination processes, chemical reactions in solution are quite different and more complicated from those in the gas phase. The molecular properties and chemical reaction mechanism can change considerably from the gas to the liquid phase. Unlike the gas phase reaction, in which the geminate recombination of I_2 and Br_2 is impossible, geminate recombination in solution is greatly enhanced by the solvent cage. It is thus essential to investigate the nature of the solute/solvent interaction. As we will see in detail later, the diffraction measurements in our experiments probe these effects through the solute/solvent cross term, which can be expressed through atom-atom pair distribution functions $g_{ij}(r,\tau)$, where i is an atom in the solute and j is an atom in the first coordination shell [20]. In the study of the recombination process of Br_2 in CCl_4 that we will present, X-ray diffraction at high energy and Molecular Dynamics simulations will be used to measure and predict the cage structure. By means of the time-resolved X-ray diffraction technique our aim in the study of this system is to measure directly the temporally varying molecular structures as it was done for I_2 in CCl_4 and determine in this way the relaxation mechanism. We will report the experimental details, the data analysis and the Molecular Dynamics simulations on this system, the results and the perspectives to get more information about the chemical process. Let us try very briefly to illustrate what we can learn and how, before going into all the details in the next chapters: at any given time delay $\Delta\tau$ between the laser pump pulse used to trigger the dissociation and the X-ray pulse used to probe the structure, we measured the diffraction patterns in pairs "with" and "without" laser. From these patterns we got the (radially integrated) difference curves $\Delta S(q,\tau)$ which are then Fourier transformed into real space as $\Delta S[r,\tau]$, [20]. The $\Delta S[r,\tau]$ curves that we will show can be considered a one-dimensional film of the change in atom-atom pair distributions for the global system, solute and solvent, during the recombination process.

1.2 HgI_2 and $HgBr_2$ in CH_3OH

After the natural choice of Br_2 in CCl_4 as simple diatomic system to study and compare to the previously studied I_2 in CCl_4, we decided to investigate the recombination process during a photo-induced chemical reaction of a triatomic molecule in solution. The first triatomic molecule chosen for our study was HgI_2 dissolved in CH_3OH.

In 2000, the first dissociation signal of HgI_2 in CH_3OH was observed with the weak monochromatic X-ray beam available at that time on ID09B beamline at the ESRF [21]. In Fig1.3 we show a comparison between this signal and the signal measured with polychromatic beam in this work.

Of course we will discuss in detail the meaning and the information of the difference

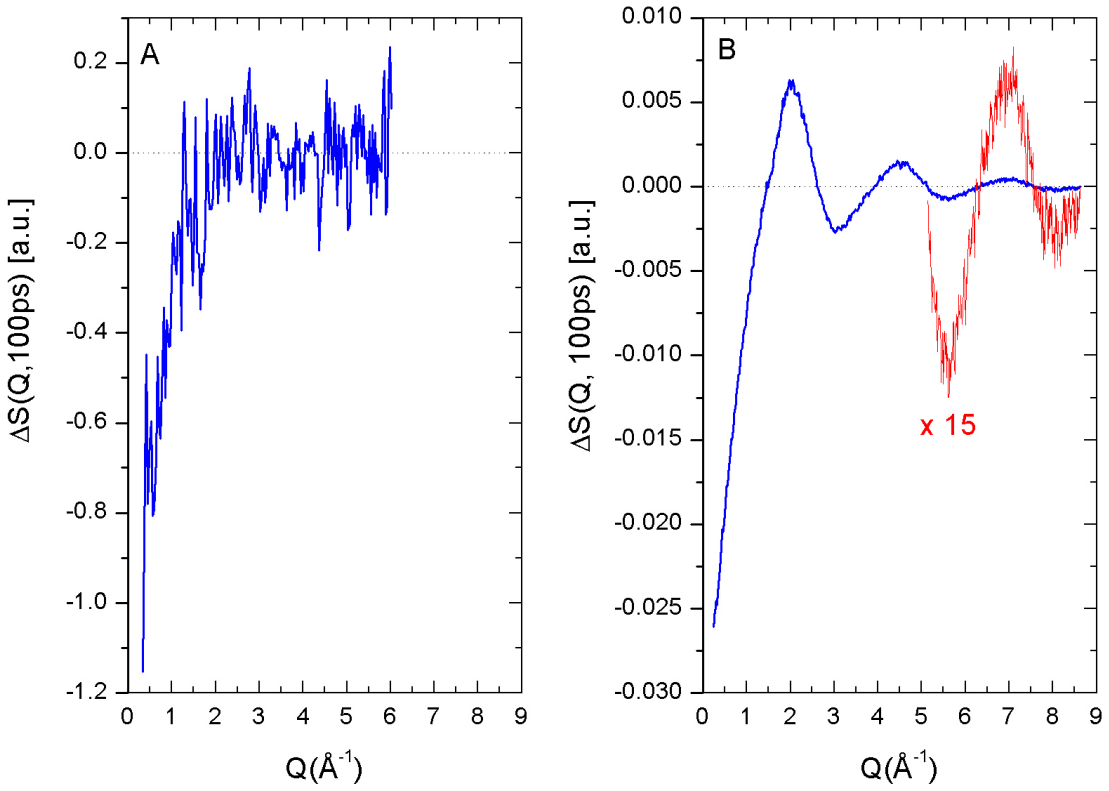

Figure 1.3: On the left (panel A) the photo signal from HgI_2 as recorded in year 2000. The experiment was done with monochromatic beam at 16.5keV from the in-air undulator U20 at 16.7mm gap. The flux was 3×10^8ph/s. The curve is the average of 20 signals collected with 10min exposures each. On the right (panel B) the same curve but recorded with the 3% bandwidth polychromatic beam at 18.2keV from the in-vacuum undulator U17 at 9mm gap. The flux was 5×10^{11}ph/s. The curve is the average of 40 repetitions collected with 10s exposures each.

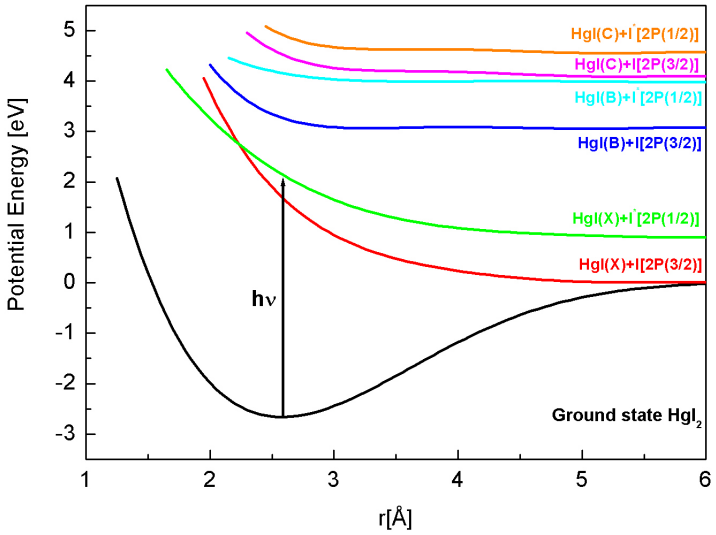

Figure 1.4: Schematic of the one-dimensional PES of HgI_2 dissociation [27].

signals, but this picture demonstrates the progresses made with polychromatic beam since 2000. The technical developments achieved during the years allow us now to obtain experimental signals from which we can clearly identify the photodissociation and follow in time the structural rearrangements during the recombination process.

In general, a rich literature about mercuric halides is available. These molecules have been studied by photoabsorption and emission techniques for more than a hundreds years [22] largely because of their nature as prototypical linear triatomic molecules. Their structures have also been investigated in the liquid phase by X-ray diffraction and Raman studies [23]. The discovery of their electronic-transition lasing action [24, 25] together with their potential as high-power blue-green laser system, renewed the interest in the structures of this class of molecules. In particular, the dissociation of HgI_2 has been object of many femtosecond-resolved spectroscopic studies in the gas phase [26, 27, 28]. In their work, Zewail and coworkers [27] using laser induced fluorescence focused on the two-body reaction $HgI_2 \rightarrow HgI + I$ by monitoring the HgI formation up to 3ps. In Fig. 1.4 we show the schematic plot of the one-dimensional PES of HgI_2 dissociation as reported in [27]. By means of time-resolved mass spectrometry [28] two and three-body dissociation ($HgI_2 \rightarrow Hg + I + I$) were observed and characterised. Concerning the solution phase, studies on this molecule in ethanol were carried out by Hochstrasser and co-workers, who investigated the solvation dynamics at delays up to 15ps using femtosecond absorption spectroscopy. In their works [29, 30, 31], they pay special attention to the vibrational relaxation process and rotational dynamics of the impulsively generated HgI molecules. What emerged from these solutions studies, in spite of the important investigations already made, was the lack of a comprehensive reaction mechanism in the solution phase spanning from ps up to μs. In the recently published paper, "Spatiotemporal reaction kinetics of an ultrafast photoreac-

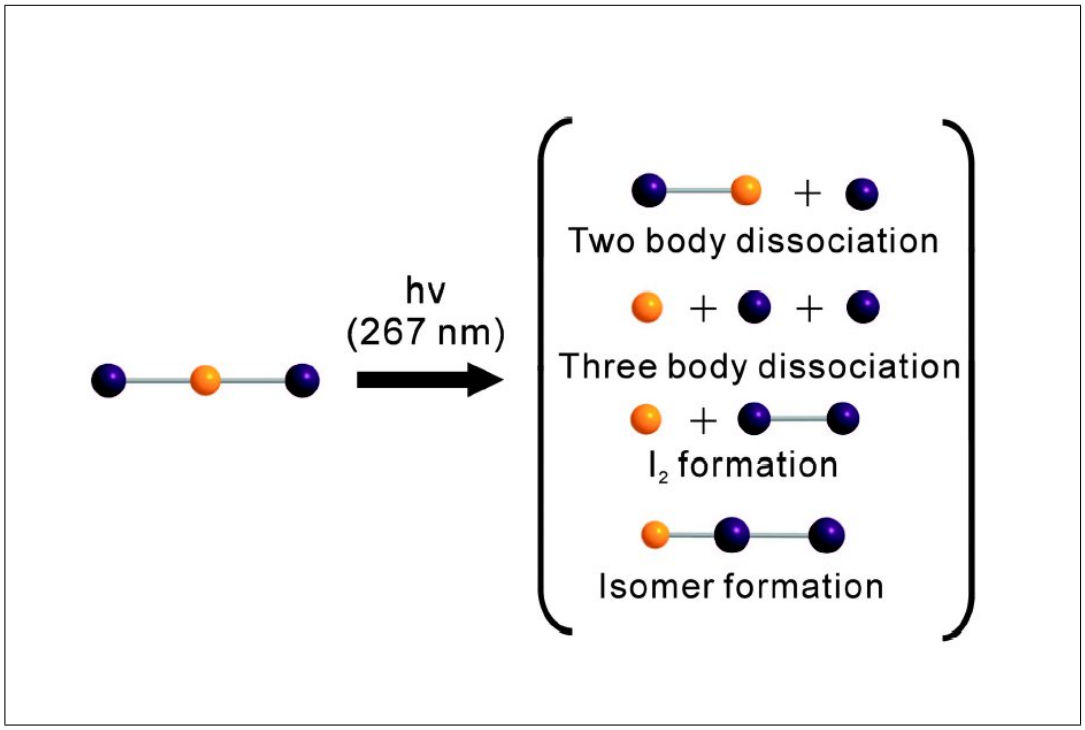

Figure 1.5: Putative reaction channels after photodissociation of HgI_2 in solution.

tion pathway visualised by time-resolved liquid X-ray diffraction" [32] we showed how time-resolved X-ray diffraction can now provide this missing information directly. We will present and discuss these results here, in which I was particularly involved with the Molecular Dynamics simulations. In this investigation we needed first of all to discriminate between different plausible dissociation pathways upon ultra-violet excitation. Indeed, HgI_2 in solution can dissociate in four ways. Considering the time resolution of our technique as we explained before, we have the resolution power to discriminate between two-body dissociation, $HgI_2 \rightarrow HgI + I$, and three body dissociation, $HgI_2 \rightarrow Hg + I + I$. A dissociation into $Hg + I_2$ could also be expected, as well as the formation of a $HgI - I$ isomer. In Fig.1.6 a schematic representation of the possible dissociation channels. Thanks to quantum chemical calculations (later on we will give a simple explanation of this very powerful computational method), the photodissociation energies for putative transitions can be calculated as displayed in Fig. 1.6.

We will also describe later on how the structural parameters were obtained, but point out here that we can exclude the possibility of three body dissociation with $267nm$ radiation (448.2 kJ/mol). This preliminary information will drive our analysis in order to understand which species are actually formed after the dissociation and then follow their recombination in time, up to μs in order to describe the complete reaction pathway and underlining the correlation between transient structures and solvent energetics. The next natural step after having determined the reaction pathway of HgI_2 in CH_3OH, is to make the substitution $I \rightarrow Br$ and study $HgBr_2$ molecules dissolved in the same solvent. This looked indeed like an obvious continuation of the

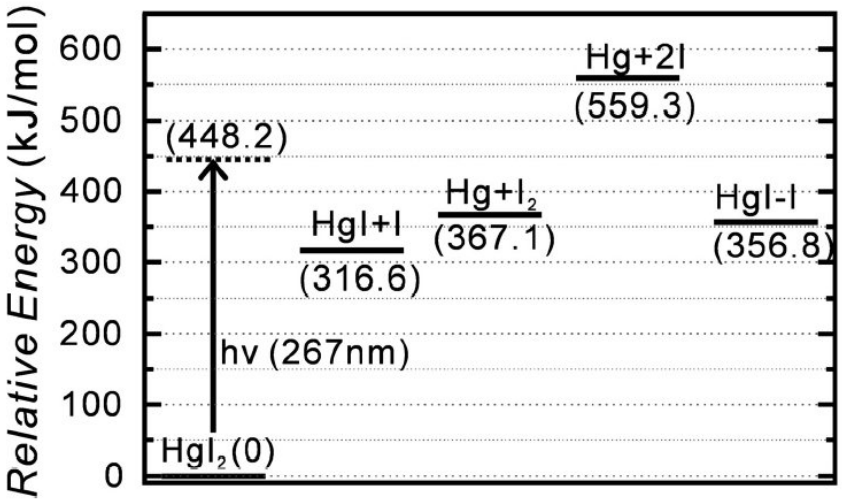

Figure 1.6: Relative energies of the dissociation products of HgI_2 in solution.

study, which can show how the differences in size and Z number of atom can influence the photodissociation and recombination pathways. As for HgI_2, many investigations have been performed on $HgBr_2$, both from a theoretical and an experimental point of view. As mentioned earlier the photodissociation of the mercuric halides have been studied for nearly 100 years. Wadt [33] and Maya [34], summarised respectively much of the theoretical and experimental work on the photodissociation of mercuric halides. Absorption spectroscopy and laser induced fluorescence methods have been used to probe the vibrational distributions of the dissociation products of HgI_2 and $HgBr_2$ [35], and Hochstrasser and co-workers measured also the solvation dynamics of $HgBr_2$ in solution by femtosecond absorption spectroscopy [36], with the aim to describe the structural and dynamical properties of solvation. In this sense the photolysis of mercuric dihalides is particularly interesting because it involves large changes in the charges associated with the three atoms: for example, the dissociated atom, which has a substantial partial charge in the triatomic state [37] becomes neutral after dissociation. Using time resolved X-ray diffraction, our aim was, once again, to determine the dominant photo-dissociation pathway of excited $HgBr_2$ in CH_3OH and then follow the recombination from 100ps to 1μs to determine the reaction mechanism in the solution and compare it with HgI_2 in CH_3OH. In the following figures, Fig.1.7, 1.8, we show the plausible dissociation channels as well as the photodissociation energies for each reaction channel as determined by DFT quantum chemical calculations for $HgBr_2$ in solution.

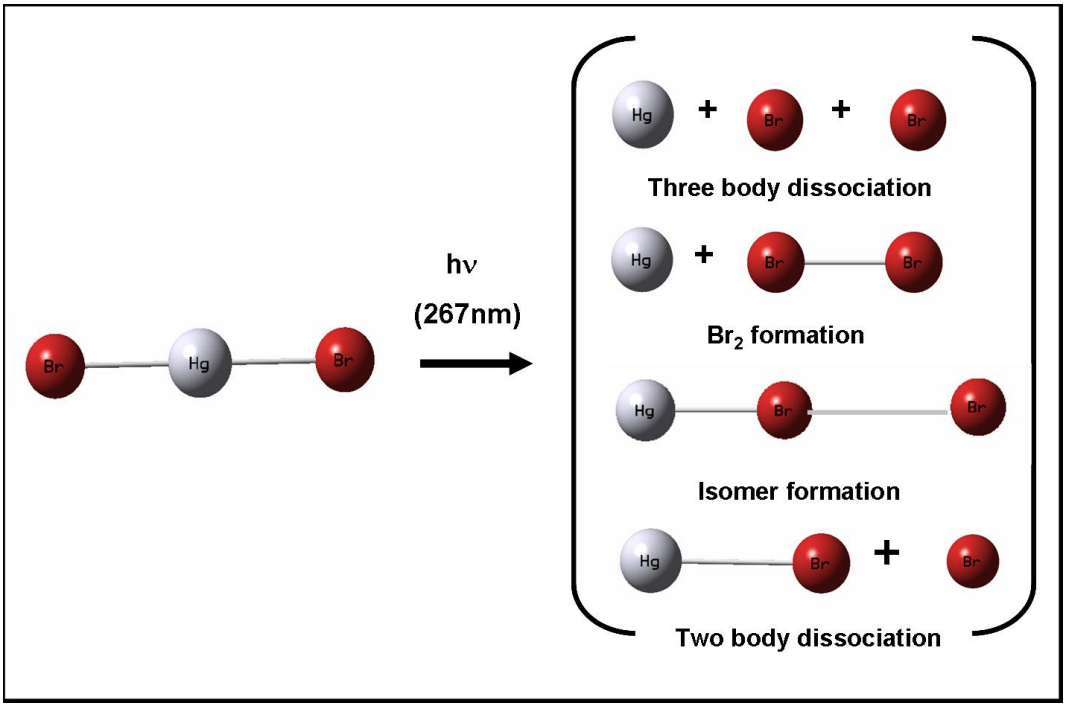

Figure 1.7: Putative reaction channels after photodissociation of $HgBr_2$ in solution.

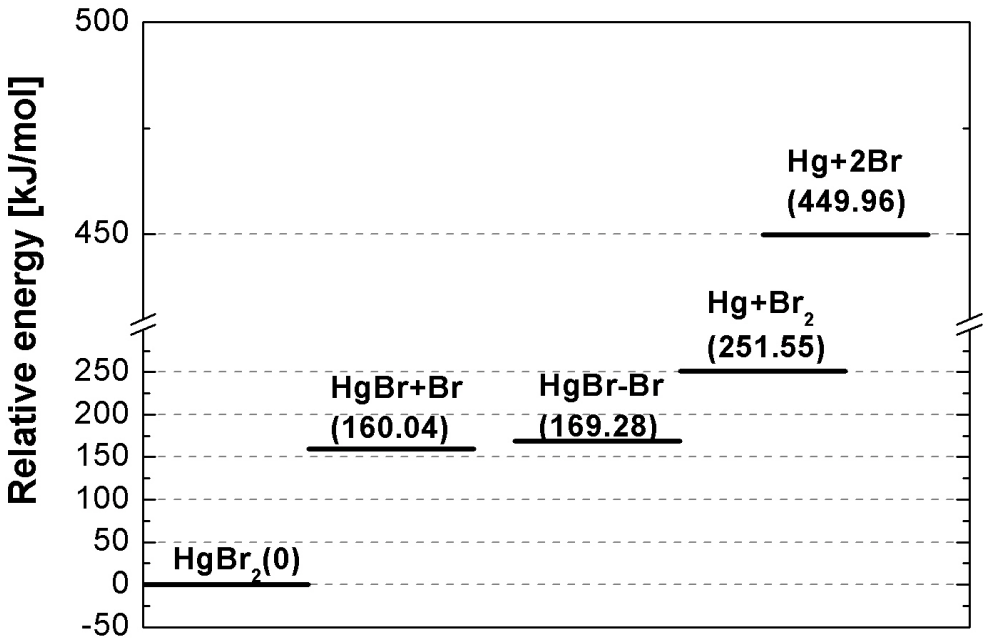

Figure 1.8: Relative energies of the dissociation products of HgI_2 in solution.

1.3 Conclusions

The aim of this chapter was to introduce the physical and chemical processes that I studied during my PhD. And I stressed how this work started from the pump and probe experiment on I_2 in CCl_4 by Plech et al. [1] which allowed to monitor the recombination of molecular iodine dissolved in CCl_4 in real time. As a natural continuation of this study, I became interested in looking at Br_2 in CCl_4 as a straightforward comparison and consolidate the experimental technique and the data analysis needed to determine the temporally varying atom-atom pair distribution function. Although more complicated molecules were studied following I_2 in CCl_4 [9], the aim of this work was to present a simple but systematic study of the relaxation and recombination of small photo-excited molecules in solution. To better evaluate the possibilities of the technique we turned our attention to slightly more complex triatomic molecules, HgI_2 and $HgBr_2$ dissolved in methanol.

Chapter 2

In this chapter a brief overview of the basic principles of X-ray diffraction is given, to clarify how it is possible, using this technique, to obtain direct structural information on a liquid. The principles of the pump and probe technique are then presented and the experimental difference diffraction signals containing information on the structural rearrangements of a photo-excited solute in solution are discussed. The specific experimental set-up on beamline ID09B at the ESRF, where this work has been performed, is also described.

Résumé du chapitre 2

Une brève introduction aux concepts fondamentaux de la théorie de la diffraction des rayons-X est fournie dans ce chapitre, dont le but est de montrer comment il est possible d'obtenir des informations directes sur la structure d'un liquide grâce à l'application de cette technique. La deuxième partie de ce chapitre, après l'introduction théorique se concentre sur les aspects expérimentaux de nos études: d'abord avec l'explication des principes de la méthode de pompe-sonde et ensuite avec les dispositifs utilisés sur la ligne de lumière ID09B à l'ESRF et la description de l'aire expérimentale.

Chapter 2

Time Resolved X-Ray Diffraction on Liquids

The aim of this chapter is to clarify how it is experimentally possible to collect data containing direct information on the structural changes of photo-excited molecules in solution during a chemical reaction, using time resolved X-ray diffraction and reaching a time resolution of about 100 picoseconds. For this purpose we will present first of all a brief overview of the basic principles of X-ray diffraction, to see how, through X-ray diffraction signals, direct structural information can be obtained from a liquid. I will then discuss the principles of the pump and probe technique and show how we can obtain an intuitive picture of the structural changes in real space. An in depth explanation of the data analysis and the ensuing results and interpretations will be done in the following chapters. Here I will focus on the experimental set-up on beamline ID09B at the ESRF which allowed us to collect the data and, in conclusion, I will summarise the experimental parameters used in the studies discussed in this work.

2.1 Basic principles of the X-ray Diffraction Theory

In this section I will briefly recall the basic principles of X-ray diffraction and summarise the basic equations. Without pretending to give an exhaustive review on this topic, I want to stress the meanings of the diffraction phenomenon, to understand the structural information we can obtain from diffraction spectra and establish the tools needed to extract it, linking directly theory and experiment.

2.1.1 X-ray diffraction

In general when an X-ray beam impinges on an atom two processes may occur: the beam may be absorbed with the ejection of electrons, or the beam will be scattered. We can first think of the scattering process in terms of classical theory: the primary beam is an electromagnetic wave with electric vector varying sinusoidally with time and directed

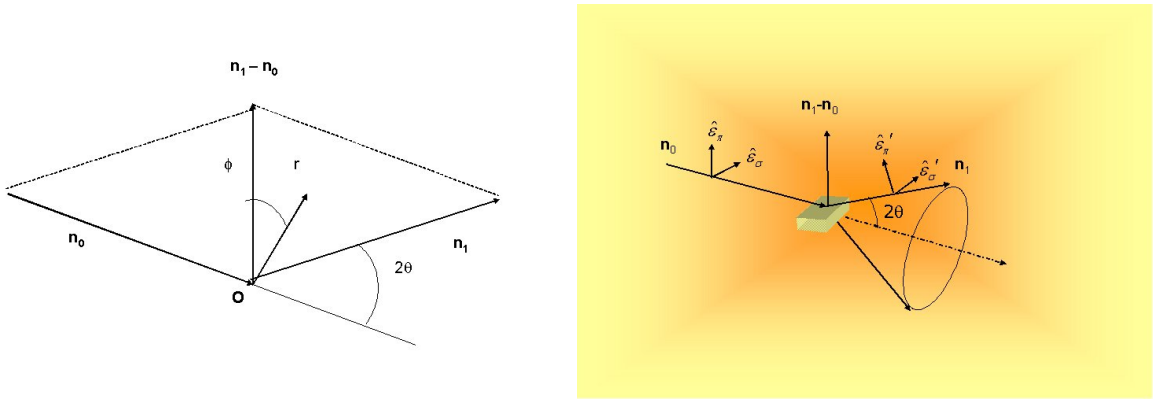

Figure 2.1: Simple drawing of the scattering geometry: on the left the relation between the $\vec{n_i} - \vec{n_0}$ vector and the vector $\vec{r}$ for an atom centred at O. On the right the horizontal and vertical polarisation unity vectors $\vec{\epsilon_\sigma}$ and $\vec{\epsilon_\pi}$ are also visualised: our beam is 99.6% polarised in the orbit plane.

perpendicular to the direction of propagation of the beam. This electric field exerts forces on the electrons of the atom producing accelerations of the electrons. Following classical electromagnetic theory, an accelerated charge radiates. This radiation, which spreads out in all directions from the atom, has the same frequency as the primary beam, and it is called scattered radiation.
Let us consider an X-ray beam of wavelength λ_X falling on an atom with one electron in its ground state. If the frequency of the beam is higher than all the resonance frequencies of the atom, then the scattered intensity S at a certain distance from the atom has two components [38, 39]. The first one involves only the ground state wavefunction Ψ_0. For a one-electron atom

$$S(\vec{Q}) = S_0 r_e^2 P \mid \int \mid \Psi_0(\vec{r}) \mid^2 \exp\left(i\vec{Q}\cdot\vec{r}\right) d^3\vec{r} \mid^2 \tag{2.1}$$

with $\vec{Q} = \frac{2\pi}{\lambda_X}(\vec{n_i} - \vec{n_0})$ where $\vec{n_i} = \frac{\vec{Q_i}}{\|\vec{Q_i}\|}$ is the unity vector in the incident direction and $\vec{n_0}$ is the unity vector in the observation direction. The norm of $\vec{Q}$ is given by $Q = \frac{4\pi \sin\theta}{\lambda_X}$ with 2θ angle between $\vec{n_i}$ and $\vec{n_0}$.
$r_e^2 = \frac{e^2}{4\pi\epsilon_0 m_e c^2} = 2.82 \cdot 10^{-15} m$ is the classical electron radius.

Following the derivation of the Thomson scattering cross section [39], P is the polarisation factor which depends on the X-ray source and can be written as

$$P = \begin{cases} 1 & \text{synchrotron: vertical scattering plane} \\ cos^2\psi & \text{synchrotron: horizontal scattering plane} \\ \frac{1}{2}(1 + cos^2\psi) & \text{unpolarised source} \end{cases}$$

with ψ being the angle between an observation point X at a distance R from the radiation source and the direction of the incident beam as shown in Fig.2.2. The polarisation factor for a synchrotron source arises from the fact that the electrons in a synchrotron orbit in the horizontal plane. It follows that their acceleration is also in

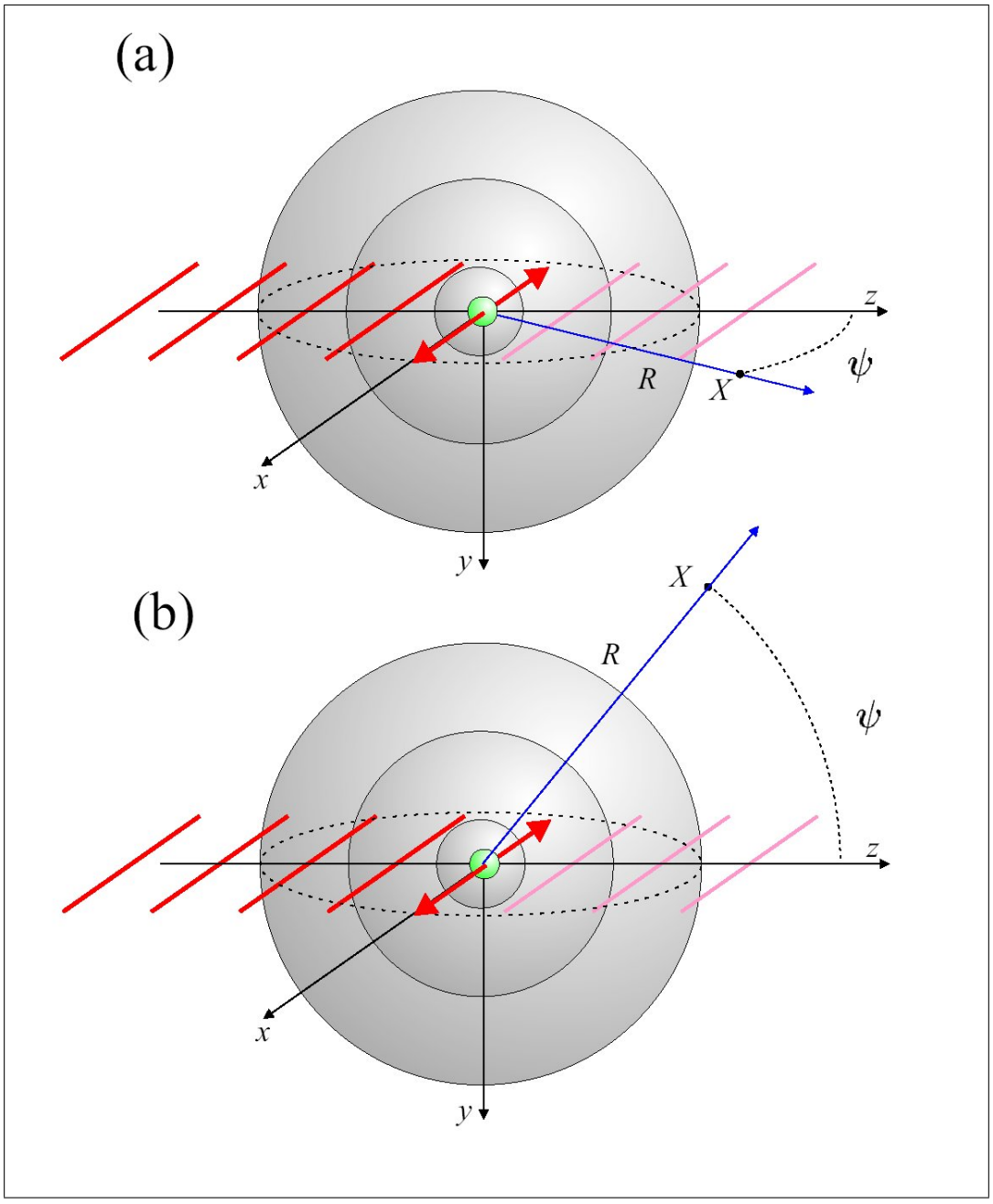

Figure 2.2: The classical description of the scattering of an X-ray by an electron. The electric field of an incident plane wave sets an electron in oscillation which then radiates a spherical wave. The incident wave propagates along the z axis and has its electric field polarised along x. The wave crests of the incident wave lie in between those of the scattered spherical wave because of the 180° phase shift in Thomson scattering. The radiated field can be calculated depending on the observation point X and two different cases exist: (a) the point X lies in the same plane as the polarisation of the incident wave, and the observed acceleration has to be multiplied by a factor $cos\psi$; (b) the observation point X is in the plane normal to the incident polarisation and the full acceleration of the electron is seen at all scattering angles ψ [39].

the plane and hence the emitted X-rays are linearly polarised in the horizontal plane but only if viewed in the orbit plane; out of this plane the polarisation is elliptical.

$\mid \Psi_0(\vec{r}) \mid^2$ represents the probability density of finding the electron in the ground state in the position $\vec{r}$, that we can indicate as $\rho(\vec{r})$.
The scattered intensity is associated with a wave of the same frequency as the incident wave: it gives the coherently scattered intensity, and we can rewrite the previous equation as

$$S_{coh}(\vec{Q}) = S_0 r_e^2 P \mid \int \rho(\vec{r}) \exp(i\vec{Q} \cdot \vec{r}) d^3\vec{r} \mid^2 . \tag{2.2}$$

The term $\int \rho(\vec{r}) \exp(i\vec{Q} \cdot \vec{r}) d^3\vec{r}$, is the atomic form factor $f(\vec{Q})$, which is of fundamental importance in the theory of diffraction, being the Fourier transform of the charge density. The coherent intensity is consequently proportional to the squared atomic form factor of the scattering atom.
By assuming spherical symmetry for the electronic charge distribution it is possible to obtain a simple expression for $f(\vec{Q})$:

$$f(\vec{Q}) = f(Q) = \int_{r=0}^{+\infty} \exp(iQr\cos\phi)\rho(r)2\pi r^2 \sin\phi d\phi dr \tag{2.3}$$

In this approximation, $f(Q)$ is a real function, depending only on Q. Calling Z the number of electrons in the atom, $\rho(r)$ is the density associated with all the electrons in the atom, such that

$$\int \rho(\vec{r}) d\vec{r} = Z$$

This integral gives the value:

$$f(\vec{0}) = Z$$

Dividing eq.2.2 by $S_0 r_e^2 P$ we obtain the scattered intensity expressed in so-called electron units (e.u.). In this units

$$S_{coh}(\vec{0}) = Z^2.$$

The second component of the scattered intensity contains a product of the ground state wavefunction Ψ_0 and the excited states wavefunction Ψ_n. For the simple case of one atom with one electron it can be written as

$$S(\vec{Q}) = \sum_{n \neq 0} S_0 r_e^2 \left(\frac{\omega_X - \omega_{0,n}}{\omega_X} \right) P \int \Psi_0(\vec{r}) \Psi_n^*(\vec{r}) \exp(i\vec{Q} \cdot \vec{r}) d^3 r \tag{2.4}$$

with ω_X frequency of the incident wave and $\omega_{0,n}$ frequency related to the transition from the ground state towards the $n-th$ state of the atom. Every term of the sum is associated with a scattered wave with a frequency $(\omega_X - \omega_{0,n})$ and random phase, and it corresponds to incoherent (or Compton) scattering. We can call this intensity $S_{inc}(\vec{Q})$. When many atoms undergo Compton scattering, the incoherence of these scattering events makes the total intensity equal to the sum of the individual intensities and the total intensity does not depend on the relative positions of the atoms. Thus, Compton

scattering does not contain structural information. It is nevertheless always present in the experimental signal as a background that increases at high scattering angles and we will need to model it [41, 40] in order to normalise the difference signals to the total signal for the solution. On the other hand, we denote the coherent scattering from a multi-atomic system *diffraction*, to stress the interference in the process, which can provide us with structural information.
Generalising to a multi-atomic system, $\rho(\vec{r})$ will be the total electronic density of the sample. In order to obtain the coherent scattered intensity for a multi-atomic system (and then in particular for a liquid) we have to consider, first of all, a fundamental property for the theory of diffraction: atomic localisation. In general, the atomic distances are bigger than the radius of the electronic clouds of the atoms; this means that the atomic distances are well defined and the electronic density can be written as a convolution of the electronic atomic density $\rho_i^{atom}(\vec{r})$ of the atom i with the position of the $i-th$ atom $\delta(\vec{r}-\vec{r_i})$:

$$\rho(\vec{r}) = \sum_i \delta(\vec{r}-\vec{r_i}) \otimes \rho_i^{atom}(\vec{r}) = \sum_i \int \delta(\vec{r'}-\vec{r_i})\rho_i^{atom}(\vec{r'}-\vec{r_i})d^3r'. \tag{2.5}$$

Fourier transforming this expression we get

$$FT(\rho(\vec{r})) = \sum_i TF(\delta(\vec{r}-\vec{r_i}))TF(\rho_i^{atom}(\vec{r})). \tag{2.6}$$

The second term in the product $TF(\rho_i^{atom}(\vec{r}))$ is the atomic form factor of the atom i, and the first term gives $\exp(i\vec{Q}\cdot\vec{r_i})$. Thus, the coherent scattered intensity can be written, in electron units, recalling eq.2.2 as

$$S_{coh}(\vec{Q}) = \mid \sum_i \exp(i\vec{Q}\cdot\vec{r_i}) f_i(\vec{Q}) \mid^2, \tag{2.7}$$

and the sum over all the atoms i can then be expressed as a sum over atomic species α, such that

$$S_{coh}(\vec{Q}) = \mid \sum_\alpha \sum_{i_\alpha} \exp(i\vec{Q}\cdot\vec{r_{i_\alpha}}) f_\alpha(\vec{Q}) \mid^2, \tag{2.8}$$

with $f_\alpha(\vec{Q})$ atomic form factor of the atoms of type α. It is so possible to define the (partial) structure factor of the atom of α type as

$$F_\alpha(\vec{Q}) = \sum_{i_\alpha} \exp(i\vec{Q}\cdot\vec{r_{i_\alpha}}) = \sum_{i_\alpha} TF(\delta(\vec{r}-\vec{r}_{i_\alpha})), \tag{2.9}$$

from which

$$S_{coh}(\vec{Q}) = \mid \sum_\alpha F_\alpha(\vec{Q}) f_\alpha(\vec{Q}) \mid^2 . \tag{2.10}$$

For $\vec{Q} \to \vec{0}$ we find the square of the total number of electrons in the system

$$S_{coh}(\vec{0}) = \left(\sum_{\alpha} N_{\alpha} Z_{\alpha} \right)^2$$

with $N_\alpha = F_\alpha(\vec{0})$ number of the α atoms and $Z_\alpha = f_\alpha(\vec{0})$ number of electrons of these atoms.

2.1.2 Debye scattering: X-ray diffraction from a gas of molecules

Having summarised the formulas describing the intensity of the scattered X-ray beam from an ensemble of atoms we shall now focus our attention on the diffraction from an ensemble of independent molecules [38, 39]. As the ensemble is globally disordered one could think that the interferences between the scattered waves were random as the positions of the atoms in the system, which would result in a structure factor equal to 1. But in reality the inside structure of the molecule leads to constructive interferences. The scattering from independent molecules is (considering eq.2.10):

$$S_{coh}(\vec{Q}) = \mid \sum_i F_i(\vec{Q}) f_i(\vec{Q}) \mid^2 = \mid \sum_i \exp(i\vec{Q} \cdot \vec{r}_i) f_i(\vec{Q}) \mid^2 = \sum_{i,j} f_i(\vec{Q}) f_j^*(\vec{Q}) \exp(i\vec{Q} \cdot (\vec{r}_i - \vec{r}_j)). \tag{2.11}$$

Given the isotropy of the molecular orientations, this equation can be integrated over all the possible directions giving

$$S_{coh}(\vec{Q}) = \sum_{i,j} f_i(\vec{Q}) f_j^*(\vec{Q}) \frac{\sin Q r_{i,j}}{Q r_{i,j}} \tag{2.12}$$

being $r_{i,j} = \parallel \vec{r_i} - \vec{r_j} \parallel$.
Eq.2.12 is the Debye equation, the fundamental equation in the theory of diffraction from dilute molecules. It is worth at this point of our discussion to spend some comments on it. First of all we note that the scattering decreases as $1/r_{i,j}$, i.e. relatively slowly (electron diffraction decreases as $1/r_{i,j}^5$). The diffraction signal can thus sense atoms relatively far apart. Secondly it must be stressed that it is possible in this equation to substitute the atomic form factors with molecular structure form factors: in that case $r_{i,j}$ will be the distance between i and j entities and the Debye formula will give the interference coming out from waves scattered from the considered entities (groups of atoms, groups of molecules). We can split the Debye equation as a sum of two terms, one for $i = j$ and the second one for $i \neq j$,

$$S_{coh}(\vec{Q}) = \sum_i f_i^2(\vec{Q}) + \sum_{i \neq j} f_i(\vec{Q}) f_j^*(\vec{Q}) \frac{\sin Q r_{i,j}}{Q r_{i,j}} \tag{2.13}$$

and observe that when Q becomes big enough, the second term becomes negligible compared to the first: the diffracted intensity at high Q does not include anymore information about the $r_{i,j}$ distance. The term $\frac{\sin Qr_{i,j}}{Qr_{i,j}} \rightarrow 0$ when $Q \rightarrow \infty$: we can consider this as the atomic limit, which means that the scattered intensity from a condensed phase system converges towards the atomic phase intensity $\sum_i f_i^2(\vec{Q})$ at high Q.

2.1.3 Structural information contained in the diffracted intensity

The description of the structure of disordered systems like liquids requires a statistical definition of the spatial correlations between the atoms in the system. In the case of ordered systems, like crystals for example, the molecular structure is easily defined and the geometry is completely known if the positions of all the atoms are given. The amount of data required is limited due to the symmetry of the crystal. For a disordered system this approach is not valid anymore and a virtually infinite amount of data is required to give the positions of all the atoms in the system. In addition, the fact that all the atoms are continuously moving complicates the situation further. Only a statistical description of the geometry, in terms of probability, is valid and even if it does not define the structure of the liquid completely, it provides a picture of its local structure, which is sufficient for many purposes. It consists in defining the so-called site-site distribution functions (or partial Radial Distribution Functions RDF) $g_{\alpha,\beta}(r)$ that represent the probability of finding an atom α in the system at a distance r from an atom β in the origin of the coordinate system. This function can be defined starting from pure statistical mechanics, from which it can also be shown how, using the $g_{\alpha,\beta}(r)$ function, it is possible, in the case of two body interactions, to obtain the equation of state and important thermodynamical properties of the system [43]. We want to discuss here how the experimentally measurable diffraction intensities are linked to these functions, to clarify the structural information that can be extracted from the diffraction data.

Let's now express the diffraction from a liquid through its $g_{\alpha,\beta}(r)$ functions. If we consider eq.2.10 for an equilibrium system with N_α atoms of the type α and N_β β atoms and so on, with N number of all the atomic species in the system, we can write

$$S_{coh}(\vec{Q}) = \mid \sum_{\alpha}^{N} F_\alpha(\vec{Q}) f_\alpha(\vec{Q}) \mid^2 = \mid \sum_{\alpha}^{N} \sum_{i_\alpha}^{N_\alpha} \exp\left(i\vec{Q}\cdot\vec{r}_{i_\alpha}\right) f_\alpha(\vec{Q}) \mid^2 =$$

$$= \left(\sum_{\alpha}^{N} \sum_{i_\alpha}^{N_\alpha} \exp\left(i\vec{Q}\cdot\vec{r}_{i_\alpha}\right) f_\alpha(\vec{Q}) \right) \left(\sum_{\beta}^{N} \sum_{j_\beta}^{N_\beta} \exp\left(i\vec{Q}\cdot\vec{r}_{j_\beta}\right) f_\beta(\vec{Q}) \right)^* =$$

$$= \sum_{\alpha,\beta}^{N,N} f_\alpha(\vec{Q}) f_\beta(\vec{Q}) \sum_{i_\alpha,j_\beta}^{N_\alpha,N_\beta} \exp\left[i\vec{Q}\cdot\left(\vec{r}_{i_\alpha} - \vec{r}_{j_\beta}\right)\right]. \qquad (2.14)$$

Using the property of the δ function, we can substitute the expression $\exp[i\vec{Q}\cdot(\vec{r}_{i_\alpha}-\vec{r}_{j_\beta})]$ with the Fourier transform of $\delta(\vec{r}-(\vec{r}_{i_\alpha}-\vec{r}_{j_\beta}))$, such that

$$S_{coh}(\vec{Q}) = \sum_{\alpha,\beta}^{N,N} f_\alpha(\vec{Q}) f_\beta(\vec{Q}) \sum_{i_\alpha,j_\beta}^{N_\alpha,N_\beta} \int \delta(\vec{r}-(\vec{r}_{i_\alpha}-\vec{r}_{j_\beta})) \exp(i\vec{Q}\cdot\vec{r}) d^3\vec{r}. \tag{2.15}$$

We can then consider the average of the atomic positions and replace $\delta(\vec{r}-(\vec{r}_{i_\alpha}-\vec{r}_{j_\beta}))$ with $\overline{\delta(\vec{r}-(\vec{r}_{i_\alpha}-\vec{r}_{j_\beta}))}$ and divide the sum over i_α, j_β in two contributions:

$$\sum_{i_\alpha,j_\beta}^{N_\alpha,N_\beta} \int \overline{\delta(\vec{r}-(\vec{r}_{i_\alpha}-\vec{r}_{j_\beta}))} \exp(i\vec{Q}\cdot\vec{r}) d^3\vec{r} = \sum_{i_\alpha=j_\beta}^{N_\alpha} \int \overline{\delta(\vec{r})} \exp(i\vec{Q}\cdot\vec{r}) d^3\vec{r} + \\ + \int \sum_{i_\alpha\neq j_\beta}^{N_\alpha,N_\beta} \overline{\delta(\vec{r}-(\vec{r}_{i_\alpha}-\vec{r}_{j_\beta}))} \exp(i\vec{Q}\cdot\vec{r}) d^3\vec{r}. \tag{2.16}$$

Since $\int \overline{\delta(\vec{r})} \exp(i\vec{Q}\cdot\vec{r}) d^3\vec{r} = \int \delta(\vec{r}) \exp(i\vec{Q}\cdot\vec{r}) d^3\vec{r} = 1$, the first term is equal to the number of atoms of the type α when $\alpha = \beta$, while is equal to 0 when $\alpha \neq \beta$:

$$\sum_{i_\alpha=j_\beta} \int <\delta(r)> \exp(i\vec{Q}\cdot\vec{r}) d^3\vec{r} = N_\alpha \delta_{\alpha\beta}, \tag{2.17}$$

with $\delta_{\alpha\beta}$ being the Kronecker's delta.

The second term is instead directly linked to the radial distribution function $g(\vec{r})$ [43], according to the following relation, valid in the case of a monoatomic liquid:

$$\sum_{i\neq j}^{N} \overline{\delta(\vec{r}-(\vec{r}_i-\vec{r}_j))} = \frac{N^2}{V} g(\vec{r}), \tag{2.18}$$

where V is the volume containing the N atoms. The radial distribution function $g(\vec{r})$ is defined such that $g(\vec{r})d^3\vec{r}$ gives the average number of atoms contained in the volume $d^3\vec{r}$ at a given distance $\vec{r}$ from a reference atom, divided by the average density ρ of the medium.

For small $\vec{r}$ values, when it is not possible to find any atom at a distance r from the reference atom, $g(\vec{r}) = 0$. For big distances the average number of atoms in $d^3\vec{r}$ tends to $\rho d^3\vec{r}$ and $g(\vec{r}) \to 1$ (in this definition it would actually tends to $(1-1/N)$). Between these two limits, $g(\vec{r})$ shows an oscillatory behaviour damping as r increases. For a multiatomic system eq.2.19 becomes

$$\sum_{i_\alpha\neq j_\beta}^{N_\alpha,N_\beta} \overline{\delta(\vec{r}-(\vec{r}_{i_\alpha}-\vec{r}_{j_\beta}))} = \frac{N_\alpha N_\beta}{V} g_{\alpha\beta}(\vec{r}). \tag{2.19}$$

In this case $g_{\alpha\beta}(\vec{r})d^3\vec{r}$ gives the average number of the atoms of the type β in the volume $d^3\vec{r}$ in the position $\vec{r}$ with respect to an α atom, divided by ρ_β, the average

density of atoms β.
In conclusion, the diffracted intensity $S_{coh}(\vec{Q})$ can now be written as a function of the radial distribution functions $g_{\alpha\beta}(\vec{r})$ in the following way:

$$S_{coh}(\vec{Q}) = \sum_{\alpha,\beta}^{N,N} f_\alpha(\vec{Q}) f_\beta(\vec{Q}) \left(N_\alpha \delta_{\alpha\beta} + \frac{N_\alpha N_\beta}{V} \int g_{\alpha\beta}(\vec{r}) \exp\left(i\vec{Q}\cdot\vec{r}\right) d^3\vec{r} \right). \tag{2.20}$$

Integrating this expression over all the possible directions we get

$$S_{coh}(Q) = \sum_{\alpha,\beta}^{N,N} f_\alpha(Q) f_\beta(Q) \left(N_\alpha \delta_{\alpha\beta} + \frac{N_\alpha N_\beta}{V} \int_0^{+\infty} g_{\alpha\beta}(r) \frac{\sin(Qr)}{Qr} 4\pi r^2 dr \right). \tag{2.21}$$

This relation shows how laser induced changes in $g_{\alpha,\beta}(r)$ are seen as a change in the scattering. Note that the weight of a certain atom-atom pair is proportional to $Z_\alpha Z_\beta$. The Q dependence of the atomic formfactors makes impossible to Fourier invert S(Q) into real space. In other words, it is impossible to recover $g_{\alpha,\beta}(r)$ directly. In a solution, a homogeneous mixture of two (or in general more) substances, the solute and the solvent, it can be useful to divide the $g_{\alpha\beta}(r)$ in different contributions. Let us consider the example of a solution of Br_2 dissolved in CCl_4. It is possible to identify 3 different $g_{\alpha\beta}(r)$, which are shown in Fig.2.3.

We will have, first of all, $g_{\alpha\beta}(r)$ functions where both α and β belong to the solvent. The green curve shows the $g_{Cl,Cl}(r)$ (of course there will be also the $g_{C,C}(r)$ and $g_{C,Cl}(r)$ for the CCl_4 molecule): these functions describe the structure of the liquid, and for this reason they depend on the thermodynamical variables (temperature, pressure, density); however, in a solution, because of the presence of the solute, they could in principle be different from the pure-liquid $g_{\alpha\beta}(r)$s . An effect that has not been measured so far with the time resolved X-ray scattering. The pink curve shows instead a $g_{\alpha\beta}(r)$ curve with α belonging to the solvent and β to the solute molecule (in this case $g_{Br,Cl}(r)$). These are characteristic of the mixing and describe the structure of the solvent around the solute, what we call the cage. The $g_{\alpha\beta}(r)$ for which both α and β belong to the solute, as for the purple curve $g_{Br,Br}(r)$, describes eventually the structure of the solute molecule itself.

From these considerations, and the observed relation between RDF and experimentally measurable $S(Q)$, we can already anticipate here that there will be, consequently, three different contributions to the measured signal playing different roles at different time scales when observing structural changes during a chemical reaction in solution phase [9, 20, 64, 1, 46]: the (direct) photo-induced change in solute structure, the change in the solvation cage, i.e. the new solvent packing around the solute, and the bulk solvent response to heating and thermal expansion. This heating is induced by the transfer of energy from the photon-absorbing solute to the surrounding solvent. The underlying mechanism is that vibrational relaxation of a nascent molecule is very fast, typically over in 1-100ps, which causes the temperature of the solvent to rise locally on

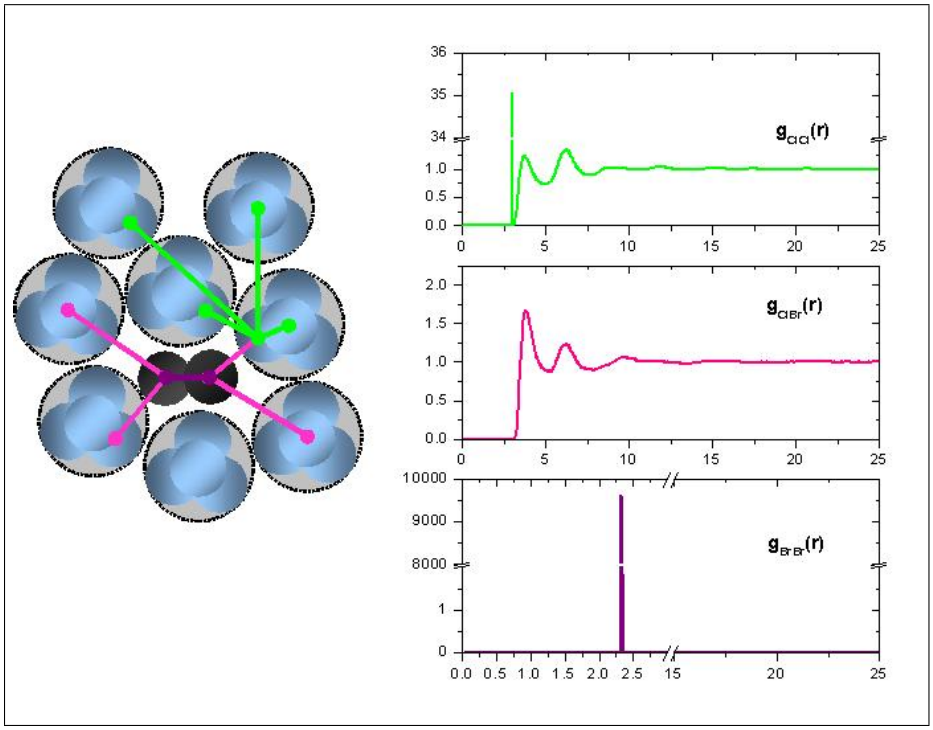

Figure 2.3: Schematic representation of the different $g_{\alpha\beta}(r)$ functions in a solution of Br_2 (black molecule) in CCl_4 (light blue molecules) chosen as example. In green we show one of the three possible solvent-solvent (Cl-Cl) correlations, and on the right panel the correspondent $g_{\alpha\beta}(r)$ function (obtained in the way we will see later from MD simulation). In pink the solute-solvent correlation between Br and Cl with the simulated RDF curve on the right and in purple the solute-solute $g_{Br,Br}(r)$.

the same time scale. The time scale for expansion relaxation, in contrast, is linked to the release of the pressure gradient in the laser spot, which generates a density wave that travels outwards at the speed of sound. The over-pressure is typically released in 50ns for our sample dimensions. The (adiabatic) expansion reestablishes the ambient pressure in about 50ns.

2.2 The Pump and Probe Technique at ID09B beamline at the ESRF: data collection strategy

Armed with the atom-atom correlation functions $g_{\alpha,\beta}(r)$ developed in the previous section, we will now move on to the experimental part of the project. Our aim is to track photo-induced atomic motions in small molecules in solution during a chemical reaction. We need then to collect diffraction intensities of the system as a function of Q and as a function of the time after having optically triggered the reaction. This is done using a stroboscopic pump and probe approach which we will describe below. Thus, we will start by stressing the "philosophy" of the technique, the signals we obtain and how we analyse the data to get a real-space picture of the evolving molecules.

2.2.1 Stroboscopic pump and probe technique and the difference maps

Let's start from the principal drawing in Fig.2.4, of our experimental set-up for liquids to understand how the data is collected in pump-probe experiments. We will discuss the specifics of the most important components in more detail in the next section.

The laser pulse excites a subset of solutes in the solution which is flowing in a closed loop sample cell. The laser both initiates and clocks the chemical reaction. Then a delayed 100ps long X-ray pulse probes the structure of the excited system. The diffraction pattern, which is averaged over 100ps, the time it takes for the pulse to cross a quasi stationary molecule, is detected by a 2-D MarCCD detector, which is centred on the incoming beam. The intensity is measured as a function of the scattering vector Q and the time delay between the laser and the X-ray pulses. The data collection strategy is to collect triplets of images for each time delay. Indeed the data is collected in units of *laser off/laser on/laser off* triplets (i.e. a diffraction pattern from the non-excited system, a diffraction pattern from the system after a given time delay and a second non-excited control). We average the two *laser off* patterns to minimise the effect of slow drifts in beam position, and this is done in angular space after radially integrating the 2D images using the FIT-2D software [67]. Then we subtract the *laser off* average from the *laser on* signal at every time delay which gives us the difference diffraction pattern $\Delta S(Q)$. From now on we will work with these difference maps , to follow the process triggered by the laser. From the snapshots taken as time goes by we can reconstruct a film of the evolution of the system, Fig.5.2.

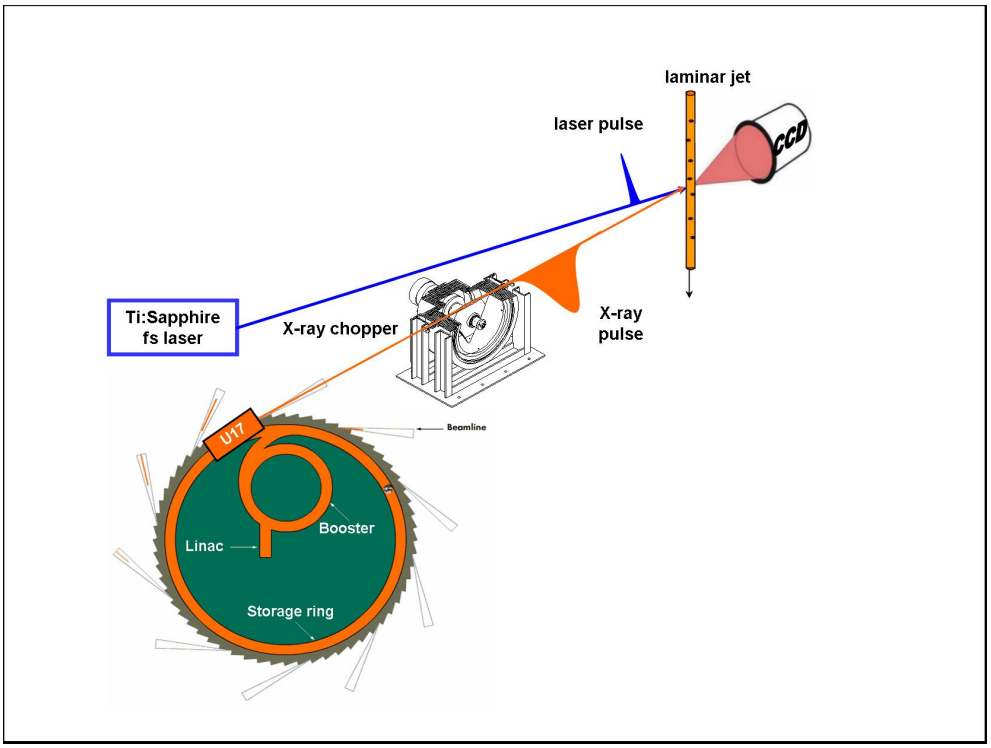

Figure 2.4: The principle of optical pump/X-ray probe set-up on ID09B [42].

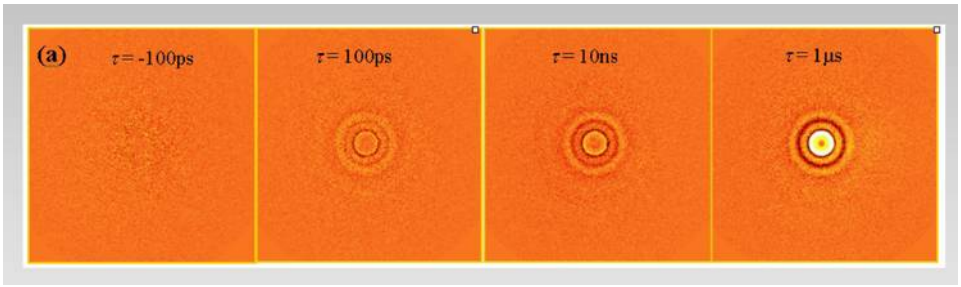

Figure 2.5: Differences of the diffraction patterns collected for Br_2 in CCl_4 as a function of the time delay. There is no difference intensity at $-100ps$, which confirms the accurate timing between the laser and X-ray pulses. At positive time delays, the difference features appear and progress with the time.

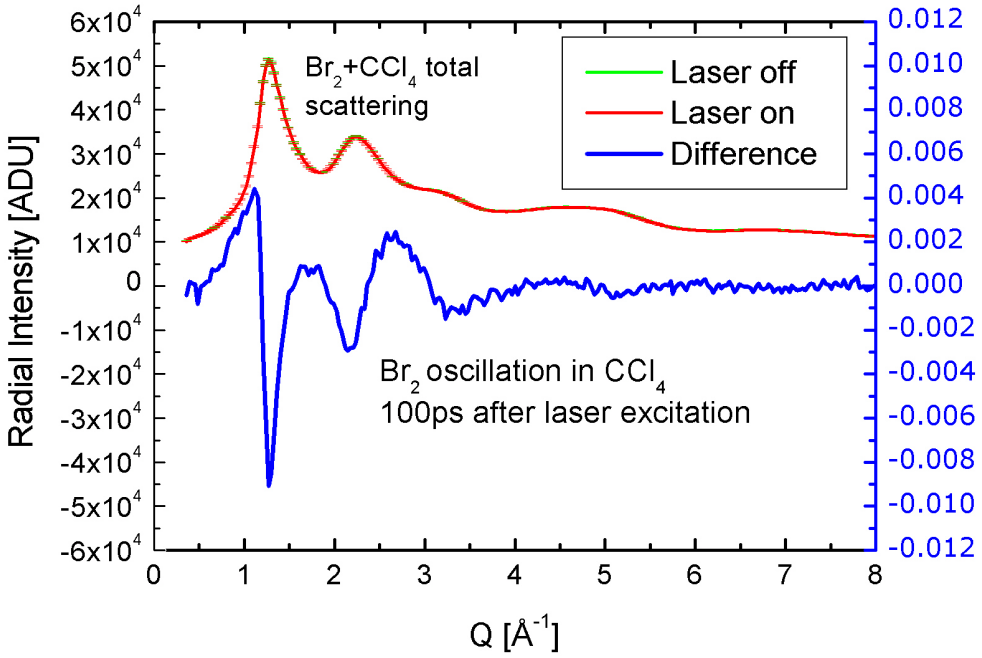

Figure 2.6: Radial intensities of non-excited Br_2 in CCl_4, of excited Br_2 in CCl_4 100ps after the excitation, and difference between the two. The solute signal is embedded in a huge solvent background and the laser-induced changes are of the order $\Delta S/S < 0.2\%$.

Let us observe the $\Delta S(Q)$ collected for Br_2 in CCl_4 100ps after the excitation [1, 9]. Without going into the details of the experiment, that we will discuss later, let us make some preliminary observations from the curves in Fig.2.6.

We can first of all notice that the laser on and laser off curves nearly coincide: the solute signal is buried in a huge solvent background and the laser induced changes are of the order $\Delta S/S < 0.2\%$. This weak relative signal calls for a very stable experimental set-up. The X-ray source, the optics, the chopper, the flow cell and the detector all have to be extremely stable in order to derive usable data [48]. Then we can for instance, in order to understand the features contained in the experimental signals, theoretically calculate the scattered intensity. We can start, for simplicity, with the intensity scattered by a ground state Br_2 molecule given by the Debye function for an isolated molecule in its gas phase, as shown in Fig.2.7. If, with the laser, we excite the system in a higher electronic state we will have a molecule with a different bondlength: as we can see from the formula (Eq.2.12), the scattered intensity will change. We can take the difference of these two curves and get the $\Delta S(Q)$ for this transition, a curve which goes to zero for $Q \to 0$. If we dissociate the molecule and we calculate the intensity given by two separated Br atoms and then subtract the $S(Q)$ of the ground state molecule, we find that in this case for $Q \to 0$, $\Delta S(Q)$ goes negative. A negative feature at low Q in $\Delta S(Q)$ can always be read as a fingerprint of dissociation.

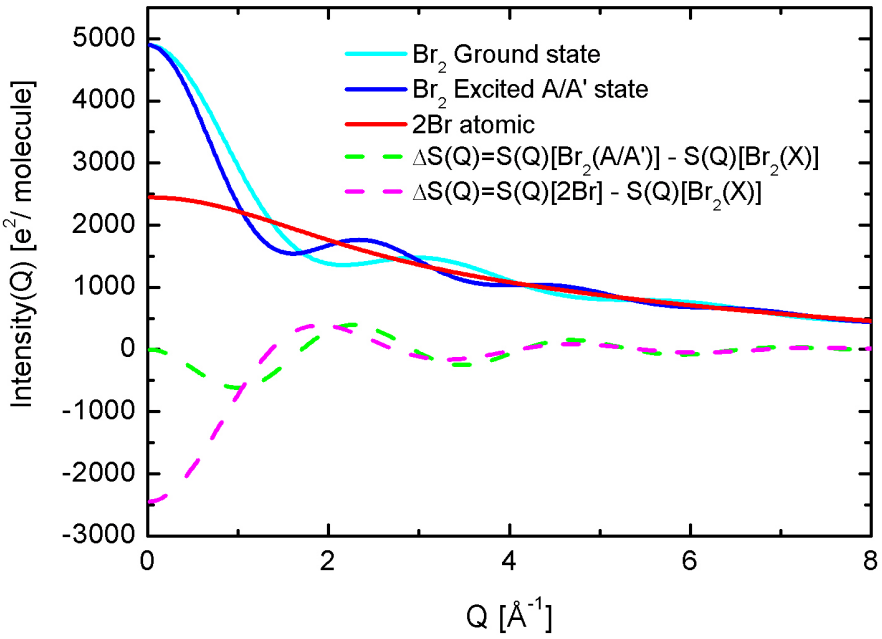

Figure 2.7: Simulation of the diffracted intensities from isolated Br_2 molecules in the ground and excited state, and from two infinitely separated Br atoms. The difference curves represent the theoretical diffracted intensities in a transition between the ground state to the excited one and between the ground and the dissociated state. In particular the negative feature at low Q in the difference curve is the fingerprint of dissociation.

2.2.2 Theoretical expression for the difference diffracted intensities

The recently published theory of time-resolved X-ray diffraction [44, 20, 1] help us to better understand the information included in the difference diffracted signals $\Delta S[Q,\tau]$. Briefly, this theory involves two steps: the first consists in developing a Maxwell-type theory of X-ray scattering by an optically excited system of charges and currents. In the second step these currents, that are supposed to be known in the first step, are actually calculated. Methods of statistical mechanics of nonlinear optical processes are employed to achieve this goal [46]. Without going into the calculations details [46], it was found that the difference signal $\Delta S[Q,\tau]$ appears as a convolution between the temporal profile of the X-ray pulse envelope $I_X(t)$ and the diffraction signal of an infinitely sharp X-ray pulse $\Delta S_{inst}[Q,t]$:

$$\Delta S[Q,\tau] = \int_{-\infty}^{+\infty} dt I_X(t-\tau)\Delta S_{inst}[Q,t]. \tag{2.22}$$

This signal turns out to be dependent only on the properties of the material system and of the laser fields. A simplified expression for the $\Delta S_{inst}[Q,t]$ is derived assuming the validity of the quasistatic limit and the Born-Oppenheimer approximation in our experiments. The first consists in considering that the optical excitation is fast as compared with the chemical reaction. In fact, optical pumping is generally done on the picosecond time scale, whereas with present state of the art, the X-ray probing is at least 100 times longer. The simplicity of this situation is due to the fact that, if two dynamic variables evolve on vastly different time scales, they are essentially independent. The Born-Oppenheimer approximation instead introduces the separation of electronic and nuclear motions; for convenience, the latter will be considered to be classical. Each excited electronic state of the molecule can then be considered as a distinct molecular species, and the laser-excited system can be viewed as a mixture of them. The local structure of such a system is generally described in terms of atom-atom distribution functions $g_{\mu,\nu}(r,t)$. These functions are proportional to the probability of finding the nuclei of atoms μ, ν at the distance r at time t. With these considerations

$$\begin{aligned}\Delta S_{inst}[Q,t] = \left(\frac{e^2}{mc^2}\right)^2 P\Bigg\{\sum_{\mu\neq}\sum_{\nu} f_\mu f_\nu \Bigg[\frac{1}{V(t)}\int_0^{+\infty} dr' \\ \times 4\pi r'^2 (g_{\mu\nu}(r',t)-1)\frac{sinQr'}{Qr'} - \frac{1}{V(0)} \\ \times \int_0^{+\infty} dr' 4\pi r'^2 (g^0_{\mu\nu}(r')-1)\frac{sinQr'}{Qr'}\Bigg]\Bigg\}.\end{aligned} \tag{2.23}$$

In this expression $g_{\mu\nu}(r',t)$ and $g^0_{\mu\nu}(r')$ are the atom-atom distribution functions before and after laser excitation, f_μ and f_ν are atomic form factors, and $V(t)$ is the volume of the system. The sums $\sum_\mu, \sum_\nu$ extend over all pairs of nuclei. Note that the functions $g_{\mu,\nu}(r',t)$ are averaged over all laser-excited electronic states j, carrying the populations

$n_j(t)$. Then, if the $g^j_{\mu\nu}(r',\tau)$'s describe atom-atom distributions in the electronic state j, one finds

$$g^j_{\mu\nu}(r',\tau) = \sum_j n_j(t) g^j_{\mu\nu}(r',t). \tag{2.24}$$

2.2.3 Fourier transformed signals $\Delta S[r,\tau]$

As we said already and as widely known, "photographing" atomic positions in a liquid can be achieved in static problems by Fourier transforming the X-ray diffraction pattern [38, 39, 45]. The situation is particularly simple for atomic liquids, where the well-known Zernicke-Prins formula provides $g(r)$ directly [38]. Starting from the basic theory of time-resolved X-ray diffraction explained in the previous section, we can now see which information is contained in the Fourier transform of the experimental $\Delta S[Q,\tau]$, to see how the problem of visualisation of atomic motions can be tackled. A convenient starting point in this study consists in introducing a properly normalised Fourier sine transform of the quantity $M(Q)Q\Delta S(Q,\tau)$ where M is the normalisation factor $M(Q) = [\sum_{\mu\neq\nu} f_\mu(Q) f_\nu(Q)]^{-1}$ [46]. By definition

$$\Delta S[r,\tau] = \frac{1}{2\pi^2 r}\int_0^{+\infty} dQ \left[\sum_{\mu\neq}\sum_{\nu} f_\mu(Q) f_\nu(Q)\right]^{-1} Q\Delta S(Q,\tau) sin(Qr). \tag{2.25}$$

Using in eq.2.25 the quasistatic $\Delta S(Q,\tau)$ as from eq.2.22 and eq.2.23 it can be demonstrated that [46]

$$\Delta S[r,\tau] = \int_{-\infty}^{+\infty} I_X(t-\tau)\Delta S_{inst}[r,\tau], \tag{2.26}$$

$$\begin{aligned}\Delta S_{inst}[r,\tau] = \left(\frac{e^2}{mc^2}\right)^2 P\Bigg\{\Bigg[\sum_{\mu\neq}\sum_{\nu}\frac{1}{\pi r}\int_0^{+\infty} dr' w_{\mu\nu}(r-r') \\ \times\left(\frac{1}{V(t)} g_{\mu\nu}(r',t) - \frac{1}{V(0)} g_{\mu\nu}(r')\right)\Bigg] \\ - \left[\frac{1}{V(t)} - \frac{1}{V(0)}\right]\Bigg\},\end{aligned} \tag{2.27}$$

$$w_{\mu\nu}(x) = \int_0^{+\infty} dQ f_\mu(Q) f_\nu(Q)\left[\sum_{\mu\neq}\sum_{\nu} f_\mu(Q) f_\nu(Q)\right]^{-1} cos(Qx). \tag{2.28}$$

From this expression of $\Delta S[r,\tau]$ it is possible to understand its physical meaning and the information it can provide about molecular motions in liquids. First of all one has to notice that the signal $\Delta S_{inst}[r,\tau]$ has two terms. The first describes the change in the pair distribution functions $g_{\mu\nu}$ during the chemical reaction, and it is thus related to the molecular dynamics of the reactive system. The second-term probes the change in the volume V due to laser heating. Secondly, as we also noticed in eq.2.21, it stands

out that the atom-atom distribution functions $g_{\mu\nu}$ do not enter into $\Delta S[r,\tau]$ alone but are coupled with the atomic form factors $f_\mu(Q)$, $f_\nu(Q)$ via $w_{\mu\nu}(x)$'s. This blurs the information contained in $\Delta S[r,\tau]$. It can be observed that if the atoms μ,ν belong to different molecules, the corresponding peaks in $\Delta S[r,\tau]$ are mainly shaped by the $g_{\mu\nu}$'s. In contrast, if they are located on the same molecule, the $f_\mu(Q)$, $f_\nu(Q)$'s dominate. Moreover, the fact that the signal $\Delta S[r,\tau]$ is composed of a number of different $g_{\mu\nu}$'s is not a real handicap. Indeed, if the μ-ν bond is broken, only the distribution function $g_{\mu\nu}$ of atoms μ, ν forming this bond stands out in the difference signal. Other terms disappear, partially or completely. Thermal expansion dominates $\Delta S[r,\tau]$ at small r's. At these distances the atoms behave as hard spheres, the $g_{\mu\nu}$'s all vanish and only the term $1/V(0) - 1/V(t)$ survives. As $\Delta V/V = -\Delta\rho_M/\rho_M$ the evolution of the mass density can be monitored in this region of r. What we learn is, in conclusion, that under the quasistatic conditions, and with a certain number of required precautions, the Fourier transform of the difference diffraction signals, permits to "film" atomic motions monitoring molecular dynamics.

2.2.4 Example of real space information

From the above consideration we can then interpret the experimental $\Delta S[r,\tau]$, obtained for the Br_2 in CCl_4 experiment where the 138mM concentration of Br_2 was excited at 400nm. At this concentration, the Br_2/CCl_4 mixing ratio is 1:75. The gap of the undulator was 9.0mm which put the undulator peak at 18.15keV and the centre of mass energy E_X, the effective energy used in transforming $2\theta \rightarrow Q \rightarrow r$, was 17.755keV.

In Fig.2.8 we show the difference maps in real space for the time delays 100ps, 200ps, 500ps, 1ns. As we saw in the previous chapter, the equilibrium Br-Br bondlength for the Br_2 molecule in the ground state is 2.3Å . It is clear that the minimum at this distance represents the depletion of the X state in Br_2 from the dissociation. Some fraction of the Br_2 molecules recombine in the A/A' state: indeed we can see a maximum appearing at 3Å , which is the equilibrium Br-Br distance in the A/A' state. We see that the amplitude of the minimum at 2.3Å decreases with time, in other words, the ground state gradually recovers. In principle, we should observe as a counterpart the decrease of the amplitude of the maximum at 3Å, indeed, the excited molecules relax from the A/A' state back to the ground state. Fewer and fewer molecules are then found as time goes by in this excited level and these molecules reappear with the typical Br-Br distance of the ground state. Nevertheless, unfortunately this peak results to be composed of twin peaks, where one is coming from the solvent response. In the same way, also the features at higher distances are more complex to interpret, because they involve inter-molecular correlations in the solvent, beyond the length scale of the bromine dynamics: we can assign the minimum at 6.2Å to a temperature rise in the bulk solvent: as the excited solute molecules recombine to the ground state, they release heat into the solvent. This produces a broadening of the solvent's intermolecular distance distributions at constant volume. In other words, the atom-atom distributions broaden without shifting their "center of mass". In the difference map, this shows up as a three-peak structure, two positive peaks centred around a negative peak. We attribute this feature to the $Cl..Cl$ intermolecular distance, because of its bigger relative

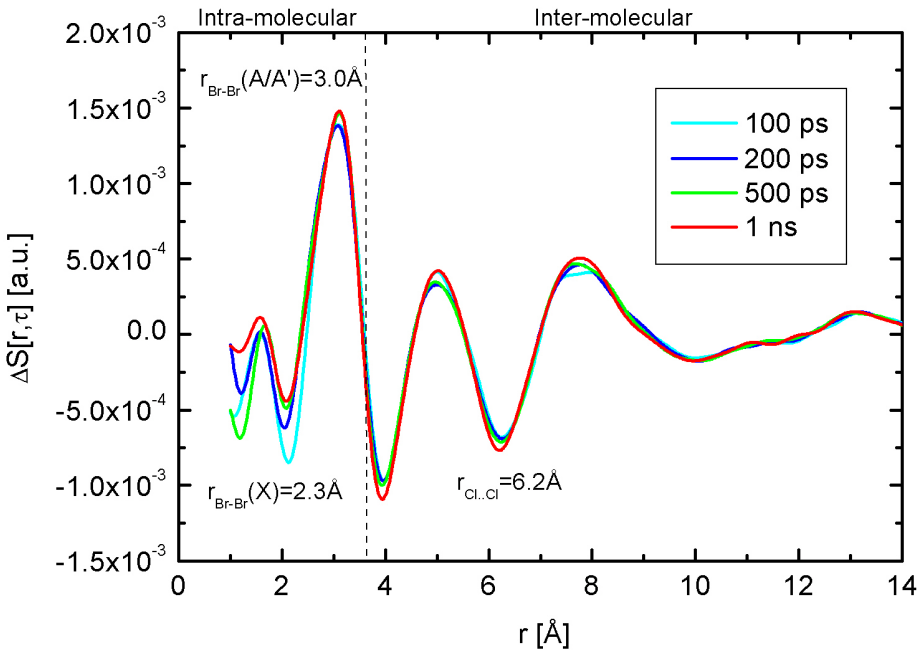

Figure 2.8: Radial difference curves at different time delays for the Br_2/CCl_4 solution. The peaks and valleys at the different r distances show depletion and formation of bonds and their time evolution.

Z_iZ_j weight as compared to the $C..Cl$ or $C..C$ correlations. This first analysis of radial difference maps give a preview of how it is possible to follow chemical reactions and relaxation processes in solution [1, 9]. For a full understanding of the time-resolved curves, including the cage and the solvent's thermal expansion, Molecular Dynamics simulations and solvent response studies are required [9, 20, 64, 1, 46]. We pointed out that the conversion of X-ray data to molecular geometry is relatively direct, these hard photons being scattered by core electrons, which are tightly bond to the nuclei. We will now see in the next section how the nature of synchrotron radiation makes it one of the most important tools for investigating molecular and atomic structure, stressing why in particular X-ray diffraction appears to be a powerful tool for studies of structural dynamics in liquids. Despite the 5 to 6 orders of magnitude lower scattering power of X-rays as compared to electrons, X-rays have the great advantage of being applicable in condensed phase materials. Electron diffraction is particularly useful for the gas phase, thin films and surfaces, where the electron's high scattering cross section is a great asset. But the high scattering cross section translates into low penetration depth, which makes it nearly impossible to use electron diffraction in condensed phase.

2.3 The Pump and Probe Technique on beamline ID09B at the ESRF: experimental details

A deeper description of the experimental apparatus for Time Resolved X-ray Diffraction on liquids will now be given, comprising the X-ray source at the ESRF, the laser system, and how the two sources are brought to the sample and how they are phased. We will start this section by explaining the characteristics of synchrotron radiation and its suitability for liquid studies with special emphasis on the ESRF parameters [49, 48, 51, 50].

2.3.1 The probe: Synchrotron Radiation

When electric or magnetic fields force electrons or other charged particles, moving with relativistic speed, to follow curved trajectories, they radiate electromagnetic radiation in a narrow cone in the direction of their motion. This highly collimated radiation is called synchrotron radiation. Synchrotron radiation emitted by electrons in particle accelerators is extremely intense and extends over a broad energy range from the infrared through the visible and the ultraviolet, into the soft and hard X-ray regions of the electromagnetic spectrum. Due to these and other characteristics, synchrotron radiation has become a fundamental tool to study several different aspects of the structure of matter at the atomic and molecular level. The main properties of the radiation emitted from a synchrotron depends a lot on the characteristics of the circular accelerator (storage ring) used to produce it. We can nevertheless make a list of the most important parameters:

1. high intensity;
2. high brilliance (from a small source);
3. very broad and continuous spectral range;
4. narrow vertical collimation;
5. high degree of polarisation;
6. high beam stability;
7. pulsed time structure.

The properties of synchrotron radiation can be calculated by applying the methods of classical electrodynamics to the motion of relativistic charged particles [39, 52, 49]. A complete account of the properties of synchrotron radiation would though be beyond the aim of this thesis. For these reasons I would like only to focus on what makes X-rays a particularly suitable probe for the present study, spending then some words on the last property in the list, the pulsed time structure, which allows us to follow atomic motions during chemical reactions.

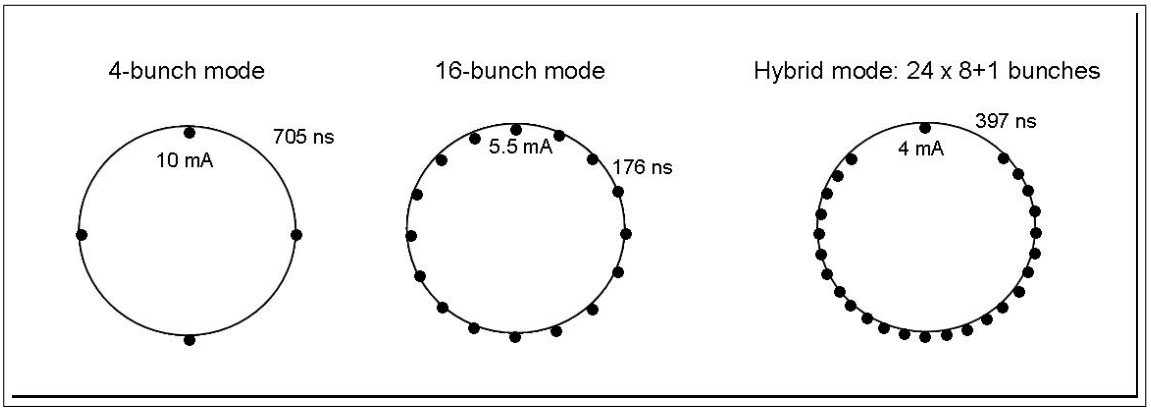

Figure 2.9: Timing mode at the ESRF: in these filling modes of the storage ring it is possible to isolate single X-ray pulses for pump and probe experiments [42].

The European Synchrotron Radiation Facility (ESRF)

Third generation synchrotrons are highly brilliant sources of X-rays and the ESRF is the most powerful synchrotron in Europe for hard X-rays above 10keV. In these large installations electrons are emitted by an electron gun and subsequently accelerated first in a linear accelerator (linac) and then transmitted to a circular accelerator, the booster synchrotron where they are accelerated to 6GeV. These high-energy electrons are then injected into a large storage ring (844 metres in circumference) where they circulate, in bunches with the duration of 60-150ps, in a vacuum chamber, at a constant energy, which is maintained by a RF field. The lifetime of the beam is typically varies between 60 and 10 hours depending on the operating mode of the storage ring, which we will discuss later. The storage ring has both straight and curved sections. As they travel around the ring, the electrons pass through different types of magnets. It is during the passage through the bending magnets or insertion devices that the X-rays are produced. In the case of bending magnets, when the electrons pass through these magnets, they are deflected from their straight path by 11.25 degrees: this change in direction causes them to emit weak incoherent radiation. The insertion devices, or undulators, consist of arrays of magnets with alternating polarity: the electrons undergo undulations forced by the magnetic fields and the beams of radiation emitted from the different bends overlap and interfere with each other to generate a bright and partially coherent beam which is up to 1000 times more intense than the one generated by bending magnets. Focusing magnets are placed in the straight sections of the storage ring: these magnets are used to focus the electron beam, keeping it small and well-defined in order to produce the very bright X-ray beam needed for the experiments. Synchrotrons can operate in different timing modes characterised by the number of electron bunches in the storage ring. The rate at which bunches appear in the ring is a sub-harmonic of the RF frequency. At the ESRF the RF frequency is 352.2MHz, which allows having up to 992 bunches, separated in time by 2.84ns, around the 844.1m long ring.

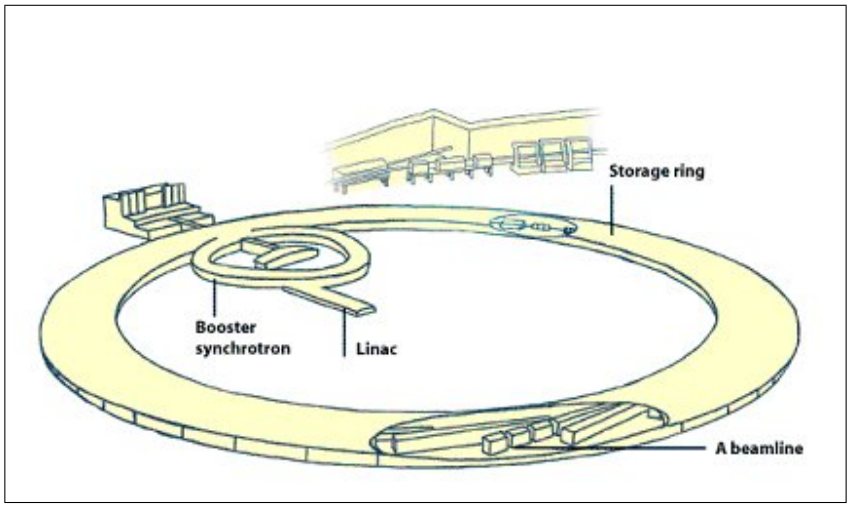

Figure 2.10: A very simple sketch of the different parts of the synchrotron [42].

Pulsed time structure

Forced into a circular orbit by the bending magnets, the electrons loose, during each turn, part of their energy to synchrotron radiation. The energy loss is regained in passing through the RF cavities. In a RF cavity a longitudinal electric field is generated in order to accelerate the electrons. The RF fields have an accelerating effect only during one half of their period and a decelerating action during the other half; so the RF cavity is effective in restoring the electron energy only for half of the time. Only "synchronous" electrons, i.e. electrons entering the cavity and finding at that time the exact electric field needed to fully restore the energy lost during one turn, will be in a stable condition. In this case they will continue their motion along the ring returning in the RF again in time to regain the exact amount of energy lost in the circular path. Slower or faster electrons with respect to the synchronous ones would need higher or lower energy to compensate their energy loss and therefore they will be lost. These considerations show that only one half of the accelerating period is effective in maintaining the stability of the orbit. And furthermore this condition is in reality even more strict and only 5%-10% of the RF period is effective in restoring the electron energy. All the electrons passing through the cavity out of phase with this 5%-10% effective time will not follow the ideal orbit of the ring and are therefore lost. As a consequence the electrons in the storage ring are grouped in bunches with a time length which is typically 5%-10% of the RF period. Of course, then, the emitted synchrotron radiation appears in pulses with the same duration which determines the highest achievable time resolution in our experiment. At the ESRF the temporal pulse length of an X-ray pulse is 100ps (fwhm).

2.3.2 ID09B beamline

The X-ray source at ID09B is a narrow band in-vacuum undulator, the U17, named after its 17mm magnetic period, which determines the characteristics of the X-ray

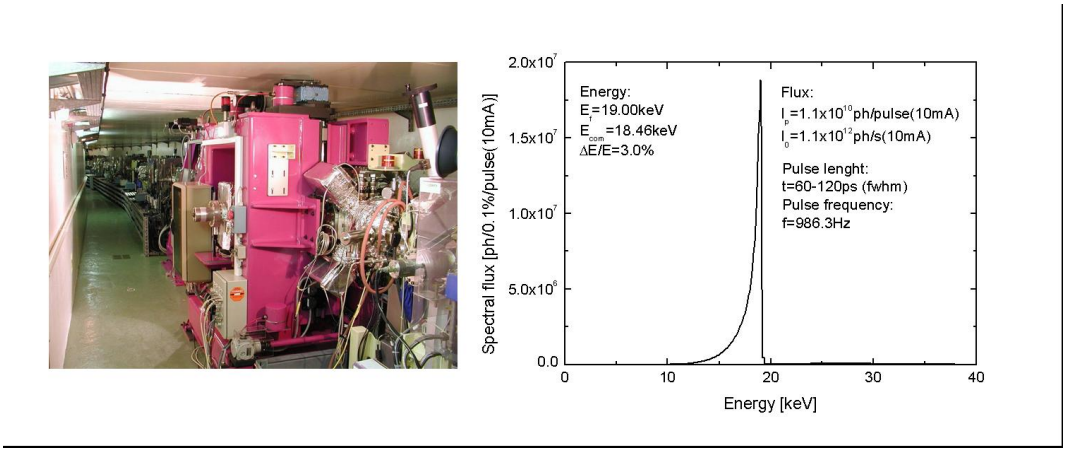

Figure 2.11: The in-vacuum U17 undulator on ID09B beamline and its spectral intensity [42].

radiation produced on ID09. The X-ray beam needs then to be aligned and focused onto the sample using X-ray optics, the X-ray optical devices in the optics hutch.

In order to perform time resolved experiments at the highest possible time resolution, we need to select a single X-ray pulse from the train of pulses from the undulator. This is done just before the sample, in the experimental hutch by a mechanical chopper. In this section we will go into some details of the most important X-ray devices and then describe the laser and the synchronisation between the pump and the probe. The latter controls the time delay at which we probe the structure of the sample during the reaction [49, 48, 50, 51].

The U17 undulator

The first element in the beamline is the U17 single line undulator, which produces X-ray pulses with up to 10^{10} photons per pulse by imposing a sinusoidal motion on the electron beam with the magnetic field from 236 poles with 17mm period. The magnets are placed inside the vacuum vessel for the electron beam thus allowing to move the magnets very close to the electron beam and hence increasing the field and deflection. By changing the gap, the energy of the X-ray can be varied from 15 to 20 keV, an energy range with an ideal trade-off between diffraction intensity and radiation damage. The spectrum produced is dominated by a single tooth-shaped line with a sharp energy cut-off at 15keV at 6mm gap, with a bandwidth $\Delta E/E \simeq 3\%$, followed by a broad second harmonic and a weaker but sharp third harmonic. The 3% bandwidth of the undulator is sufficiently monochromatic for most diffraction experiments in liquids due the natural positional and orientational disorder in liquids: this allows us to perform time resolved experiments to study reactions of molecules in liquid solution in polychromatic mode, without the need to monochromatise the beam. Indeed, as we saw looking at the difference maps, extremely intense X-rays are needed to discern the photo-signal from the solvent background with reasonably short exposure time (10s). In using the natural line width of the undulator we can gain up to two orders of magnitude in flux as compared to a monochromatic beam from a Si(111) monochromator [51]. On the other

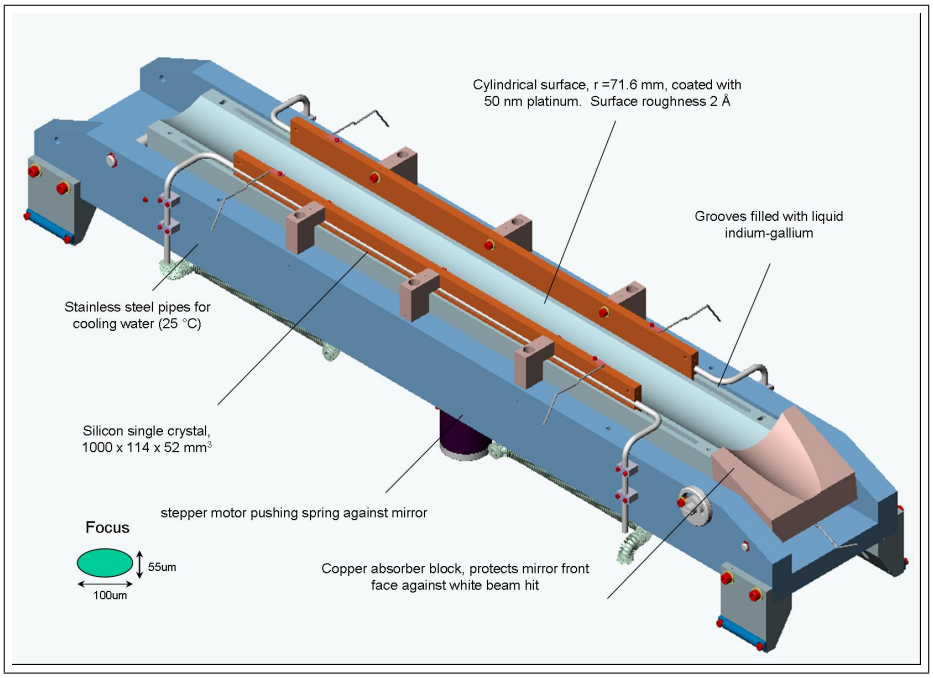

Figure 2.12: The toroidal mirror used to focus the pink beam [42].

hand this energy dispersion in the data means that in comparison between experiment and theory, the theory needs to be corrected for the U17 spectrum (as we will see later in the discussion of the data reduction procedure). Because of the partial coherence of the X-rays, the interference length inside the sample has a limited range. The longitudinal coherence length $\lambda_c = \lambda_X^2/\Delta\lambda \approx 17$ Å of the radiation from the U17 undulator at 17keV, is well beyond the first solvation shell of a typical solution. In CCl_4, just to give an example, the average distance between neighbouring molecules is 5.7Å which means that the U17 X-ray beam only resolves the first three coordination shells in pure CCl4.

The focusing mirror

The central cone of the X-ray beam coming out from the undulator is focused by a 1.0m long toroidal mirror cut from a single crystal of silicon. The mirror is located 33.1m from the source where the beam is 7.25mm wide and 0.67mm high. The toroidal shape is obtained by vertical bending of a cylinder. The mirror dimensions are chosen such that gravity curves the mirror into the parabolic shape needed to focus the beam 22.4m downstream, (R_m=9.9 km) into a 100μm x 60μm spot(fwhm). The mirror body is supported at the ends and the shape is controlled by a stepper motor acting on a spring from below the mirror. The mirror is coated by a 500Å layer of platinum, for improved reflectivity at high energies, with a surface roughness of 1.8Å(rms). The incidence angle is 2.668mrad and energies up to 26keV are reflected. The mirror is water cooled through copper plates that are immersed into indium-gallium filled channels along the sides of the optical surface. The liquid interface between the mirror body and the cooling system attenuates vibrations from the cooling system [53].

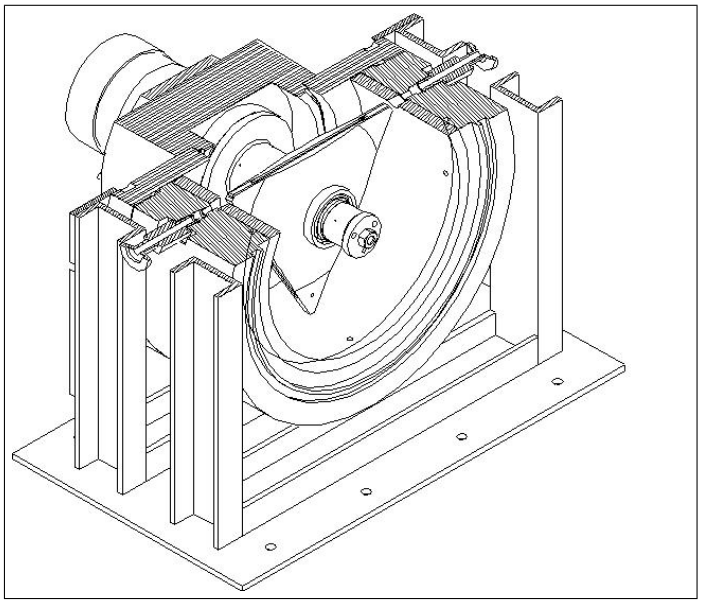

Figure 2.13: The ID09 chopper with the triangular titanium rotor in the vacuum chamber [42].

The single pulse selection

To reach 100ps time resolution in pump-probe measurements we have to select one single pulse out of the train of pulses from the undulator. One of the main tasks in ultrafast pump-probe experiments at synchrotrons is to control the pulse structure on the sample. The frequency of the X-ray pulses from the 16-bunch mode is 5.7MHz, much faster than commercial milli-joule femtosecond lasers that typically run at 1kHz. As the laser/X-ray pulses have to arrive on the sample in 1:1 pairs when integrating CCD detectors are used, the X-ray frequency has to match that of the laser. The solution is to use a high-speed chopper in front of the sample where the chopping efficiency is high due to the small beam size. For this reason only modes with sufficient temporal separation between bunches are suitable for time resolved experiments. The pulse separation in 16-bunch mode is 176ns and 705ns in 4-bunch mode. The chopper isolates X-ray pulses at 986.3Hz.

The ID09 chopper consists of a triangular rotor made of titanium, which rotates about its center of gravity. The rotation axis is horizontal and perpendicular to the beam. The rotor has a groove in one of its sides. The groove is covered (or roofed) by small plates at its extremities. The groove is thus a semi-open tunnel. The rotor, which is suspended in magnetic bearings, rotates at 986.3Hz. It is thus mandatory to keep the rotor in vacuum.

The opening window, i.e. the transmission versus time, is generally trapezoidal in shape. The base line of the trapezoid is:

$$\tau = \frac{a}{2\pi R f \sqrt{1-(h/R)^2}},$$

where a is the height of the tunnel, R is the maximum radius of the triangle, h is

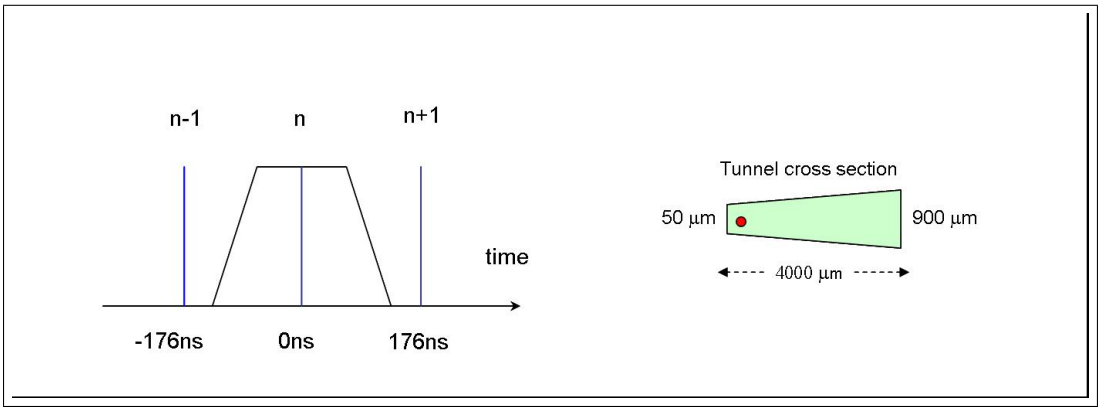

Figure 2.14: On the left we show the temporal acceptance window for single pulse selection in 16 bunch mode. On the right panel we show the trapezoidal shape of the chopper tunnel.

the (orthogonal) distance of the tunnel to the centre of rotation and f is the rotation frequency. The chopper parameters are R=98.6mm, h=47.4mm, f=986.3Hz.

The opening time, at the highest speed, can be varied by having a variable tunnel height. That is done by the use of a trapezoidal tunnel cross-section (Fig.2.14): the tunnel is 4.0mm wide and the height a increases linearly from 0.05 to 0.90mm. The opening time can thus be varied from about 80ns (a=50μm) to 1.47μs (a=900μm) by translating the chopper horizontally, which is useful for adapting to a given bunch structure. As the opening window has to synchronise to the centre of three pulses, the opening time has to be slightly shorter than twice the inter-pulse distance. In 16-bunch, the filling mode used for the experiments reported in this work, the inter-pulse separation is 176ns. Using the chopper at a height of 200μm, the opening time is 300ns, which allows us to select one single pulse.

The chopper selects pulses continuously at 986.3Hz, and selects hence a new pulse every 1.014ms. This introduces of course a huge loss of intensity in using 1 kHz X-rays which is partially compensated by using the polychromatic beam from the undulator, since the 3% bandwidth beam is 500 times more intense than a monochromatic beam from a silicon monochromator [51].

X-ray Detectors

Several different kinds of detectors are used on the beamline as diagnostic tools for the X-ray alignment, for the determination of the absolute time delay between the X-ray pulse and the laser pulse and to collect diffracted intensities. We will briefly go through the main characteristics of the different detectors used [51].
In the optics and experimental hutch three pindiode and two wire detectors are used to measure the intensity of the X-ray beam during the alignment procedure.

A very fast detector, sensitive to both X-ray and laser radiation allows us to measure the time delay between the pump and probe. It consists of a GaAs photoconductor that is operated with a bias voltage of +400V. On a fast digital oscilloscope (Tekronix TDS 694C, 3GHz) the time-trace of the signal can be recorded with a jitter of less than 10ps.

The resolution of the laser/X-ray time delay for the detector and oscilloscope has a time resolution of 10-20ps when the mid-point of the rising edges are used. A Cyberstar scintillation counter, which picks up air scattering from the X-ray beam, is used both for timing and evaluating the I_0 intensity that is actually impinging on the sample. This detector gives a (rising edge) time resolution of about 5ns. It is placed directly behind the sample slits, 40cm from the sample. The radiation hitting the scintillator detector is caused by air scattering and can be increased by introducing a scattering foil in the X-ray beam, which is sometimes needed when monochromatic beams are used. The diffracted X-ray intensity can be collected by a range of different detectors, from point detectors to high resolution 2D detectors depending on the problem studied. A special feature on ID09B is that if the beamline is run in stroboscopic mode, a strong burst of X-ray pulses is recorded within 100ps. Therefore photon counting is normally not feasible and pump-probe detectors are usually run in integrating mode or current mode.
The principle of the two-dimensional detector is a thin scintillator plate with a diameter of 132mm and 40μm thickness of $Gd_2O_2S:Tb$, that is connected to a fibre optic taper. The fibres demagnify the image by a factor 2.7 and guide the scintillation light to a 2048 x 2048 pixel CCD chip. The chip is cooled to a temperature of -70°C to reduce the dark current. At ID09 the MARCCD camera is equipped with a 1.6mm thick tungsten beamstop, that is directly mounted on the beryllium entrance window to provide additional protection from the primary beam. The camera is mounted on a horizontal translation stage, that allows to vary the sample-detector distance between 50 and 600mm. Attention should be paid to several things:

1. The dark current is low because of the low temperature of the CCD. It is measured to be 0.0044 ADU/pixel/sec.

2. The scaling factor is roughly 1ADU per 18keV photon.

3. The readout noise is quite considerable and consists of a deterministic part, that

Detector	**principle**	**field of view**
wire monitor	photo-electric	-
photodiode	semiconductor	⊘ 20mm
GaAs photoconductor	semiconductor	1mm x 0.4mm
Cyberstar	scintillator, photomultiplier	⊘ 25mm
MarCCD	scintillator, fibre optics, CCD	⊘ 132mm

Detector	**spatial resolution**	**time resolution**	**read-out time**
wire monitor	0.1mm	-	-
photodiode	-	300μs	-
GaAs photoconductor	1mm x 0.4mm	60ps	-
Cyberstar	0.1mm x 0.1mm (slits)	5ns	-
MarCCD	100μm	0.1s	8s

Table 2.1: Summary of some characteristics of the main detectors used on ID09B.

changes with continuous operation mode and a stochastic part, that can not be controlled.

4. The readout time and time for data transfer is about 15s using 1×1 binning.

5. The picture can be disturbed by single high ADU events, that occur randomly over the active area. These are caused by radioactive decays in the fiber optics. Special care should be taken to discard them from the data processing (e.g. by taking two identical images one after another and mask differing events or use the 180° symmetry of the X-ray signal).

Before performing any experiment the correct sample-detector distance is calibrated using the diffraction spectra from Al_2O_3 powder in a spinning capillary.
The CCD detector should ideally be spherical for diffraction experiments, but is in reality flat. Consequently the phosphor thickness "seen" by the scattered beam becomes $t/\cos 2\theta$. X-rays will thus be more efficiently absorbed at high angles and we need to correct the images and the radial distributions correspondingly. We define the phosphor correction R (a multiplicative scale-down factor to correct the data) such that we get the value seen by a spherical phosphor screen of thickness t:

$$R(E) = [1 - \exp(-\mu(E)t)]/[1 - \exp\left(\frac{-\mu(E)t}{\cos 2\theta}\right)],$$

$\mu(E)$, the linear absorption coefficient in cm^{-1}, being a function of the energy. This means that we need to calculate R for the value of X-ray energy used in the experiments to correct our data (Fig.2.15). The effective density of Gd_2O_2S to use in order to calculate $\mu(E)$ for our phosphor screen is $4.5g/cm^3$ which has to be additionally corrected for 4.5% terbium atoms present in the powder.

2.3.3 The pump: the laser system

We will now describe the femtosecond laser, used to initiate photoreactions [51]. As shown in Fig.2.3.3 it comprises four stages. The first stage is a continuous wave (CW) diode-pumped laser from Coherent (VERDI). It produces 5W of frequency-doubled light at 532nm. The VERDI pumps a Ti:sapphire fs-oscillator (MIRA, from Coherent). The optical cavity in this laser runs in phase with the RF clock at RF/4. This oscillator produces, via the Kerr-effect in the Ti:sapphire crystal, weak 100fs pulses at 800nm. The frequency is adjusted to RF/4 by adjusting the length of the cavity. The third stage, the Hurrican Laser from Spectra Physics, is a chirped pulse amplifier (CPA) which stretches, amplifies and compresses a sub-train of pulses at 986.3Hz. The pulses are amplified to 1.1mJ per pulse at 800nm and the pulse duration is 130fs. The fourth stage is the optical parametric generation (OPG)/optical parametric amplification (OPA) which uses frequency mixing to obtain wavelengths between 290-1500nm.

Recently (March 2006) the femtosecond laser system was upgraded, with the substitution of the MIRA and the Hurricane with the Halcyon oscillator and the Dragon

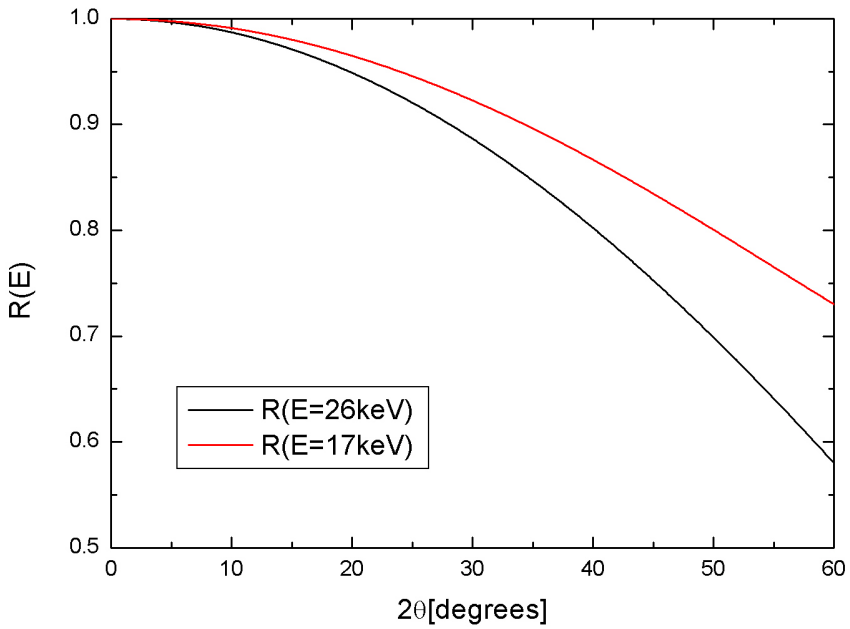

Figure 2.15: The $R(E)$ function used to correct for the flatness of the MARCCD phosphor screen plotted, as an example, for two different X-ray energies.

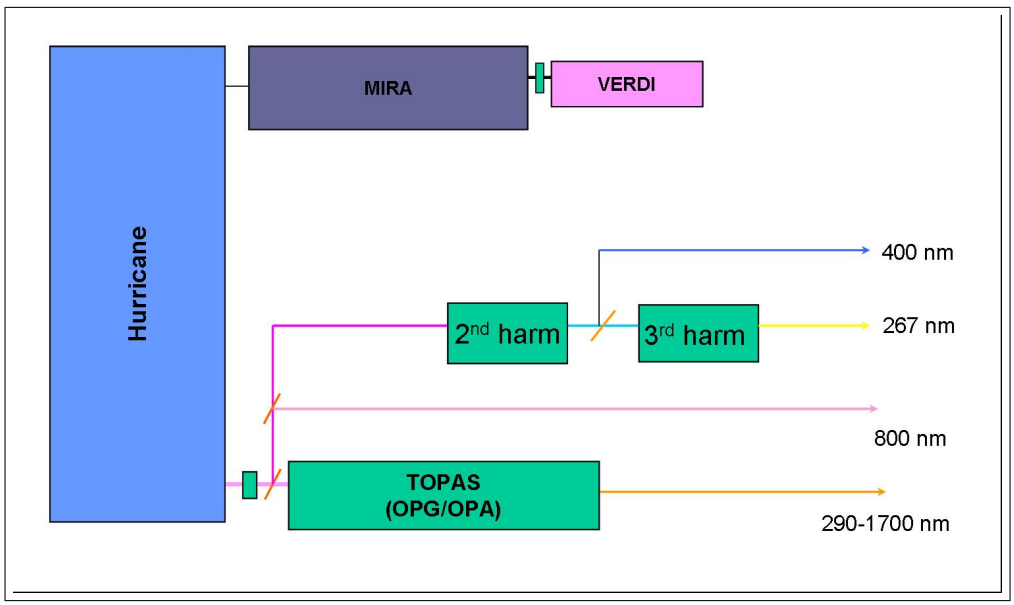

Figure 2.16: Simple sketch of the laser table: with the 4 stages of continuous and pulsed generation, amplification and tunability [42].

multipass amplier, both manufactured by KMlabs. I won't go into the details of the new system which was not used in the experiments described here. The new system should deliver 2.5mJ per (100fs) pulse with a maximum repetition rate of 3kHz. The higher energy will allow a higher excitation efficiency and its higher repetition rate will reduce the data acquisition time.

Synchronisation and timing

From the presented description of the experimental technique it appears how crucial is the correct and precise synchronisation between X-rays, chopper and laser. A very sophisticated electronics controls the synchronisation. The basic idea is nevertheless to use as fundamental frequency the frequency given by the bunch clock of the synchrotron ring, 352kHz and to split and electronically multiply or divide this signal to send it as input signal for the other instruments. The frequency of the chopper is matched to a sub-frequency (360^{th}) of the fundamental. Then the phase has to be adjusted to make it open at the right time to select one single pulse. This is done adding a delay to the signal which temporally shifts it without changing its frequency anymore. The laser system has instead a frequency of 88MHz which is, in general, proportional to the cavity length. The fundamental signal is then multiplied to match this frequency and the oscillator pick-up compares the two signal and adjust the cavity mirror to make the frequency of the laser match a higher harmonic of the fundamental. Another signal from the fundamental is sent to the pockel cell, to choose the laser pulse that has to be amplified. During the data collection then the X-ray/laser pulses delay has to be changed. By moving the Pockels cell the movements are done in step of 11ns, after which one selects a different laser pulse; to have a higher resolution the cavity length has to be changed: this is done through a phase shifter which makes the mirror in the cavity move until we get the same frequency but a different phase, shifted in time of the required delay.

2.3.4 Spatial overlap between laser and X-ray pulse

The spatial profile of the two spots is checked by means of a 100μm pinehole mounted in the axis of rotation of the goniometer where the sample is placed during the measurement. The pinehole is first aligned on the X-ray beam looking at the transmission profile and then rotated some 10 degrees, the incidence angle of the laser. The laser beam is moved by moving a motorised lens close to the sample. In this way a rough alignment of the two beams is obtained. A fine overlap is then achieved looking at the scattering patterns itself using what we call FOM (Figure Of Merit) scans. The procedure is based on the idea that, if the laser beam releases heat in the liquid, the liquid will expand. The main effect on long timescales (1μs) is a rigid shift of the first diffraction peak to lower Q-values, as a consequence of the increased distance of the first coordination shell. In that process, the Q values on the left hand side of the liquid peak will increase in intensity, Q values on the right hand side will decrease. We can thus divide the CCD in two concentric disks, an internal and an external, and divide the inner by the outer disk. In this way we obtain a number, FOM, which is

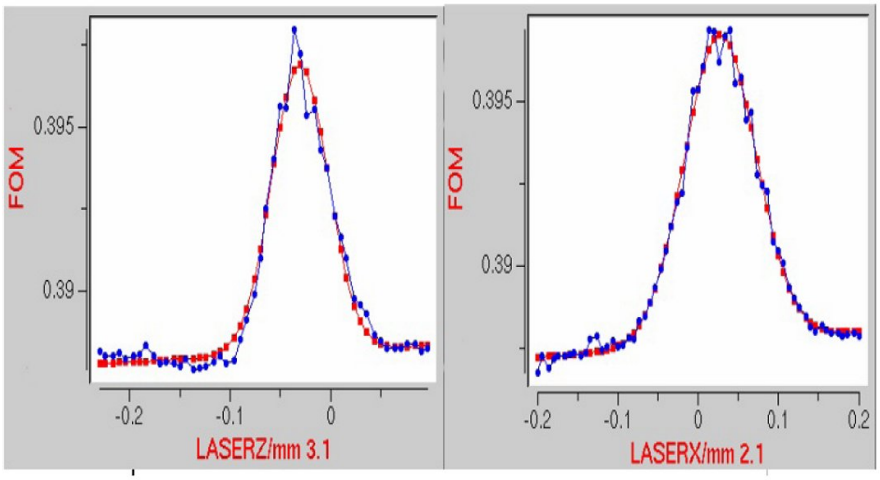

Figure 2.17: Experimental FOM scans in the two transverse dimensions together with Gaussian fits.

a measure of the temperature rise and based on only one diffraction image. Scanning the horizontal and vertical position of the laser by the lens movements (see Fig.2.17) we can then centre the laser beam very precisely onto the X-ray illuminated volume, maximising the FOM signal, i.e. the temperature rise in the liquid.

As the laser spot in our experiments is slightly larger than the X-ray spot, only the central part of the laser excited sample is detected. Transverse gradients in the excitation level will thus be neglected in our data analysis.

2.4 Sample Environment for TR Studies on Liquids

In order to excite always a "fresh" sample, in our experiments it is essential to keep it flowing, to ensure the replacement of liquid between subsequent laser pulses at the 1KHz repetition rate. The stability of the flow and the solute concentration are very important parameters that strongly influence the signal to noise ratio. The details for each studied system will be given in the data analysis for each molecule.

2.4.1 Capillary and open jet

In our experiments we used two different set-ups, a capillary based system and an open-jet [9]. In the first the solution is circulated through a thin quartz capillary of 300μm diameter under a steady flow ($\sim$0.1ml/s speed) from a peristaltic pump. In the open-jet system, the capillary is removed and a stable jet is provided by a high-pressure slit nozzle (300μm, from Kyburz). This allows to use a tighter laser focus and the possibility of using more concentrated solutions, both leading to a better signal to noise ratio, and at the same time eliminating quartz scattering from the CCD data.

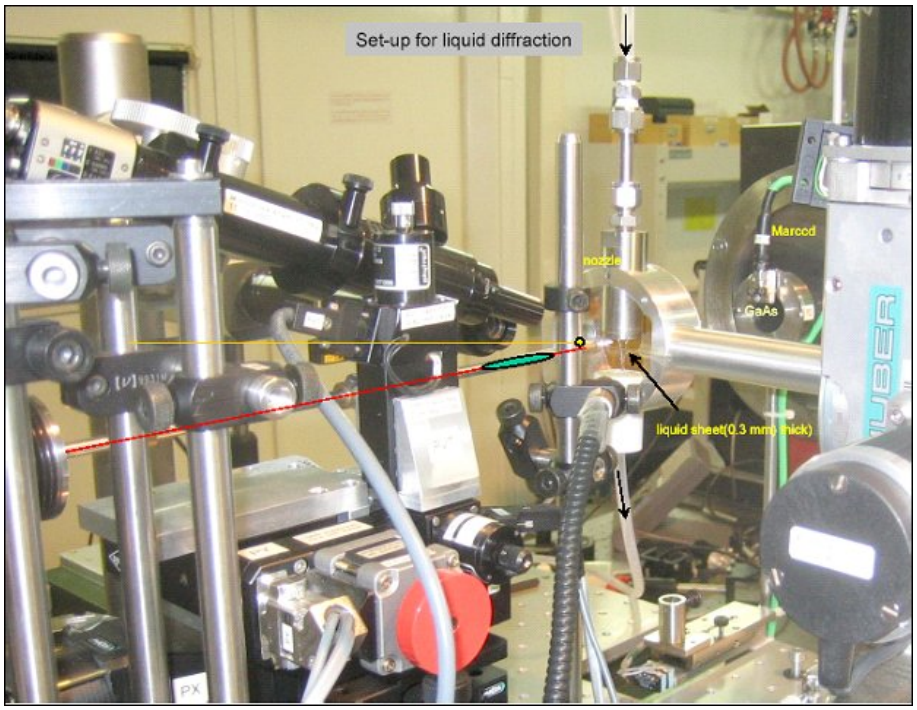

Figure 2.18: Photograph of the set-up for time resolved X-ray diffraction on liquids. The sample cell is the open-jet system. The X-ray and laser beams are drawn, as well as the flow of the sample. The GaAs detector used for measuring the time delay is also seen as well as the flat screen of the MARCCD.

2.4.2 Determination of the concentration

Here we want to discuss how to determine the best concentration for the solutions we intend to study. In general we need to find a good compromise between the signal to noise ratio, S/N, the solubility of the studied systems and the necessity of keeping a high dilution condition, in which the inter-solute contributions are negligible in the diffraction signal.

We can derive a theoretical expression for the S/N in our experiments, in which we are only interested in the diffraction signal from the excited solute molecules, such that

$$S = S(Q)_{exc\ solute}. \tag{2.29}$$

In order to keep the high dilution limit, in our typical experimental conditions the number of solute molecules N_{solute} is much smaller than the number of solvent molecules $N_{solvent}$

$$N_{solute} \ll N_{solvent} \tag{2.30}$$

so that we can assume the noise to be only the noise due to the solvent signal

$$N = \sqrt{S(Q)_{solvent}} \tag{2.31}$$

According to the considerations above we can write

$$\frac{S}{N} = \frac{S(Q)_{exc\ solute}}{\sqrt{S(Q)_{solvent}}}. \tag{2.32}$$

Moreover, we will assume that the number of excited solute molecules $N_{exc\ solute}$ is equal to the number of absorbed laser photons N^{abs}_{laser} (low power limit):

$$N_{exc\ solute} = N^{abs}_{laser} = N^{0}_{laser} - N^{trans}_{laser} = N^{0}(1 - e^{-\mu\ell}), \tag{2.33}$$

where in the above expression N^{0}_{laser} is the number of incoming laser photons (per pulse), N^{trans}_{laser} the number of transmitted laser photons. ℓ represents the thickness of the sample and μ is the absorption coefficient at the given laser wavelength.

We can then write the signal from the excited solute molecules and from the solvent molecules as

$$\begin{aligned} S(Q)_{exc\ solute} &= N^{0}_{X-ray} \cdot s(Q)_{exc\ solute} \cdot N_{exc\ solute} = \\ &= N^{0}_{X-ray} \cdot s(Q)_{exc\ solute} \cdot N^{0}_{laser}(1 - e^{-\mu\ell}) \end{aligned} \tag{2.34}$$

$$\begin{aligned} S(Q)_{solvent} &= N^{0}_{X-ray} \cdot s(Q)_{solvent} \cdot N_{solvent} = \\ &= N^{0}_{X-ray} \cdot s(Q)_{solvent} \cdot \ell \cdot A \cdot c_{solvent}. \end{aligned} \tag{2.35}$$

In 2.34 and 2.35, N^0_{X-ray} is the number of incoming X-ray photons (per pulse), $s(Q)_{exc\ solute}$ and $s(Q)_{solvent}$ are the diffraction signals per excited solute molecule and per solvent molecule. $N_{solvent}$ is the number of solvent molecules in the X-ray probed volume and $c_{solvent}$ the solvent concentration. A is the area of the X-ray illuminated sample. In this way, substituting in Eq.2.32 the signal to noise ratio is

$$\frac{S}{N} = \sqrt{N^0_{X-ray}}\ \frac{s(Q)_{exc\ solute}}{\sqrt{s(Q)_{solvent}}}\ N^0_{laser}\ \frac{1}{\sqrt{A \cdot c_{solvent}}}\ \frac{1-e^{-\mu\ell}}{\sqrt{\ell}}. \tag{2.36}$$

Obviously the S/N is optimised for high X-ray and laser fluxes. At a fixed ℓ (typically 300μm in our experiments) S/N increases with $\mu = n\sigma$, i.e. with the density n of solute molecules (where σ is the absorption cross section), as shown in Fig.2.19: higher concentration leads to a better signal to noise ratio.

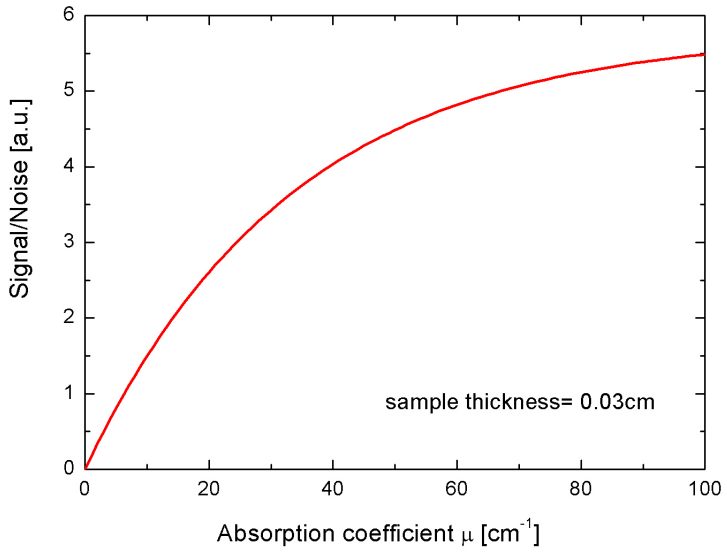

Figure 2.19: Signal to noise ratio as a function of the absorption coefficient μ.

The high dilution limit has nevertheless to be conserved because of the solubility and the possible observation of inter-solute correlations in the signal. These two effects cannot be easily quantified "a priori". It can be concluded that in our experiments the concentration of the solute has to be experimentally determined to maximise the photo-product yield while keeping the inter-solute contribution negligible [50]: this has to be done observing the diffraction signal at different concentrations and in principle choosing the highest possible one which is still in the safe limit of high dilution, i.e. for which we do not observe changes in the shape of the diffraction signal due to the appearance of solute-solute correlations.

2.5 Experimental parameters in the Br_2, HgI_2 and $HgBr_2$ experiments

In the previous sections we presented the data collection strategy which will be the same for all the time resolved diffraction studies performed in this work. We discussed also the general characteristics of the X-ray and laser beams and optics and the experimental set-up for liquid diffraction at ID09B. We want now to summarise the specific working parameters used in the three different experiments that we are going to discuss.

Characteristics of the X-ray beam	
Ring filling mode	16-bunch
Energy	E_f=18.2keV (undulator gap=9mm), ΔE/E=3%
Beam spot at the sample	100×60μm^2
Flux	$\sim$ 5×10^8 ph/pulse

Table 2.2: Characteristics of the probe X-ray pulses in the three experiments. All the experiments were performed in 16-bunch mode with the polychromatic X-ray beam produced by the mono-harmonic undulator U17 operated at 9mm gap.

Characteristics of the laser beam		
	Br_2 **in** CCl_4	$HgI_2/HgBr_2$ **in** CH_3OH
Excitation wavelength	400nm	267nm
Pulse duration	150fs	$\simeq$2ps
Pulse energy at the sample	130μJ	$\simeq$ 40μJ
Beam spot at the sample	150×120μm^2	100×100μm^2

Table 2.3: Characteristics of the pump laser beam in the three experiments. In the HgI_2 and $HgBr_2$ experiments the femtosecond laser pulse was temporally stretched by the passage through 30cm of fused silica to lower the peak power of the laser pulse and thus preventing multiphoton excitation.

Sample and sample environment	
	Br_2 **in** CCl_4
Concentration	138mM ($1Br_2$:$75CCl_4$)
Sample cell	Quartz capillary (thickness 300μm)
Sample-detector distance	43mm
Q-range	0.24 - 8.82Å^{-1}
	$HgI_2/HgBr_2$ **in** CH_3OH
Concentration	10mM ($1HgI_2$:$2500CH_3OH$) 25mM ($1HgBr_2$:$1000CH_3OH$)
Sample cell	Open jet (jet thickness 300μm)
Sample-detector distance	43mm
Q-range	0.24 - 8.82Å^{-1}

Table 2.4: The determination of the concentration was done according to section 2.4.2. Comments concerning the working concentrations will be however added in Chapter5. The sample cell systems are both described in the previous section 2.4. With the chosen detector distance the 2θ angle was recorded between 1.5° and 57.1°. The corresponding Q-range was 0.24 - 8.82Å^{-1}, calculated for a centre of mass wavelength of 0.681Å.

Data collection	**Time delays**	**Exposure Time**
Br_2 **in** CCl_4	-3ns/-100ps/100ps/200ps 500ps/1ns/2ns 5ns/7ns/10ns/25ns 50ns/100ns/1μs	6s
HgI_2 **in** CH_3OH	-3ns/-100ps/100ps/300ps 1ns/3ns/10ns 30ns/300ns/1μs	10s
$HgBr_2$ **in** CH_3OH	-3ns/-100ps/300ps/1ns 3ns/10ns/20ns 100ns/1μs	10s

Table 2.5: List of the exposure times and time delays collected to follow the structural evolution of excited Br_2, HgI_2, $HgBr_2$. The data point at -3ns where the X-ray pulses arrive 3ns ahead of the laser, was also collected for all the systems and used to check the noise floor of the experiment. The negative time delay at -100ps was collected to check against drifts in time zero to high resolution. To select the contributions only from structural changes due to the laser excitation and remove constant structural features, difference signals were generated by subtracting the reference data at -3ns from the data at each time delay.

2.6 Conclusions

In this chapter we have discussed the key elements of diffraction theory (2.1) that enable us to understand the structural information in a diffracted signal from a solution [39, 38]. We have linked the diffracted signal with the $g_{\alpha,\beta}(r)$ functions describing correlations between pairs of atoms in a liquid [43], eq.2.21: it has been emphasised that from X-ray scattering we measure the formfactor weighted sum of these and one cannot from one measurement alone recover the $g_{\alpha,\beta}(r)$. The structural information is encoded in the real space function $S[r]$ [20]. In order to study structural rearrangements of a photo-excited solute in solution taking place during a chemical reaction we use pump-probe diffraction to get difference maps $\Delta S(Q,\tau)$ [9, 51]. We made it clear that as the diffraction method is sensitive to all species in the solution unlike optical spectroscopy where the change in (bulk) solvent structure is typically silent. The photosignal has three components: the change in the solute structure, the change in the solvation cage due to the rearrangements of the solvent molecules around the new solute structures, and the bulk solvent response to heating and thermal expansion [9, 1, 64]. What is needed now is to develop a model that allows to disentangle the different contributions. We will see in the next chapter how we can calculate these three contributions using Molecular Dynamic (MD) simulations.

Chapter 3

The theoretical diffraction signal from a solution, including the interactions between solute-solute, solute-solvent, and solvent-solvent atoms can be obtained by Molecular Dynamics (MD) simulations. In this chapter we describe the basic principles of this computational technique. A very brief overview of the Density Function Theory which provides us the input parameters for the simulations is given. The Moldy software used in this work to perform the simulations is also illustrated. Through the propedaedeutical example of Br_2 in CCl_4 we discuss how we can build up step by step a complete theoretical model for the experimental difference diffracted signals. The simulated radial distribution functions and the theoretical diffracted intensities calculated for HgI_2 and $HgBr_2$ in CH_3OH are also shown.

Résumé du chapitre 3

Les signaux de diffraction par une solution, contenants toutes les interactions atomiques et moléculaires du système, c'est-à-dire les interactions entre les molécules soluté-soluté, entre les molécules soluté-solvant, et entre les molécules solvant-solvant peuvent être obtenus théoriquement grâce aux simulations de la Dynamique Moléculaire. Dans ce chapitre, nous allons introduire les principes fondamentaux de cette technique de simulation. La méthode de la Density Functional Theory, grâce à laquelle nous avons obtenu les paramètres initiaux pour les simulations, est très brièvement mentionnée et ainsi que le programme de simulation Moldy utilisé pour les simulations performées dans ce travail est également présenté. En fin de chapitre, la solution de Br_2 in CCl_4 est utilisée comme exemple didactique pour montrer comment il est possible, à travers ces simulations, de construire pas à pas un modèle théorique qui décrit les données expérimentales. Les fonctions de distribution radiale simulée et l'intensité diffractée théorisée calculées pour les molécules de HgI_2 et $HgBr_2$ dissolue dans CH_3OH obtenues grâce aux simulations y sont aussi exposées.

Chapter 3

Molecular Dynamics Simulations: theoretical diffracted signals from a solution

We saw previously how it is possible to calculate theoretically the change in diffraction signal $\Delta S(Q)$ from a change in molecular structure induced by the laser excitation of an isolated molecule in gas phase (Fig.2.7). And we mentioned that in liquids, the structural signal does not come only from the photo-induced structural change in the solute, but also from changes in the cage and the solvent response: we thus need to include these contributions in the theoretical model. The theoretical diffraction signal from a solution, including the interactions between solute-solute, solute-solvent, and solvent-solvent atoms can be obtained by Molecular Dynamics (MD) simulations. As we will see, the atom-atom distribution functions $g_{\alpha,\beta}(r)$ can be determined from MD: from these functions we can then, according to eq.2.21, calculate the $S(Q)$ in thermal equilibrium. Simulations need to be performed for the ground state of the system and for all putative reaction channels (i.e. for the system in higher electronic states, dissociated structures or in general for all possible transient structures that can be formed after excitation and during recombination), in order to obtain the difference maps, in the way that we will discuss in the next sections. The pursuing structural change in the solvent is driven by energy released from the reaction products and has to be included in the global fit self consistently. MD requires a structural description of the system: quantum chemistry calculations or very high resolution static diffraction data can provide this information.

3.1 Inputs for Molecular Dynamics simulations: quantum chemistry calculations

In this work the molecular structures and charges needed as input in the MD simulations have been provided by quantum chemistry calculations performed using Density Functional Theory (DFT) implemented in the code GAUSSIAN 94 [60].

Without going into details [61, 62, 63] of the computational methods, in Table 3.1, and Table 3.3, we summarised the structural parameters and charges obtained for Br_2 and CCl_4 molecules and for HgI_2 and $HgBr_2$ in CH_3OH. They will be used as input in the MD simulations which we are going to show in this chapter.

Very briefly, the basic principles of these calculations consist in using the laws of quantum mechanics: the energy, the angular moment, and other properties of a molecule may be obtained by solving the Schrödinger equation numerically:

$$\mathbf{H}\Psi = E\Psi.$$

The different methods are characterised by their mathematical approximations. Gaussian contains many theoretical models at different theoretical levels, which are usable for different size molecules and provide approximate solutions to the Schrödinger equation, i.e. they calculate molecular wavefunctions and energy levels etc. In any case a theoretical model should be uniquely defined for any given configuration of nuclei and electrons. This means that specifying a molecular composition is all that is required to produce an approximate solution of the Schrödinger equation and hence the molecular structure. Models are characterised by the combination of theoretical procedures and basis sets that are mathematical representations of the molecular orbitals within a molecule. The basis set can be interpreted as restricting each electron to a particular region of space. Larger basis sets impose fewer constraints on electrons and more accurately approximate exact molecular orbitals, requiring correspondingly more computational resources.

3.2 Basic principles of Molecular Dynamics simulations

The study of the liquid state of matter has a long and rich history theoretically as well as experimentally. Molecular Dynamics is a simulation technique introduced to obtain the statistical properties of an ensemble of interacting molecules [54]. In MD the classical Newton-Euler equations of motion for N molecules are solved in timesteps that are shorter than their collision times, typically every 0.5fs, in order to determine the trajectory of every single atom in the liquid. Therefore, MD programs calculate positions and velocities as function of time (discrete time points) of the atoms starting from a set of assigned velocities, usually drawn from a Maxwell-Boltzmann distribution, and an interaction potential between the particles. MD calculations are usually done

considering hundreds to thousands of molecules (from 256 to 2048 for instance) placed in a cubic cell at fixed volume with a side length of the order of a few tenths of Å^3. A simple, realistic and commonly used potential to describe the site-site interaction between two identical atoms in a liquid is the Lennard-Jones 12-6 potential,

$$\nu(r) = 4\epsilon \left[\left(\frac{\sigma}{r}\right)^{12} - \left(\frac{\sigma}{r}\right)^{6} \right], \tag{3.1}$$

This potential has a long-range attractive tail of the form $-1/r^6$, a negative well of depth ϵ at the minimum in $\nu(r)$, and a steeply rising repulsive wall at distances less than $r \sim \sigma$, the so-called collision diameter, or minimum approach distance, which represents the separation of two particles where $\nu(r) = 0$. This potential, as most of the pair potentials commonly used in computer simulations is approximate but it contains the salient features of real interactions in an empirical way. From the distribution of atom-atom positions we obtain the (time-independent) averaged atom-atom correlations $g_{\alpha,\beta}(r)$ which describes how the molecules correlate in the liquid phase. It is then possible to calculate the diffracted intensity of the system.

3.2.1 Moldy Software

We used the program Moldy developed by Keith Refson for simulating the spatial atom-atom correlations in solution. Moldy is designed to simulate a broad class of atomic or molecular systems [55] under the assumptions that the system is an assembly of rigid molecules, atoms or ions. The force fields are derived from continuous potential functions acting between the (usually) atomic sites on each molecule. Finally the dynamics are assumed to be governed by the classical Newton-Euler equations of motion. If we denote the force exerted by atom α in molecule i on atom β in molecule j by $\mathbf{f}_{i\alpha j\beta}$, then the total force acting on molecule i is

$$\mathbf{F}_i = \sum_j \sum_\beta \sum_\alpha \mathbf{f}_{i\alpha j\beta} \tag{3.2}$$

and the torque is given by

$$\mathbf{N}_i = \sum_\alpha (\mathbf{r}_{i\alpha} - \mathbf{R}_i) \times \mathbf{f}_{i\alpha} \tag{3.3}$$

where $\mathbf{R}_i = 1/M_i \sum_\alpha m_{i\alpha}\mathbf{r}_{i\alpha}$ is the centre of mass of molecule i. The motion is governed by the Newton-Euler equations

$$\begin{cases} M_i \ddot{\mathbf{R}}_i = \mathbf{F}_i \\ \mathbf{I}_i \cdot \dot{\boldsymbol{\omega}}_i - \boldsymbol{\omega}_i \times \mathbf{I}_i \cdot \boldsymbol{\omega}_i = \mathbf{N}_i \end{cases} \tag{3.4}$$

where $\dot{\boldsymbol{\omega}}_i$ is the angular velocity of the molecule, $\mathbf{I}_i = \sum_\alpha m_{i\alpha}(p_{i\alpha}^2 \mathbf{1} - \mathbf{p}_{i\alpha}\mathbf{p}_{i\alpha})$ is the inertia tensor and $\mathbf{p}_{i\alpha} = \mathbf{r}_{i\alpha} - \mathbf{R}_i$ is the atomic site coordinate relative to the molecular centre of mass. The orientations of the molecules are represented by quaternions, and the dynamical equations 3.4 are integrated using a modification of the Beeman

algorithm [55].
The forces determining the dynamics of the system are derived from the potential $\phi_{i\alpha j\beta}$. The indices i and j run over all the molecules in the system and α and β over the atoms in the respective molecules. The total potential energy of the system is

$$U = \sum_i \sum_{j>i} \sum_\alpha \sum_\beta \phi_{i\alpha j\beta}(\mathbf{r}_{i\alpha j\beta}), \tag{3.5}$$

where $\mathbf{f}_{i\alpha j\beta} = -\boldsymbol{\nabla}\phi_{i\alpha j\beta}(\mathbf{r}_{i\alpha j\beta})$ is the force acting on site β of molecule j from site α of molecule i. The total force and torque acting on any particular molecule are calculated using eq.3.2, 3.3. Since $\mathbf{f}_{i\alpha j\beta}$ and therefore $\mathbf{F}_{ij}$ are short-ranged forces (i.e. they decay faster than r^{-3}) one can define a cutoff radius, r_c. Interactions between sites whose separation r_{ij} is greater than r_c are assumed to be negligible and they do not need be evaluated. In the case of polyatomic molecules it is usual to apply the cutoff according to the intermolecular separation Rij. We already described the potential chosen for our systems; in addition to the short range potential, electric charges may be specified for each atomic site which interact according to Coulomb's law. These long range Coulomb interactions are handled using the Ewald sum technique [55].
It is convenient to conduct simulations in the NVT ensemble, where the number of atoms, the volume and the temperature of the system are fixed, and where the temperature is the supplied parameter, rather then the kinetic energy at thermal equilibrium. From the equipartition theorem every degree of freedom in the system has the same kinetic energy. The effective temperature of the system is then given by an ensemble average of its kinetics energy. The initial kinetic energy may be set approximately by choosing random velocities which sample the Maxwell-Boltzmann distribution at the desired temperature, and this is indeed what Moldy does on starting a new run. Since the initial configuration is usually very far from equilibrium, the sample will have too much potential energy. As the run progresses this will be converted into kinetic energy, raising the temperature above the desired value. It is therefore necessary to remove the excess kinetic energy to keep the temperature constant. Moldy offers different methods to control the temperature: velocity scaling is suitable during the equilibration period but it does not generate meaningful particle trajectories. The Nose-Hoover method, the one we used in our simulation after a few thermalization runs with velocity scaling, couples the system to a heat bath using a fictional dynamical variable [56].
Moldy allows any initial structure to be specified and replicated in the MD cell. In our simulations we started from a near-equilibrium crystal structure. The input parameters are the number, mass and position of the different atoms in the system, and their interactions. Finally, the initial centre-of-mass velocities are chosen from the Maxwell-Boltzmann distribution at the simulation temperature.

3.3 Example of simulated contributions: Br_2 in CCl_4

I will now show how we can calculate $\Delta S(Q,\tau)$ for a chemical transition from the $g_{\alpha,\beta}(r)$ curves from MD. In order to do this I will consider the photo-excited Br_2 in CCl_4. In the next chapters more details will be given including a discussion of the MD fits to the experimental data.
We saw before how the Debye formula gives the diffraction from (non-interacting) molecules in the gas phase (eq.2.12). If we consider the potential energy surfaces of Br_2 (Fig.1.1), we know that [Chapter 1] after the excitation to the Franck-Condon state the molecule explodes and the Br atoms collide with the cage molecules. Three possible outcomes are now possible: in some cases, highly vibrationally excited molecules Br_2^* are formed in the original X state. They relax along the X potential energy surface while transferring heat to the solvent. Alternatively they may relax to the A/A' excited state which has an elongated bond length of 2.7Å as compared to 2.3Å in the ground state. A smaller number of atoms will escape the cage and recombine with other Br atoms (non geminate recombination). We discussed the time scale of these processes in Chapter 1: with our time resolution we see what happens from about 100ps after excitation, which means that we only probe the tail of the cooling phase to the ground state where the vibrational amplitude is small (weak signal). When we start probing the system after 100ps, we expect to find a mixture of Br_2^* molecules in the A/A' state and Br atoms contributing to the difference signal. Therefore from eq.2.12 we can calculate $S(Q)$ for Br_2 in its ground state, in the A/A' excited state and for atomic Br and by subtracting the groundstate $S(Q)$ from these curves we obtain the theoretical $\Delta S(Q)$ for each excited state shown in Fig.2.7. We can then make a linear combination of these generic curves in order to fit the data, the fitting parameters being the percentage of molecules in each state. The 100ps time delay is shown in Fig.3.1.

The experimental data in Fig.3.1 is scaled to the theoretical difference Debye scattering from independent gas molecules. What is seen immediately is that the high-Q part fits well whereas the low-Q part deviates substantially. The reason is that the high-Q part probes predominantly atom-atom correlations in the Br structures, whereas at lower Q, the X-rays probe the longer lengths scales associated with solute-solvent and solvent-solvent terms. To quantify the low-Q range 0.1-4 $Å^{-1}$ we need input from MD which will be described below.

3.3.1 Solute and cage

I will now show the results of three MD simulations one for the groundstate $Br_2(X)$ in CCl_4, one for $Br_2(A/A')$ in CCl_4, and the last one for atomic Br in CCl_4. The input parameters are the following:

- the linear Br_2 molecule is formed by two neutral Br atoms interacting through a Lennard-Jones potential (eq.3.1) with the parameters given in [54].
- The Br-Br distance in the ground and excited state are known from quantum

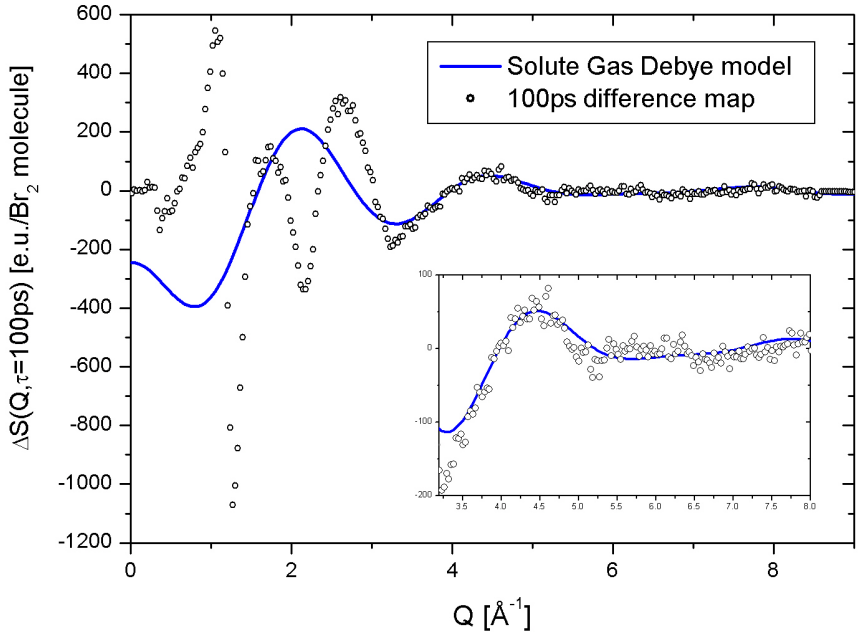

Figure 3.1: First attempt to fit the experimental $\Delta S(Q, 100ps)$ to molecular gas-phase transitions. Note the striking discrepancy at low Q region and the good agreement for $Q > 4\text{Å}^{-1}$ which we can describe as the "molecular gas-phase region" where atom-atom correlations from the breakage and formations of bonds dominate. The fit neglects the cage and the solvent. The theoretical curve has been calculated with 55% of the Br_2 molecules in the X state, 35% in the A/A' state and 10% of atomic Br. The complete fit and results will be shown in Chapter5.

3.3. Example of simulated contributions: Br_2 in CCl_4

Atom	x	y	z	mass [g/mol]	charge [e]
C	0	0	0	12.0107	0.248
Cl_1	1.8	0	0	35.4527	-0.062
Cl_2	-0.6	1.697056	0	35.4527	-0.062
Cl_3	-0.6	-0.848528	1.469694	35.4527	-0.062
Cl_4	-0.6	-0.848528	-1.469694	35.4527	-0.062
Br	0	0	0	79.904	0
Br	2.33(X state) / 3(A/A' state)	0	0	79.904	0

Table 3.1: Structural parameters, mass and charges for Br_2 and CCl_4 molecules used in the MD simulations.

Atomic pair	4ϵ [kJ/mol]	σ [Å]	Atomic pair	4ϵ [kJ/mol]	σ [Å]
$C-C$	0.838	3.80	$Br-Br$	8.552	3.54
$C-Cl$	1.932	3.635	$Br-C$	2.676	3.67
$Cl-Cl$	4.457	3.47	$Br-Cl$	6.176	3.505

Table 3.2: Parameters for the pair-pair Lennard-Jones potential used to simulate the interactions in a solution of Br_2 in CCl_4.

chemical calculations [16] and the simulations have been performed for the ground state, the A/A' state and the Br atomic state.

- The solvent's molecular structure and the potential parameters are given in [58].
- The Lorentz-Berthelot mixing rules are used:

$$\epsilon_{a,b} = \sqrt{\epsilon_{a,a} \cdot \epsilon_{b,b}} \qquad \sigma_{a,b} = \frac{\sigma_{a,a} + \sigma_{b,b}}{2}. \tag{3.6}$$

Tables 3.1, 3.2 summarise the input parameters, the structure of the molecules and their interaction potential.

The time step in the simulation is 0.5fs, and the atomic positions are recorded in the computer memory every 100 steps. The calculation of the radial distribution functions is done according to the ergodic principle stating that the MD sampling in time after millions and millions of collisions gives $g_{\alpha,\beta}(r)$ in thermal equilibrium. We performed MD simulations for 1 Br_2 molecule (X and A/A' state) and 1 Br atom in 2048 CCl_4 molecules, averaged over 1.8ns of dynamics after thermalization.

In Fig.3.2 we show the site-site pair correlation functions obtained from these simulations.

Fourier transforming the distribution functions to Q-space we obtain the total intensity and its atom-atom components eq.2.21.

We will now examine how MD describes the solute-solvent interaction, i.e. the cage, which is described by the terms $g_{Br-C}(r)$, $g_{Br-Cl}(r)$.

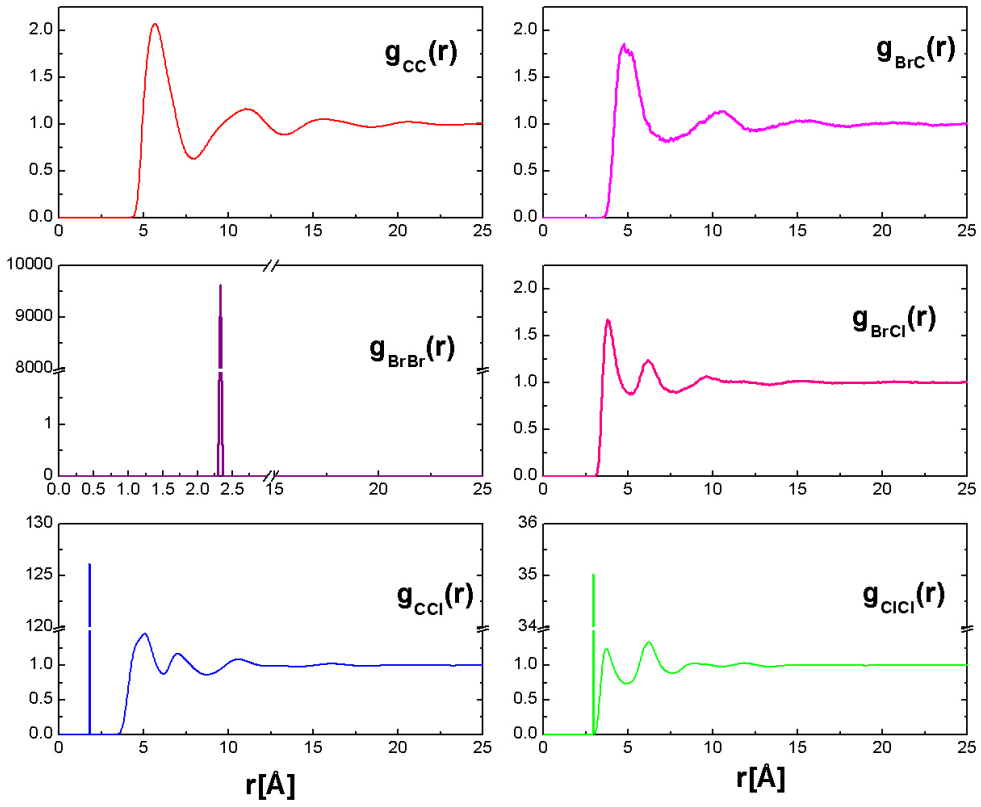

Figure 3.2: Radial distribution functions from the MD simulation of 1 Br_2 molecule in the ground state in a solution of 2048 CCl_4 molecules.

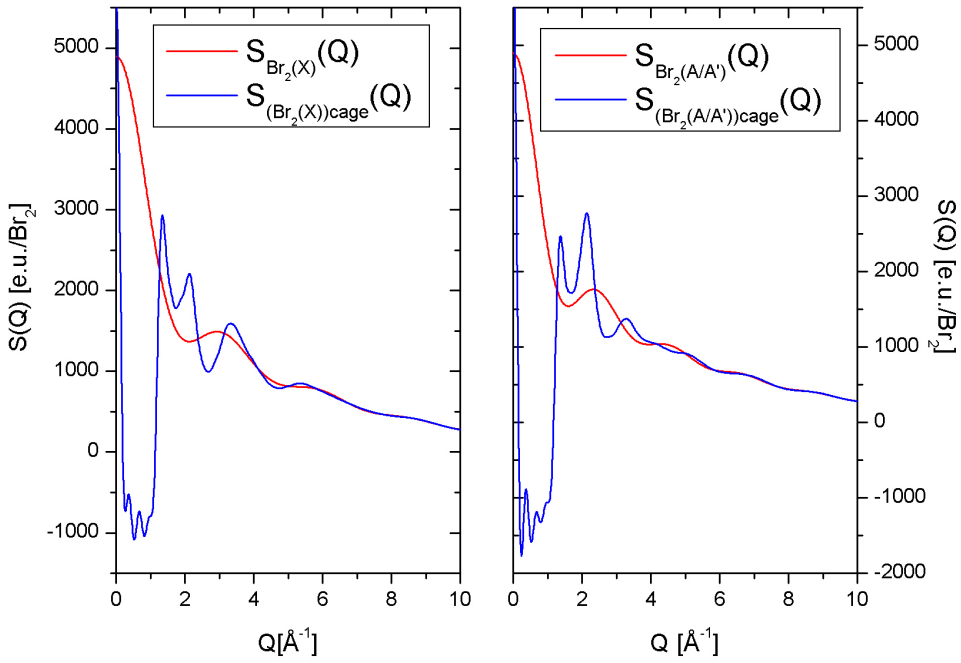

Figure 3.3: MD simulated diffraction intensities from Br_2 in X and A/A' including the cage, compared with the gas phase Debye scattering.

In Fig.3.3 we show the differences between the caged curves with those of isolated Br_2 gas molecules, and demonstrate that, as expected, the cage modifies the low Q range, Q <4Å^{-1}, i.e. in the intermolecular region. The low Q region Q <1Å^{-1} is probably unphysical due to the limited box size in MD (34Å).

It is also interesting to examine the cage size for a Br atom and Br_2 molecule. In fig.3.4 we plot the $g_{Br-Cl}(r)$ correlation in the case of a Br_2 molecule and a Br atom in 2048 CCl_4. The $Br-Cl$ correlation peak is at 3.80Å for the molecular bromine and at 3.73Å for Br, showing how the solvent comes closer to atomic bromine as expected, (even if this number cannot be considered a measure of the cage radius). Nevertheless, before performing a fit with these MD simulated $\Delta S(Q)$ functions we need to include the solvent response to a change in temperature from recombining Br_2.

3.3.2 Pure solvent

We already mentioned the changes in the diffracted intensities from the changes in solvent temperature and its time scale. After the laser excitation to the Franck-Condon state above the groundstate minimum, the Br_2 molecule dissociates into two neutral Br atoms in the cage. Laser spectroscopic studies have shown that the Br-Br bond is reformed in 1-2ps or, for a small fraction of molecules, a Br atom leaves the cage. The energy transferred to the solvent in this time window is the laser energy minus the dissociation energy. This energy can be considered a side product of the laser excitation which can not be avoided. Now, a large fraction of the excited hot bromine molecules relax back to the ground state through fast vibrational relaxation. The

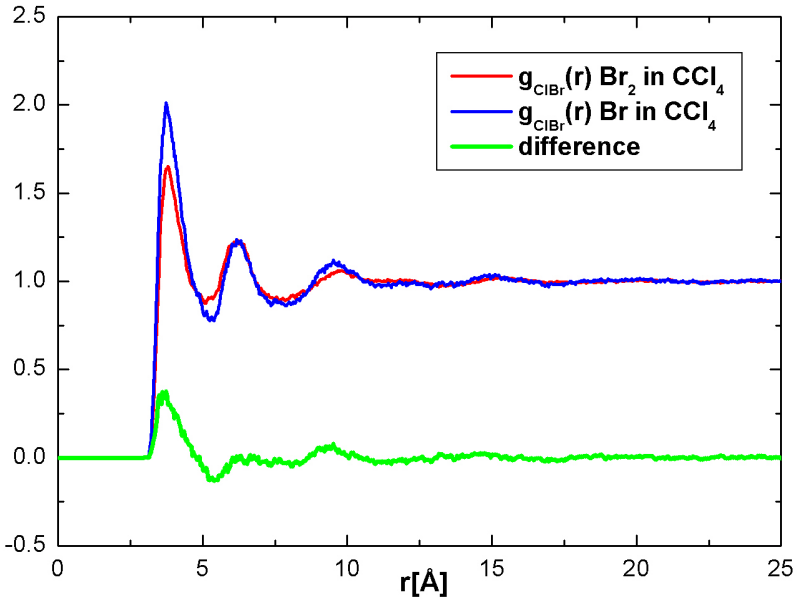

Figure 3.4: Comparison between the solute-solvent correlations for molecular and atomic bromine as obtained from a MD simulation of 1 solute in 2048 solvent molecules. The peak in the $g_{Br-Cl}(r)$ function is found at 3.80Å for Br_2 and 3.73Å for Br. Even if this is not a measure of the cage radius, nevertheless this suggests a smaller cage around the smallest solute.

energy difference decays exponentially in time with a 140ps time constant and causes a local temperature rise of the solvent. Probing at a delay of $\simeq$ 100ps, our experimental intensities will have a contribution from the temperature change of the solvent, at constant volume, $(\frac{\partial S}{\partial T})_V$. The time scale for expansion relaxation, in contrast, is linked to the release of the pressure gradient in the laser spot, which generates a density wave that travels outwards at the speed of sound. Then after typically 50ns for our sample dimensions the over-pressure is released, and the (adiabatic) expansion reestablishes the ambient pressure. After this time point, also called the acoustic horizon, we will see a change in the solvent due to thermal expansion, so it is needed to include a $(\frac{\partial S}{\partial V})_T$ (or $(\frac{\partial S}{\partial \rho})_T$) contribution to simulate the total solvent response. In general the temporal evolution of the solvent response is a linear combination of two structure differentials in two independent thermodynamical parameters, arbitrarily chosen amongst density, temperature and pressure. It can be shown by solving the hydrodynamic equations, that for time delays sufficiently short the solvent is heated at constant volume. This assumption is valid for $t < \tau_L = L/c$, where τ_L is the so-called Longaker-Litvak time, L is laser beam size and c the speed of sound in the liquid. In our experiment τ_L is typically $\sim 50ns$.

Following the approach outlined by Fabien Mirloup [57], we can simulate the two differentials by means of four different MD calculations performed for the same pure solvent system (CCl_4) at two different temperatures T_1 and T_2 and two volumes V_1 and V_2 , chosen such that the pairs (V_1, T_1) and (V_2, T_2) have the same pressure (1atm). In this way we can get the two differentials

$$\left(\frac{\partial S_{CCl_4}(Q)}{\partial T}\right)_V, \qquad \left(\frac{\partial S_{CCl_4}(Q)}{\partial V}\right)_T,$$

describing the changes in the solvent, Fig.3.5.

The four simulations for the pure solvent have been performed with the same structures and potentials of Tables 3.1, 3.2. Using the Rackett's formula [59]

$$V(T) = A_2 A_1^{1+(1-T/T_C)^{2/7}},$$

where V(T) is the molar volume in m^3 and for CCl_4 $A_1 = 0.27222$, $A_2 = 0.10140 \cdot 10^{-2}$ $T_C = 556.37$ [59], to calculate the volume at different temperatures at ambient pressure, we simulated 2048 CCl_4 molecules at $T_1 = 300K$, $T_2 = 328K$, $\rho_1 = 1.528 g/cm^3$, $\rho_2 = 1.581 g/cm^3$. The radial distribution functions are shown if Fig.3.6.

The sharp peaks in the $C - Cl$ and $Cl - Cl$ functions are due to the very strong atom-atom correlation inside the CCl_4 molecule. From the MD data in Q space we can decompose the liquid scattering of CCl_4 into atom-atom partial contributions, as shown in the upper panel of Fig.3.7

Indeed, we observe in the upper panel of Fig.3.7 that the first peak in the total intensity ($Q \sim 1.3$ Å^{-1}) contains contributions from all the three intermolecular components $C - C$, $C - Cl$, $Cl - Cl$, while the second peak ($Q \sim 2.5$ Å^{-1}) is related to smaller distances than 4Å, and it is dominated by the $Cl - Cl$ and $C - Cl$ interferences.

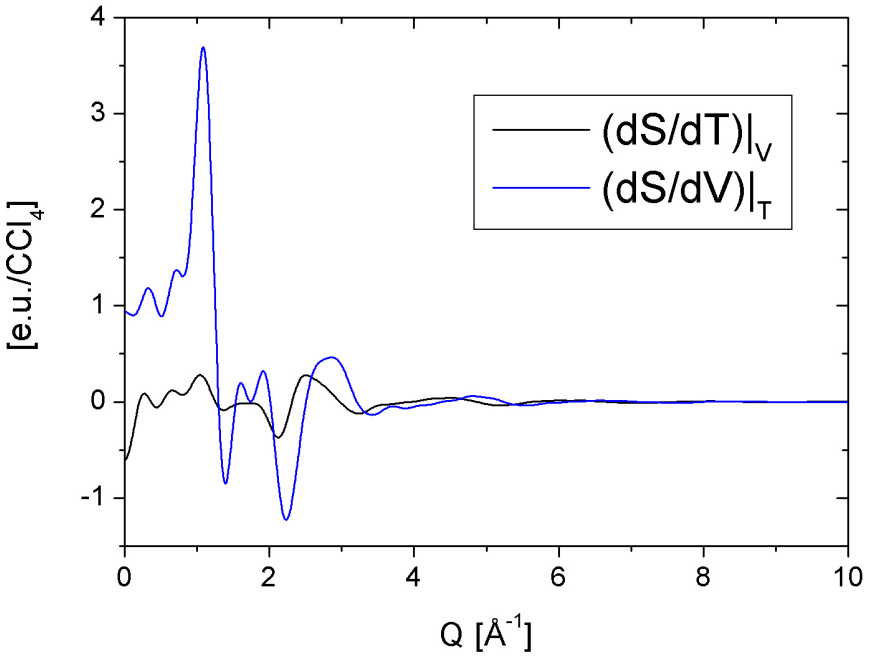

Figure 3.5: Simulated structural changes of the pure solvent.

The shoulder at ~ 3 Å^{-1} is related to smaller distances than 3.5Å, i.e. it is due to the $Cl-Cl$ correlations. The oscillations at higher Q are the signatures of the intramolecular distances. Furthermore we also note that the biggest contribution to the total intensity is given by the $Cl-Cl$ component, simply because of the high number of electrons ($Z=17$) of chlorine. With the lower plot in Fig.3.7 we show a comparison between the scattered intensity from the a CCl_4 molecule in different states, the liquid phase, the molecular gas phase and the dissociated atomic gas phase. For $Q > 4$ Å^{-1}, the intermolecular distances are no longer involved, the gas and liquid phase are almost identical, and for $Q > 6$ Å^{-1} the three curves converge towards the atomic gas limit. From the four MD simulations of $S(Q)$ we can finally extract the differentials we need to fit our data. In particular we can calculate the two contributions as:

$$\begin{aligned}\left(\frac{\partial S_{CCl_4}(Q)}{\partial T}\right)_V &= \frac{1}{2}\left(\frac{S_{CCl_4}(V_1,T_2,Q)-S_{CCl_4}(V_1,T_1,Q)}{T_2-T_1}+\right.\\ &\left.\frac{S_{CCl_4}(V_2,T_2,Q)-S_{CCl_4}(V_2,T_1,Q)}{T_2-T_1}\right),\\ \left(\frac{\partial S_{CCl_4}(Q)}{\partial V}\right)_T &= \frac{1}{2}\left(\frac{S_{CCl_4}(V_2,T_1,Q)-S_{CCl_4}(V_1,T_1,Q)}{V_2-V_1}+\right.\\ &\left.\frac{S_{CCl_4}(V_2,T_2,Q)-S_{CCl_4}(V_1,T_2,Q)}{V_2-V_1}\right).\end{aligned} \tag{3.7}$$

Note that two simulations would have been sufficient to calculate the differentials,

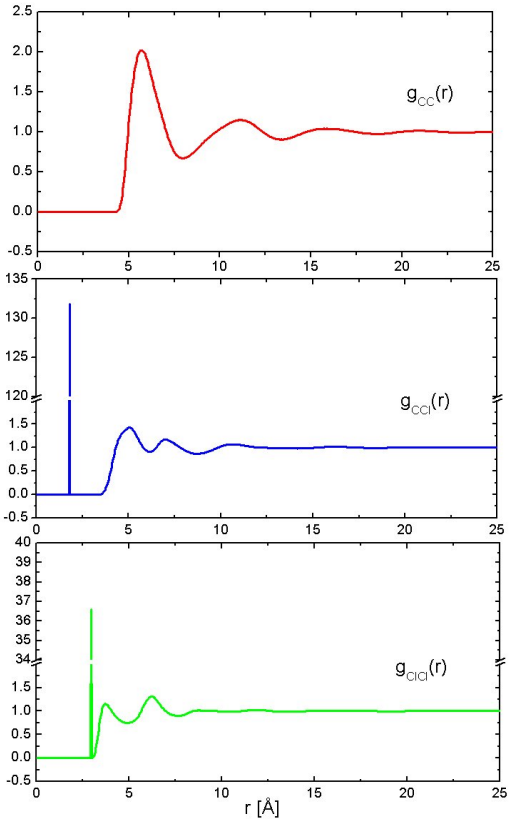

Figure 3.6: Radial distribution functions for 2048 CCl_4 molecules obtained after 1.8ns of MD simulations.

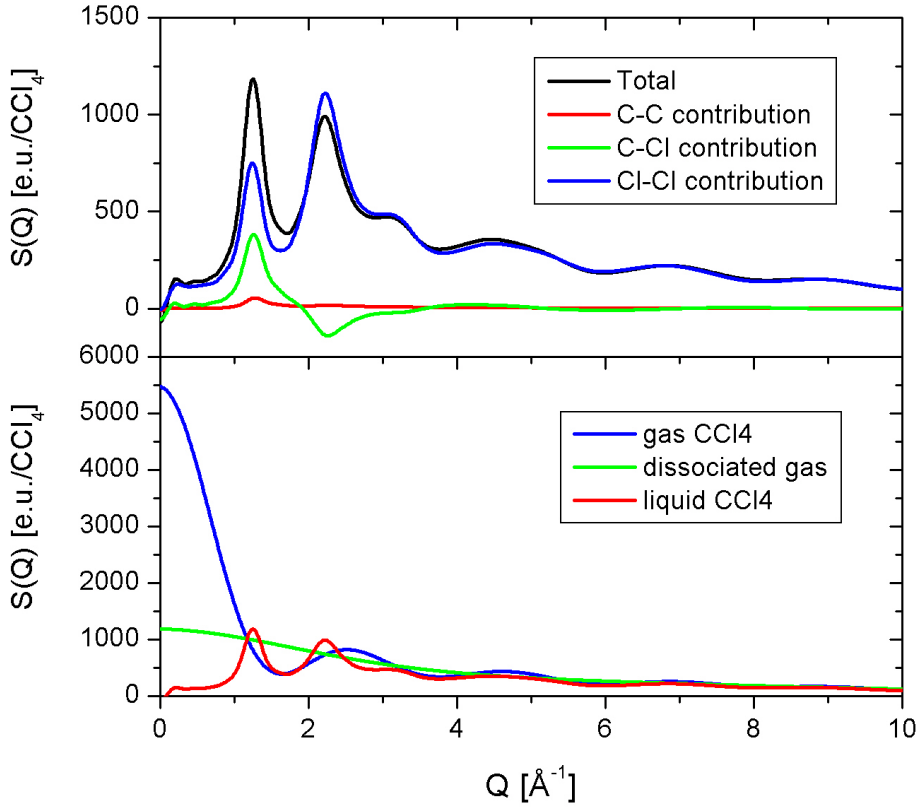

Figure 3.7: Total scattered intensity from a CCl_4 molecule and its partial components. Comparison with different CCl_4 states.

but we can reduce the errors by using all four MD simulations [57]. In Fig.3.8 we see immediately the improvements in the fit of $\Delta S(Q, 100ps)$ by adding the MD solvent response, in particular at low Q, as compared to the fit obtained without including the solvent terms (Fig.3.1). Note that in converting $\Delta S(2\theta, \tau)$ to $\Delta S(Q, \tau)$ we have replaced the tooth-shaped undulator spectrum with an effective energy E_{COM}. In the next chapter we will give more details on how we correct the theory to match the experimental X-ray spectrum. The final fit with the calculated cage and solvent term is shown in Fig.3.9.

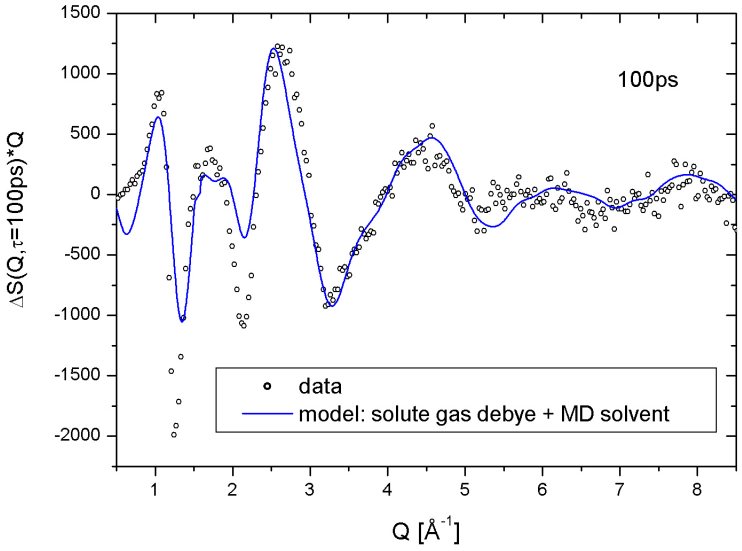

Figure 3.8: In the second model the $\Delta S(Q, 100ps)$ is fitted to gas-phase transitions from Fig.3.1 and MD solvent response. Note the striking improvement at low Q as compared to the fit obtained without including the solvent contributions (Fig. 3.1).

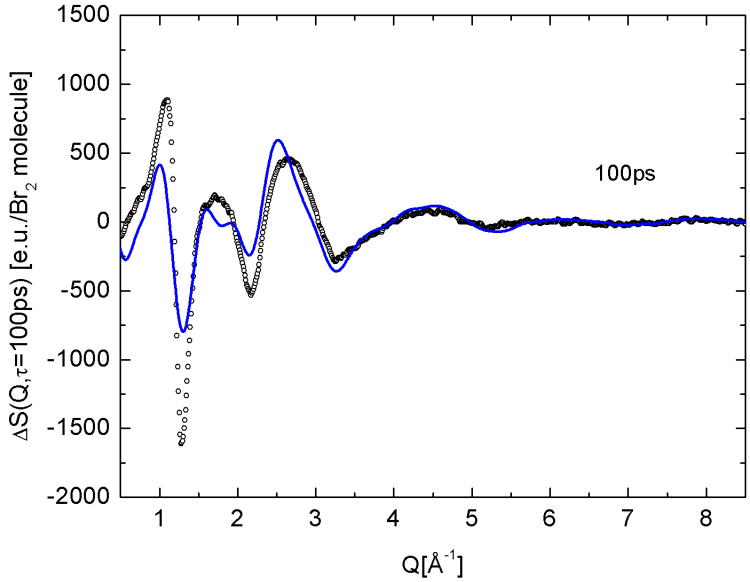

Figure 3.9: Complete model including the theoretical MD diffracted intensity of Br_2 in CCl_4 in the groundstate, in the A/A' excited state and in the dissociative atomic state plus the MD simulated solvent response. The discrepancy between the model and the data is probably due to imperfect solvent potentials in the MD simulations that are "amplified" in the solvent differential $(\frac{\partial S}{\partial T})_V$.

3.4 HgI_2 and $HgBr_2$ simulations

The aim of the previous paragraphs was to understand, by means of the Br_2 in CCl_4 example, how to use MD to calculate the diffracted intensity in liquid phase. The detailed analysis of the fits for all the molecular systems in this thesis will be discussed later. We report here also the parameters used for the MD simulations of HgI_2 and $HgBr_2$ in CH_3OH and we will show the results obtained. As we will explain in Chapter 5 we will use these results to build up the theoretical model to fit the data. In the case of these two systems the intermolecular correlations of the solute and photoproducts with the solvent were simulated by MD using the MOLDY [55], and the so-called H1 methanol model (where the methyl group CH_3 is considered as one effective atom) [80] was used. The pure solvent response will be treated separately as we will see in the next chapter. For the MD simulation of the diffraction from the solute in its cage, we used 1 solute (HgI_2, HgI, HgI-I(isomer), I, I_2) surrounded by 512 methanol molecules in a cubic box of ∼30Å. In the case of $HgBr_2$ we performed simulations on a smaller system, with 1 solute ($HgBr_2$, HgBr, Br, Br_2) in 256 methanol molecules, with a simulation box of ∼25Å. The structures of the solute molecules in methanol and the charges on the atoms were obtained from DFT calculations (see Table 3.3) by Qingyu Kong and Hyotcherl Ihee's group at Kaist [32], and they were kept constant during the simulation.

Specie	Hg-I [Å]	I-I [Å]	I-Hg-I [°]	Hg-I-I [°]	Relative energy [kJ/mol]
HgI_2	2.649	5.298	180	-	0.0
$HgI-I$	2.752	2.974	-	179.62	356.8
HgI	2.770	-	-	-	-
I_2	-	2.7	-	-	-
$HgI+I$	-	-	-	-	316.6
$Hg+I_2$	-	-	-	-	367.1
$Hg+2I$	-	-	-	-	559.3

Specie	Hg-Br [Å]	Br-Br [Å]	Br-Hg-Br [°]	Relative energy [kJ/mol]
$HgBr_2$	2.349	4.698	180	0.0
$HgBr$	2.807	-	-	-
Br_2	-	2.3	-	-
$HgBr+Br$	-	-	-	160.04
$Hg+Br_2$	-	-	-	251.55
$Hg+2Br$	-	-	-	449.96

Table 3.3: Summary of the structural parameters and energies for various molecular species calculated from density functional theory and used in MD simulations.

We noted in both cases the elongation in the Hg-X bondlength in the radical as compared to the bondlength in the HgX_2 molecule. We attribute that to the fact that a non-paired electron in the radical is in an anti-bonding state, and thus causing the elongation.

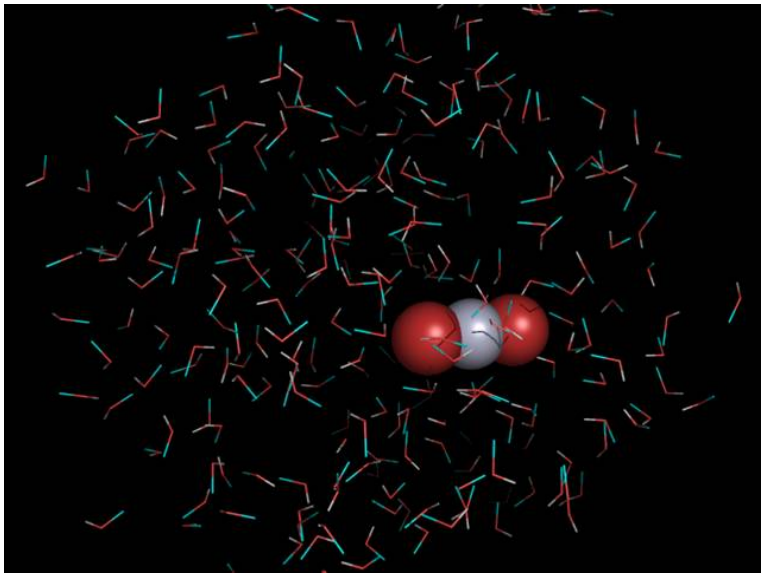

Figure 3.10: Snapshot of the simulation box after 500ps with 0.5fs timestep for 1 $HgBr_2$ molecule in 256 CH_3OH. The solvent molecules are shown in a stick presentation for transparence.

All simulations were performed at ambient temperature (300K) with a density of $0.790 g/cm^3$ and in both cases the system was equilibrated at 300K over 200ps at constant temperature via coupling to a Nose-Hoover thermostat [55, 56]. The time-step was 0.5fs and the simulations were performed in the NVT ensemble and the trajectories were followed up to 1ns. In Fig.3.11, 3.12 the solute-solvent $g_{\alpha,\beta}(r)$ functions for HgI_2 and $HgBr_2$ in methanol obtained from the simulations are shown.

The scattered intensity from each molecular configuration was calculated from the atom-atom distribution functions $g_{\alpha,\beta}(r)$ according to the relation, using tabulated atomic formfactors [40]. In Fig.3.13 and 3.14 we show the calculated S(Q) for the different considered solutes (Debye intensities) and the cage terms, i.e. the S(Q) calculated starting from the solute-solvent $g_{\alpha,\beta}(r)$.

Fourier transforming the cage terms from Q to real space we can obtain the S[r] terms for the cage of each solute molecules. In Fig.3.15 and 3.16 we show a comparison respectively between the HgI_2 and HgI real space cage term and the $HgBr_2$ and $HgBr$ real space cage term. According to what we already observed in the case of Br_2 and Br (see Fig.3.4) we observe a peak for the cage at lower r for the smaller solute, indicating that the solvent can come closer to the smallest solute.

Eventually, from the simulated intensities we can obtain the difference intensity curves for each possible dissociation channel that we want to include in the theoretical model to fit the data as we will see in Chapter 5.

In Fig.3.17 and 3.18 we show the simulated $\Delta S(Q)$ for the dissociation pathways $HgI_2 \rightarrow HgI + I$ and $HgI_2 \rightarrow HgI + 1/2I_2$, and $HgBr_2 \rightarrow HgBr + Br$, $HgBr_2 \rightarrow HgBr + 1/2Br_2$.

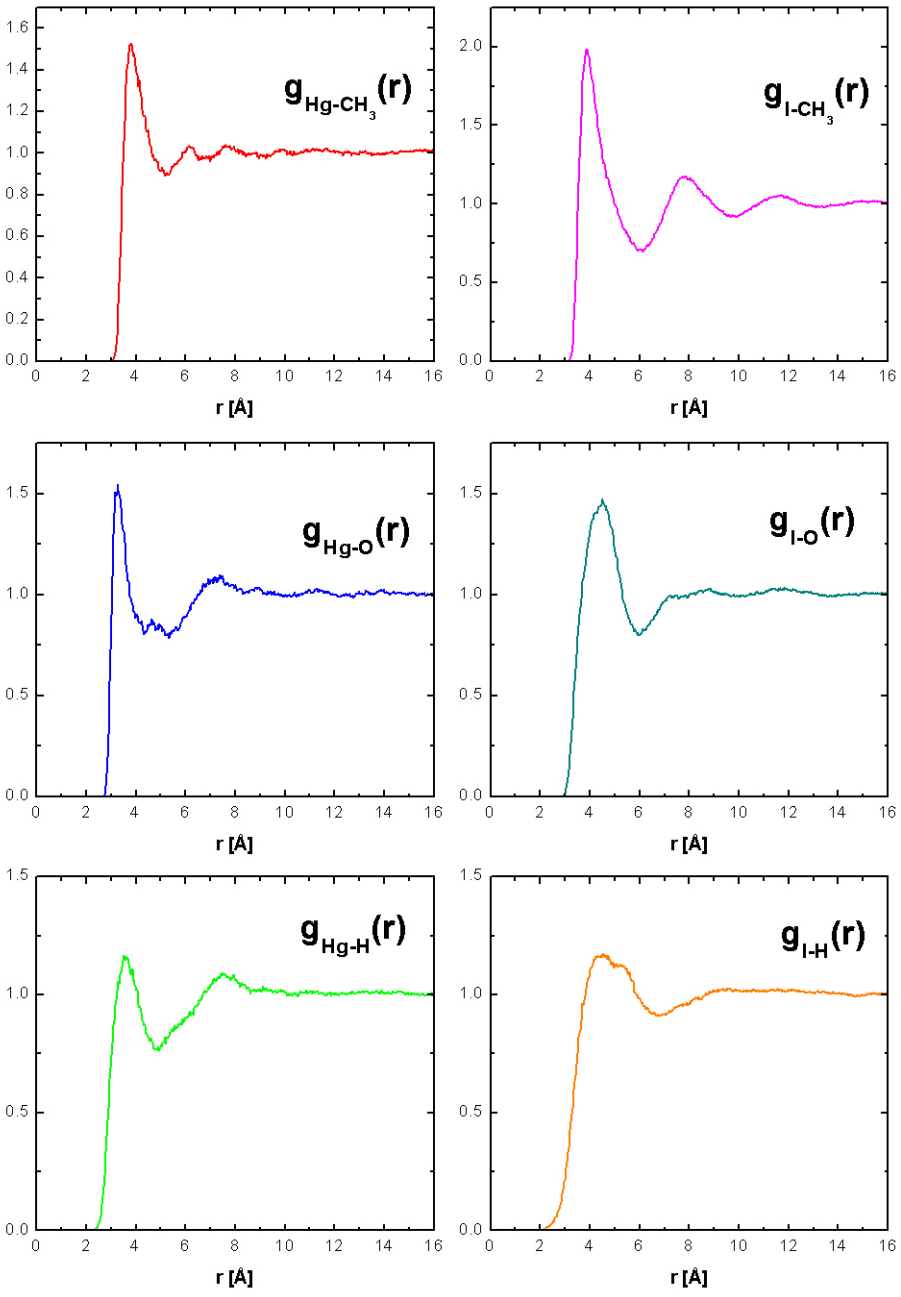

Figure 3.11: Simulated solute-solvent $g_{\alpha,\beta}(r)$ functions for HgI_2 in methanol.

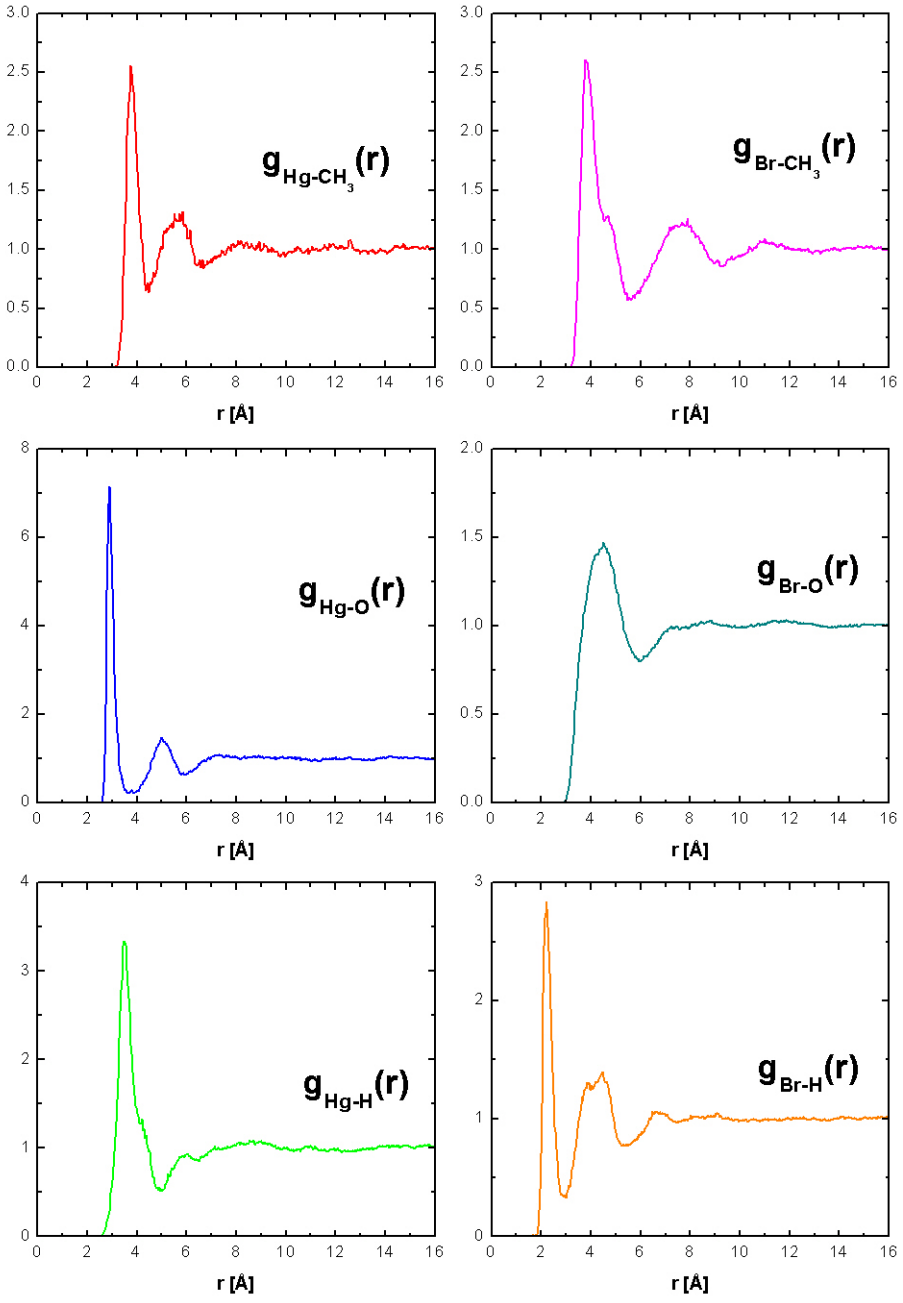

Figure 3.12: Simulated solute-solvent $g_{\alpha,\beta}(r)$ functions for $HgBr_2$ in methanol.

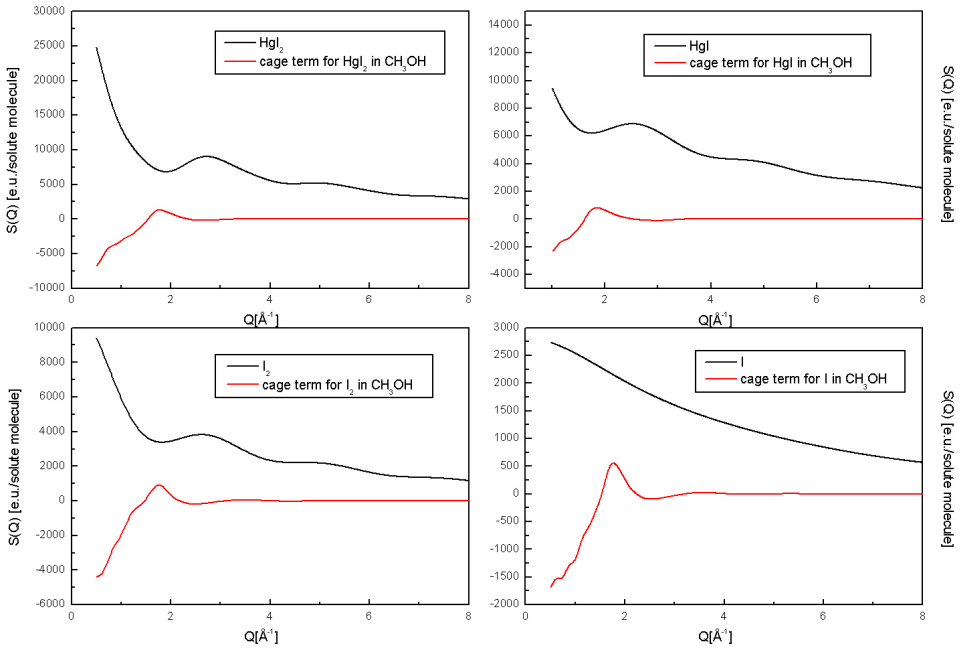

Figure 3.13: S(Q) intensities obtained from the simulated $g_{\alpha,\beta}(r)$ functions for HgI_2, HgI, I and I_2 in CH_3OH. The black curves represent the diffraction signal from the solute-solute interactions (i.e. the Debye scattered intensities) while the red curves represent the cage term, i.e. the diffraction signal from the solute-solvent interactions.

3.5 Conclusions

We gave in this chapter a short overview on the Molecular Dynamics computational technique, which allows us to simulate the partial diffracted signals from a solution, taking into account all the interactions in the system. As example, we showed the simulated atom-atom distribution functions for Br_2 in CCl_4 and pure CCl_4. We stressed the achievable information on the cage and the solvent response. From the radial distribution functions we calculated the theoretical diffracted intensities for X-rays. The results of different simulations for all the possible transient structures of a system can be combined to determine the relative transitions in the diffracted intensities. In the next chapters we will apply this method to the three molecular systems studied in this thesis. The molecular structures and charges used as input of the MD simulations performed for the three systems studied in this work were obtained from quantum chemistry calculations and have been summarised here together with the results of the simulations. We will then use the MD curves to build up the theoretical model against which we will fit the experimental data as we will explain in Chapter5.

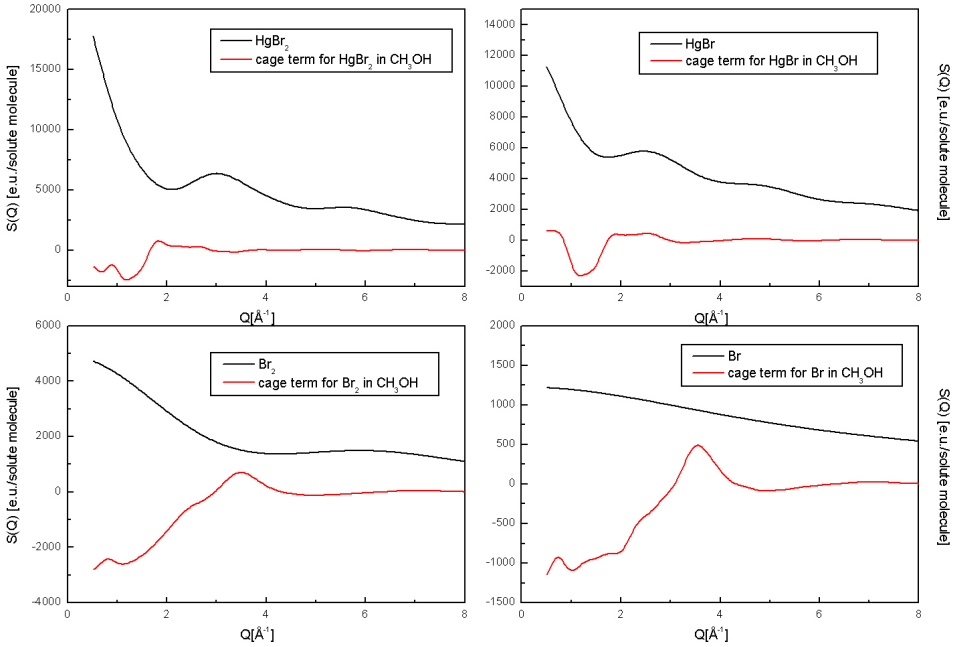

Figure 3.14: S(Q) intensities obtained from the simulated $g_{\alpha,\beta}(r)$ functions for $HgBr_2$, $HgBr$, Br and Br_2 in CH_3OH. The black curves represent the diffraction signal from the solute-solute interactions (i.e. the Debye scattered intensities) while the red curves represent the cage term, i.e. the diffraction signal from the solute-solvent interactions.

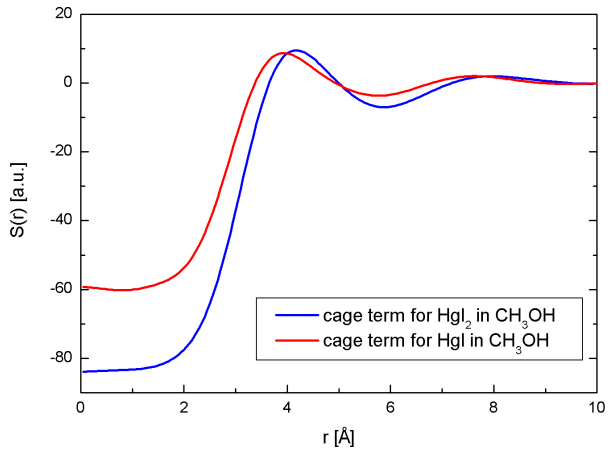

Figure 3.15: Comparison between the cage term in real space for HgI_2 and HgI. The radius of the cage is smaller for the smaller HgI solute.

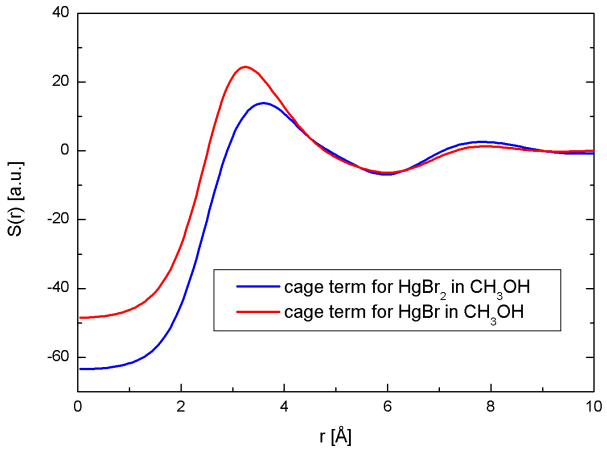

Figure 3.16: Comparison between the cage term in real space for $HgBr_2$ and $HgBr$. The radius of the cage is smaller for the smaller $HgBr$ solute.

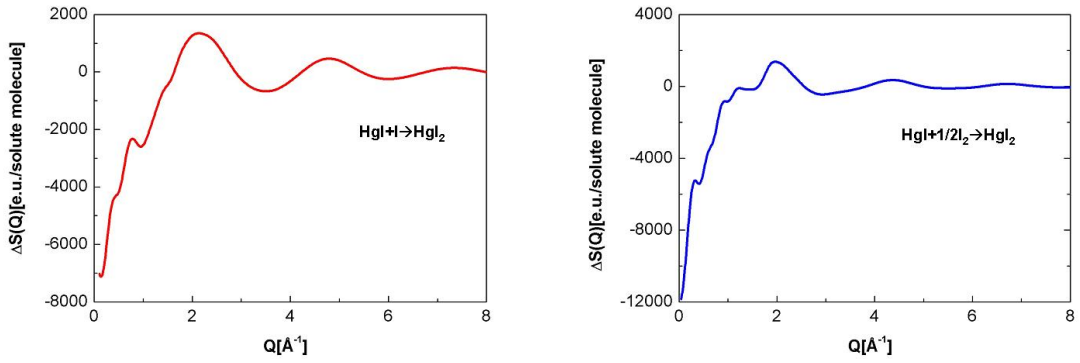

Figure 3.17: Simulated $\Delta S(Q)$ for the $HgI_2 \rightarrow HgI + I$(left) and $HgI_2 \rightarrow HgI + 1/2I_2$ dissociation channels.

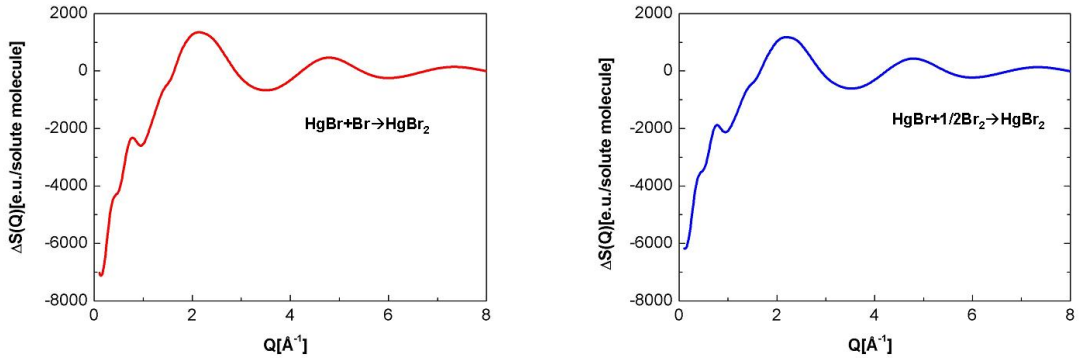

Figure 3.18: Simulated $\Delta S(Q)$ for the $HgBr_2 \rightarrow HgBr + Br$ (left) and $HgBr_2 \rightarrow HgBr + 1/2Br_2$ dissociation channels.

Chapter 4

In Chapter 4 we present the results of a static high-energy x-ray diffraction experiment on pure CCl_4 and Br_2 in CCl_4 which provide us a very precise structure determination of the pure solvent and solution. We also show the experimentally measured solvent response to induced ultrafast impulsive heating for pure CH_3OH obtained using Near Infrared (NIR) radiation. This experiment allowed us to achieve the solvent differentials needed to determine the time dependence of the temperature rise in the solvent during a chemical reaction. These results will be thus used to model the solvent response in the reaction dynamics of HgI_2 and $HgBr_2$.

Résumé du chapitre 4

Le quatrième chapitre est consacré à la description de deux expériences effectuées. D'abord, nous allons présenter les expériences de diffraction statique de rayons X de très haute énergie effectuées sur CCl_4 et sur une solution de Br_2 in CCl_4, qui nous ont permis de déterminer très précisément la structure de ce solvant et de la solution, et d'utiliser après ces informations dans l'interprétation des données obtenues par les mesures de diffraction résolue en temps. Ensuite, la mesure de la réponse expérimentale de CH_3OH au réchauffement impulsif provoqué par radiation infrarouge d'un laser femtoseconde y est aussi décrite et commentée. Les résultats de cette expérience nous a permis d'obtenir les courbes différentielles du solvant dont on a besoin pour déterminer et décrire la dépendance temporelle du saut de température du solvant pendant le cours des réactions chimiques étudiées. Ces résultats seront donc utilisés pour construire un modèle de réponse du solvant dans la dynamique de réactions des molécules de HgI_2 et $HgBr_2$.

Chapter 4

Preliminary experimental studies: determination of the structure of a solution and solvent response to impulsive heating

In the previous chapter we described the MD simulations as a computational tool to provide us structural information in liquids and their atomic correlations. We saw how MD can split the scattered X-ray signal into its principal atom-atom components. It was also shown how to extract the structure differentials that describe the changes in the diffracted intensities from a temperature rise during a chemical reaction. However numerous factors influence the accuracy of these simulations. First of all, theoretical potentials define trajectories on which molecules evolve; consequently the structure determination may depend on the type of potential used. Certain force fields are difficult to model efficiently: the most well-known example is the force field associated with hydrogen bonds. The simulations are run on a finite ensemble of molecules, which define the simulation box size, thus putting a constraint on the lowest Q and on the real space analysis. We can now ask if it is possible to obtain the structural information and the solvent response experimentally. As example of this, we are now going to show the results of a high-energy diffraction experiment on pure CCl_4 and Br_2 in CCl_4 which give us very useful information about the structure of the pure solvent and of the solution, with particular attention to bond distances and the cage. We will also present the measured solvent differentials for pure CH_3OH obtained by ultrafast impulsive heating of the liquid using Near Infrared (NIR) radiation.

4.1 Experimental structure determination in liquid solutions

The first step in a time resolved study is to measure the "static structure" of the solvent and the solution and this can be done by high-energy X-ray diffraction. I will now show some experimental curves obtained on beamline ID15 at the ESRF ($E_X = 88keV$) on pure CCl_4, data that determined the atom-atom correlation spectrum in the solvent and it can be seen as our reference X-ray structure for CCl_4.

4.1.1 Data collection and analysis of high energy static data on pure CCl_4

These studies were performed with very hard X-rays at 88keV, and allowed us to measure mono-atomic g(r), which weigh atoms-atoms pairs in proportion to Z_iZ_j. We can rewrite eq. 2.21:

$$S(Q) = f_e^2(Q) + f_e^2(Q) \int 4\pi r^2 \rho (g(r) - 1) \frac{sinQr}{Qr} dr \tag{4.1}$$

where ρ is the atomic number density and f_e is an average scattering factor per electron:

$$f_e = (\sum_{uc} f_m)/(\sum_{uc} Z_m) \tag{4.2}$$

where f_m is the elastic form-factor for atom m, uc is the chemical unit cell, and Z_m is the number of electrons in atom m.

Warren [38] derives an effective mono-atomic X-ray distribution through the sine-Fourier transform:

$$S[r] = 1 + \frac{1}{2\pi^2 \rho r} \int \frac{Q(S(Q) - f_e^2(Q))}{f_e^2(Q)} sinQr \exp(-\alpha Q^2) dQ. \tag{4.3}$$

$(S(Q) - f_e^2(Q))$ represents the deviation from atomic scattering from interference, and the integral is over the experimental Q-range. To attenuate parasitic oscillations from the finite Q range of the experiment, an exponential term with the damping factor, α is added. In static diffraction experiments, both elastic and inelastic signals are accumulated on the detector. To get the structure of liquid CCl_4, the diffracted signal $S(Q)$ is first scaled, in the high-Q limit, to the sum of the atomic gas scattering f_e^2 (see eq.4.2) and the Compton scattering for 1 C and 4 Cl atoms. Given that the Q dependence of the Compton scattering is structure independent, it is thus possible to correct for the inelastic scattering and get the elastic scattering $S_{solvent}(Q)$ over the entire Q-range and in this way calculate $S[r]$ as shown in eq.4.3. This unique high resolution experiment was done on beamline ID15 with X-rays at 88keV (0.141 Å). The high energy allowed to extend the Q-range to ~ 23Å^{-1} (Q$_{max}$=8.5-9.0Å^{-1} in time

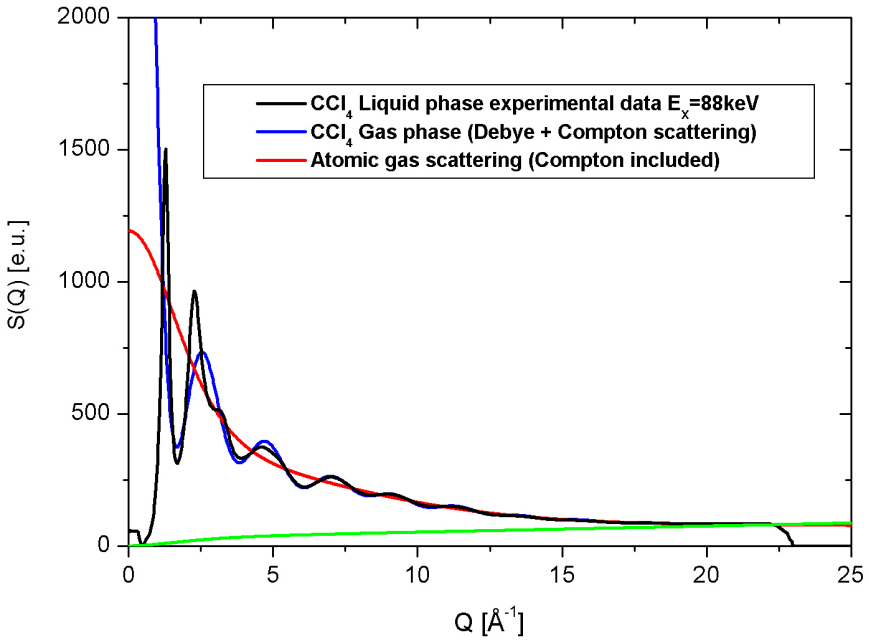

Figure 4.1: Static X-ray diffraction of pure CCl_4 solvent at 88keV: scaling of the diffraction signal of pure CCl_4, $S(Q)_{solvent}$ (black curve) to the average atomic gas scattering, f_e^2 (solid red curve). The blue curve shows the Debye scattering for molecular gas phase CCl_4, while the green curve is the calculated Compton scattering for $4Cl$+C.

resolved experiments), which greatly improves the spatial resolution. The CCl_4 solvent from Sigma Aldrich was contained in a 3mm quartz capillary. The scattered signal was recorded on a MAR345 Imaging Plate with 2300 × 2300 pixels with a pixel size of 150μm.

We show in figure 4.1 the diffraction signal from pure CCl_4 solvent, $S(Q)_{solvent}$, after appropriate scaling to the average gas scattering from an independent ensemble of atoms infinitely far from each other, f_e^2.

After subtracting f_e^2 of CCl_4 from $S(Q)_{solvent}$, the difference curve $S(Q)_{structure}$ was divided by the sharpening function and smooth function (Fig.4.2).

The resulting radial map is shown in Fig.4.3.

The molecular structure of CCl_4 is tetrahedral, with a carbon atom in the centre and 4 chlorine atoms 1.7670Å from the carbon.

In Fig.4.3 it is then possible to associate the first peak with the (four-fold degenerate) $C-Cl$ bond and the second one with the (six-fold degenerate) intramolecular $Cl-Cl$ distances 2.8855Å. The broad peaks at 3.8Åand 6.1Åare assigned to intermolecular $Cl..Cl$ distances between nearest neighbour CCl_4 pairs. These experimental distances can be immediately compared with the MD ones in Fig.3.6. The double liquid peak structure shows that liquid CCl_4 is a highly structured liquid with strong geometric order. The higher r values probes the correlation between atoms belonging to second and third coordination shells as shown in the enlarged section of Fig.4.3. Note

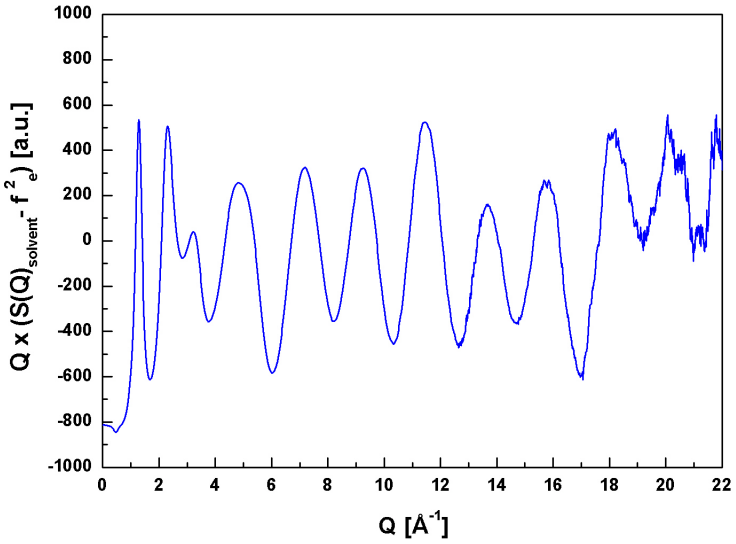

Figure 4.2: The Q dependence of the quantity $Q \times (S(Q)_{solvent} - f_e^2)$ which probes the structure of liquid CCl_4.

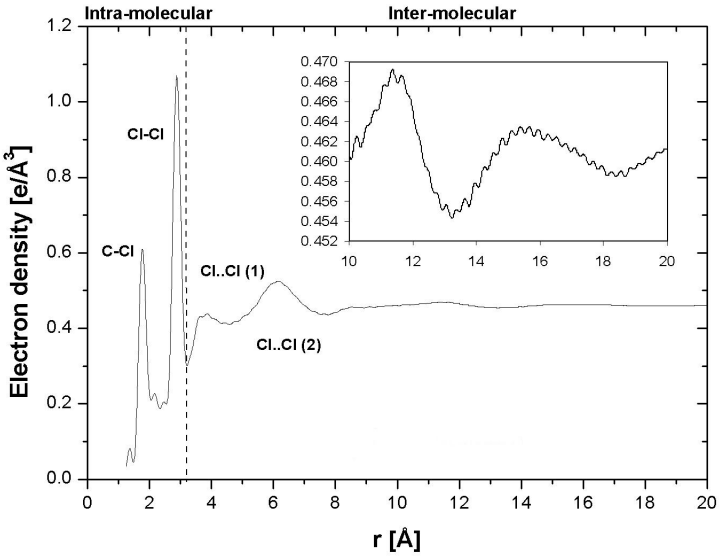

Figure 4.3: Radial map of CCl_4 from X-ray diffraction.

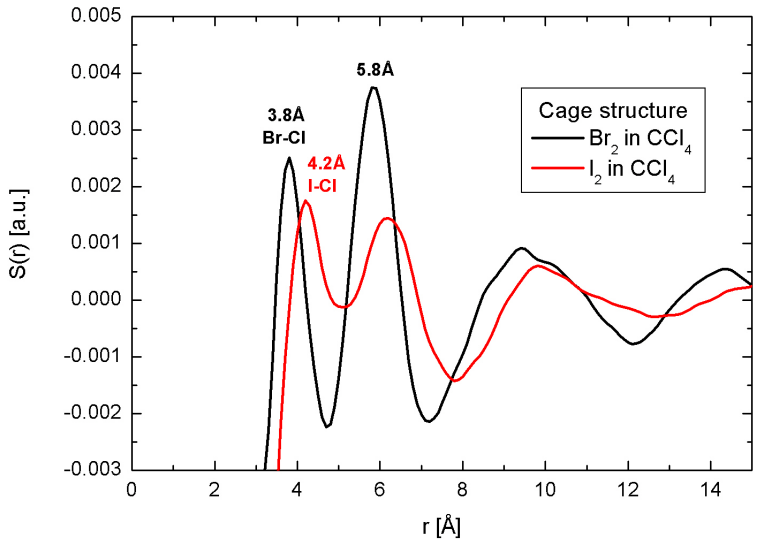

Figure 4.4: The measured cage structure of Br_2 in CCl_4 vs I_2 in CCl_4.

that non-resonant X-ray diffraction measures the weighted sum of all pair interactions and the results need interpretation. A similar experiment was also performed for Br_2 in CCl_4. In this case we can decompose the total scattering into

$$S(Q) = S_{Br-Br}(Q) + S_{Br-solvent}(Q) + S_{solvent-solvent}(Q). \tag{4.4}$$

The contribution from bromine is modelled by the Debye equation, using a fixed bondlength of 2.3Åfor the bromine in the ground state. In a set-up without energy discrimination, the contribution from inelastic scattering is subtracted using the parameters for atomic Compton scattering [41] as for the pure solvent. The quantity $S(Q)_{solvent-solvent}$ is the well-known scattering from the pure solvent and it normally dominates the other contributions at the normal concentrations used (for example 1:80 for the Br_2/CCl_4 solution in the time resolved experiment). The term $S(Q)_{Br-solvent}$ is the "cage" term. In order to extract the cage term, the bromine gas scattering is subtracted from the result and the data is finally normalised by the atomic scattering functions of bromine and the second partner. In Fig.4.4 we can see the measured cage for Br_2 in CCl_4 extract from the high-energy X-ray diffraction experiment (70mM solution). This result is compared with the measured cage for I_2 in CCl_4 (45mM solution, E_x=17keV) obtained by Anton Plech. In the MD simulations we saw how solvent is (effectively) closer to a Br atom than to a Br_2 molecule. In Fig.3.4) we observe the same trend: the cage radius is smaller for Br_2 than in I_2 due to smaller Br atoms. What may be a problem in using this data to determine experimental bondlengths in solution is that the experimental accessible $S[r]$ function, is a weighted sum of $Br-Cl$ and $Br-C$ correlations. This means that comparisons between experiment and theory (DFT/MD) in solution phase X-ray diffraction experiments have to be done at

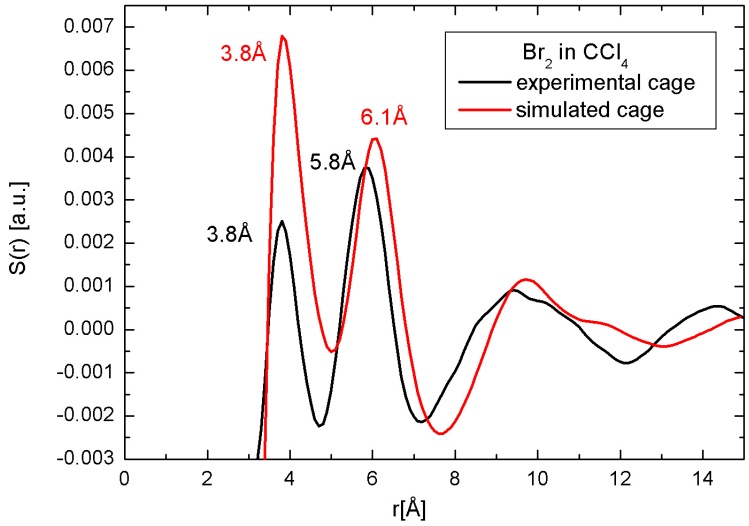

Figure 4.5: Comparison between the MD simulated and experimentally measured cage for Br_2 in CCl_4.

the $S(r)$ level, i.e. including the effect of atomic form factors. In Fig.4.4 we show the comparison between the measured and the simulated cage structure for Br_2 in CCl_4 in real space. The simulated curve is obtained as the back-Fourier transform of the cage structure in Q-space showed in Fig.3.3.

In the two curves we observe the same positions for the first peak, which reassures us on the cage radius. The two curves are nevertheless quite different. We are well aware of the limits of MD simulations: the theoretical potentials define the trajectories on which the molecules evolve; consequently the liquid structure determination depends on the type of potential used. Certain force fields are difficult to model efficiently: the most well-known example is the force field associated with hydrogen bonds. The simulations are run on a finite ensemble of molecules, which define the simulation box size, thus putting a constraint on the lowest Q and on the real space analysis. We already anticipate here the non-perfect agreement between the simulated and measured cage term which is probably one of the reasons for imperfect agreement between the theory and experiments in the time resolved regime for Br_2 in CCl_4 (see later).

4.2 Experimental determination of the solvent response: the impulsive heating of CH_3OH with NIR laser pulses

In this section we will show how it is possible to directly measure the solvent response of a simple liquid to a transient temperature rise, showing the results for pure methanol.

4.2. Experimental determination of the solvent response: the impulsive heating of CH_3OH with NIR laser pulses

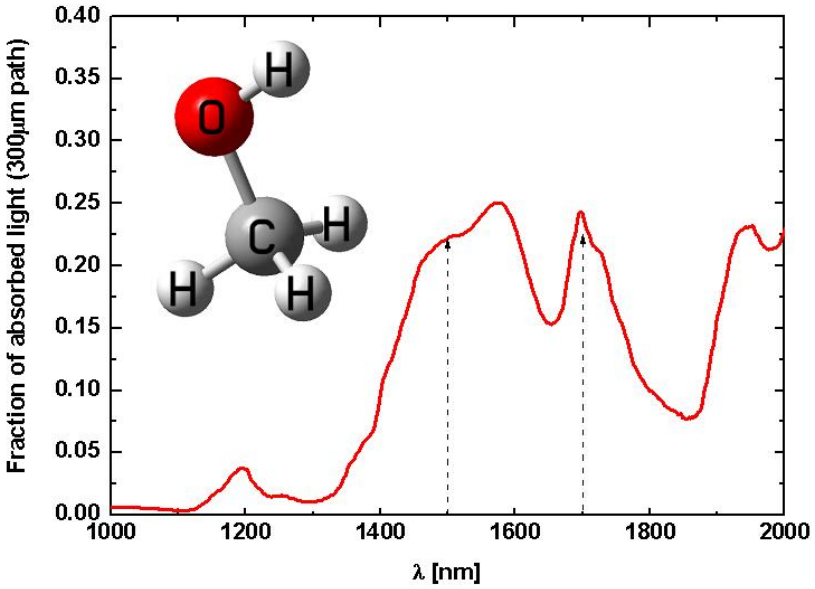

Figure 4.6: The CH_3OH molecule structure and the fraction of absorbed light vs wavelength measured with a JASCO V-570 spectrometer. NIR pulses (1500-1700nm) excite overtones of OH and CH_3 vibrations in liquid methanol.

We saw in the previous chapter (section 3.2) how the decomposition of the scattered X-ray signal has so far been aided by MD simulations. We also underlined the numerous factors which influence the accuracy of these simulations. For these reasons it is desirable, whenever possible, to measure the solvent differentials directly. Clearly in these experiments the polychromatic correction is also already included, as well as the contributions for the response of the detector, allowing us a more direct view of solute and cage dynamics.

We will show a comparison between the experimental solvent terms with those from MD simulations. It has been demonstrated [64] that the use of experimentally determined solvent differentials greatly improved the quality of global fits when applied to the time resolved data for $C_2H_4I_2$ dissolved in methanol [9]. In the next chapter will then apply these experimental differentials in the analysis of HgI_2 and $HgBr_2$ dissolved in methanol.

The key idea of this experiment is that near-IR pulses (1500-1700nm) excite overtones of OH and CH_3 vibrations in methanol, and in doing so, they inject energy into the liquid bulk in a non-destructive way, i.e. without inducing any chemical change. In Fig.4.6 we show the structure of the methanol molecule together with its absorption spectrum measured with a JASCO V-570 spectrometer. We can observe the two absorption bands in the IR spectrum at 1500nm and 1700nm, which following [66], can be assigned respectively to the first overtone of the $O-H$ stretch (whose fundamental is at 3337cm^{-1}) and to the first overtone of the CH_3 asymmetrical stretch mode (whose fundamental is at 2934cm^{-1}) .

The ensuing hydrodynamics, induced by the transfer of heat from a subset of excited CH_3OH^* to the bulk and the subsequent thermal expansion, were probed in the experiment by 100ps X-ray pulses from the synchrotron. We will explain how the time-resolved data allowed us, first of all, to extract two key differentials: the change in the solvent diffraction from a temperature change at constant density, seen at a very short time delay ($\sim$ 100ps), and a term from a change in density at constant temperature. The latter term becomes relevant at later times ($\sim 1\mu$s) when the bulk of liquid expands to accommodate its new temperature at ambient pressure. These two terms are the principal building blocks in the hydrodynamic equation of state, and they are needed in a self-consistent reconstruction of the solvent response during a chemical reaction. In particular we can roughly estimate in a very simple way the temperature rise induced through NIR impulsive heating, observing that is comparable with the temperature rise induced by the solute relaxations during a chemical reaction. The temperature rise induced in liquid methanol through laser excitation can indeed be estimated as

$$\Delta T = \frac{\epsilon_{Abs}}{\rho \quad t \quad C_V},$$

In the formula ρ, the density of methanol at room temperature is equal to $\rho = 791kg/m^3$, $C_V = 2151J/(Kkg)$ is the heat capacity of methanol at constant volume and $t = 0.0003m$ is the thickness of the sample. ϵ_{Abs} is the fraction of the (average) energy density of the incident pulse absorbed by the liquid in the X-ray volume. Looking at Fig.4.6 this fraction is $\sim$1/4 of the incident energy density, which in this experiment was chosen, in the way we will discuss immediately, to be $250 \times 10^4 mJ/m^2$, giving $\epsilon_{AbsEnergy} \simeq 62.5 \times 10^4 mJ/m^2$. With the given values we estimate $\Delta T \sim 1.2K$, comparable with the temperature rise of the solvent observed during a chemical reaction [1, 9].

4.2.1 Experimental details

The tunable femtosecond laser (2.3.3) was used to generate 100fs NIR radiation in the following way: the 800nm output from the Hurricane was used to seed the TOPAS in which it was down converted into two NIR pulses, the 1500nm (signal) and the 1700nm (idler). The pulse duration is estimated to be 100fs. As preliminary measurement we performed a titration for the laser power: the difference signal (laser on - laser off) was measured at 150ns and at 1μs as function of the laser power. The results are shown in Fig.4.7. The data were scaled by the energy density of the incident pulse. It is clear that above $250mJ/cm^2$ the behaviour is non linear indicating the onset of multi-photon absorption processes. The beam profile was measured using a 25μm pinhole coupled through a 1mm optical fiber to a 1ns detector for NIR radiation (Thorlabs DET-410); the signal was measured with a digital oscilloscope. The result is shown in Fig.4.8. The beam size is calculated using the $1/e^2$ point and was found to be $\sim 5.3 \times 10^{-4} cm^2$. With the given energy density per pulse, the measured beam size, and the 1kHz laser repetition rate, we estimate to have at the sample a total incident power of $\sim 130mW$.

Polychromatic 100ps X-ray pulses with 5×10^9 photons/pulse were delivered by the U17 in-vacuum undulator (2.3.2). The X-ray spectrum was peaked at $E_f = 18.2$keV

4.2. Experimental determination of the solvent response: the impulsive heating of CH_3OH with NIR laser pulses

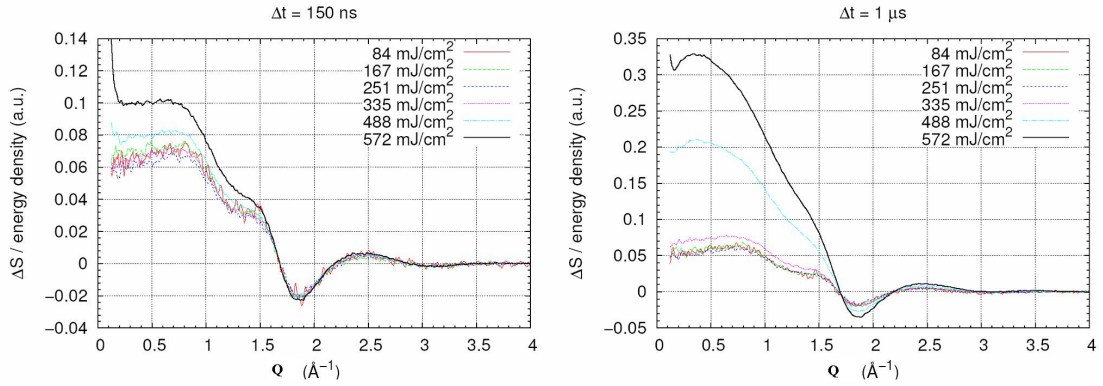

Figure 4.7: Summary of the power titration measurements. On the left panel we show the 150ns time delay and on the right the 1μs curves. The number in the the legend gives the incident energy density.

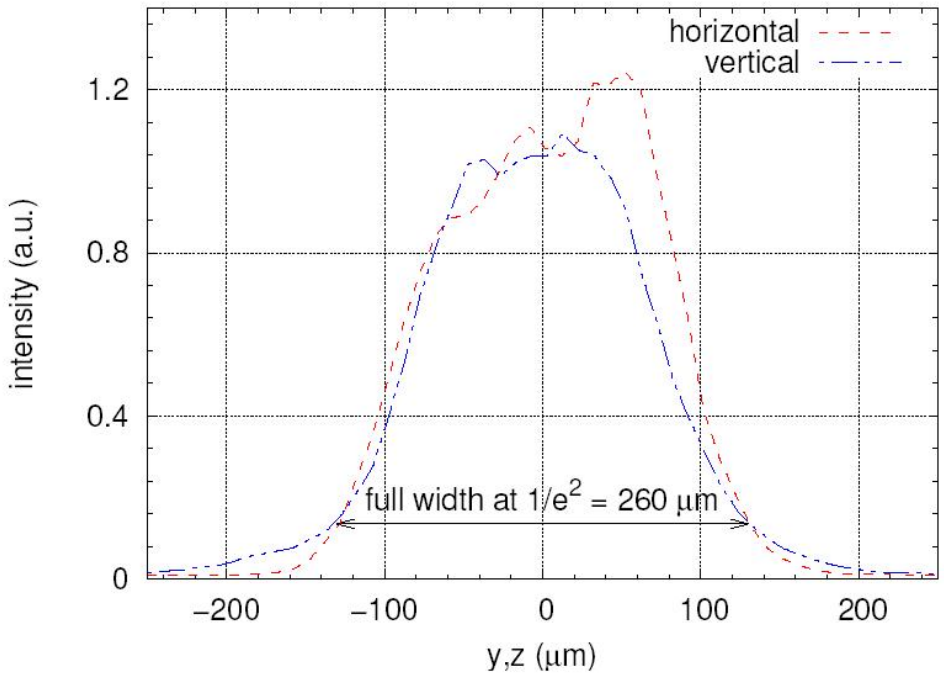

Figure 4.8: The measured laser beam profile.

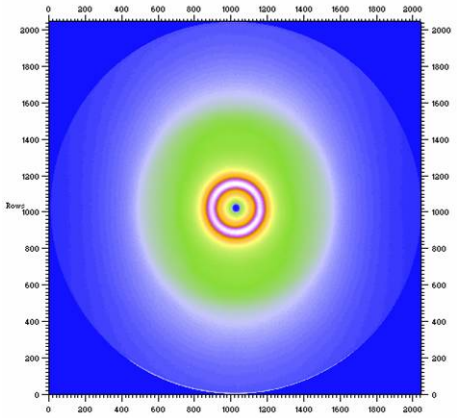

Figure 4.9: The 2D diffraction pattern from pure methanol from the MarCCD detector.

and had a bandwidth of 0.45keV (2.5% bw). The high-speed chopper was used to select single X-ray pulses in the 16-bunch mode, where the pulses are separated by 176ns. The X-ray beam was focused by a toroidal mirror to a spot size of $0.1 \times 0.05 mm^2$ at the sample. The scattered signal was recordered on the MarCCD detector at well defined time delays relative to the excitation pulse. In fig.4.9 we show the 2D diffraction pattern from pure methanol. The elliptical contour at high angles is due to horizontal polarisation of the X-rays (section 2.1.1).

The two different sample cells were used, the capillary based system and the open-jet (section 2.4). The sample was purchased from Merck and used without further purification. The data were collected by exposing the CCD for 12s and, given the 1kHz repetition rate of the laser/X-ray beam, the camera received 12000 incoming X-ray pulses per image. The pixels in a single image received between 3500 and 25000 photons. The images were collected in pairs, with and without laser, for all time delays. This data collection cycle was repeated 100 times, which typically took 4.5 hours.

4.2.2 Data reduction

The 2-dimensional diffraction patterns collected with the CCD detector were first of all radially integrated to obtain 1-dimensional radial intensity curves using the software FIT-2D [67]. It calculates the radial intensity, averaged over the azimuthal angle around the incoming beam, as a function of the scattering angle (2θ) from the beam centre [67]. In this process the pixel counts are corrected geometrically to render the flat detector spherical, the intensity reduction from the linear polarisation is scaled to 1 and the data are finally corrected for the absorption in the liquid sheet and in the phosphor (section2.1). Note that this radial intensity curve $S(2\theta)$ should be independent of the synchrotron current since the exposure time was scaled to the inverse synchrotron current to keep the intensity on the CCD constant for hours of the data collection. That reduces the effect of non linearity in the CCD. As we already show in the example of Br_2 in CCl_4 (Fig.2.6), the relative change in the scattered intensity between the ground and the excited state is very small (10^{-4} to 10^{-2}), Fig.4.10). Consequently, it is not possible to simply take the difference of the 2 images (laser on-laser off) but

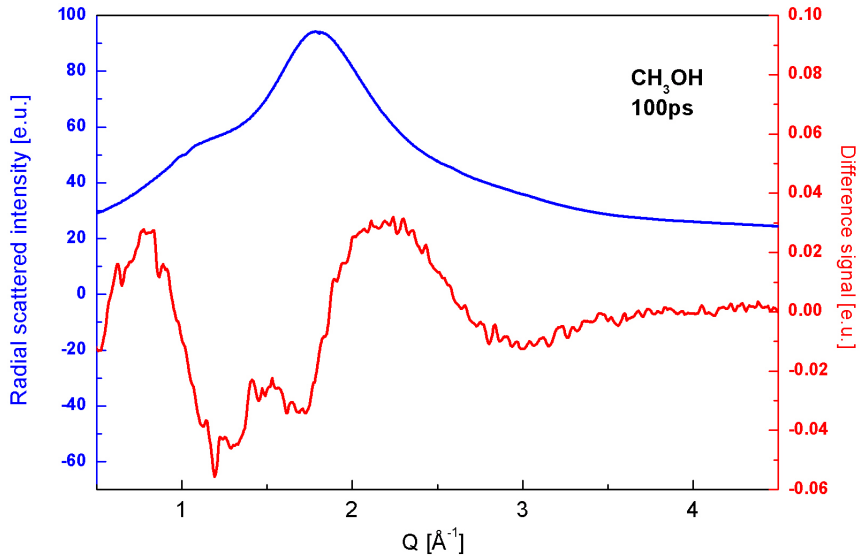

Figure 4.10: Radial scattering intensities of liquid methanol. The curve before and 100ps after NIR excitation look exactly the same. On the right scale we show the very weak signal induced by ultrafast heating, $\Delta S/S = 0.1\%$.

the raw data has to be scaled before subtraction. The reason for this is due to very small changes in the X-ray beam position during the data collection that causes small variations in the incident current I_0 after the sample slits. For this reason we have chosen to use the CCD image itself as I_0 monitor by scaling the radial intensity at 1 at the edge of the detector (high Q-limit) where the scattering can be approximated as atomic gas scattering, which is independent of chemical changes in the sample. In this way the data is scaled to a constant number of atoms which is important during the expansion phase of the sample. Indeed, the fast transfer of heat from the excited molecules to the bulk forces the solution to expand. The expansion takes place on a time scale determined by the time it takes sound waves to traverse the laser illuminated volume. In fast reactions and with current beam sizes ($\sim 100\mu m$) the expansion takes place 10 to 100ns [20]. This means that the number of molecules is generally different in laser-off and laser-on images. Given that the high-Q scattering between 8-9Å^{-1} may still have a molecular component, the best scaling approach would be to identify an isobestic point, i.e. a Q-point where the sum of all the structural changes does not change. The first iteration in finding a high-Q isobestic point is to consider the possible reaction channels including their hydrodynamics response and then check that the difference data are independent of small shifts in Q around this initial guess. Note finally that the scale factor has to be known to a relative precision that is much better than the relative changes in $\Delta S(Q,\tau)$. Hence to improve the counting statistics, a narrow interval in Q with a width of ~ 0.5 Å^{-1} was used in the normalisation. So with this approach an I_0 monitor is not needed because the image itself is used to obtain the scale factor. This self-scaling approach ensures that the data are independent of small variations in the beam position. Before obtaining the 100ps and 1μs difference

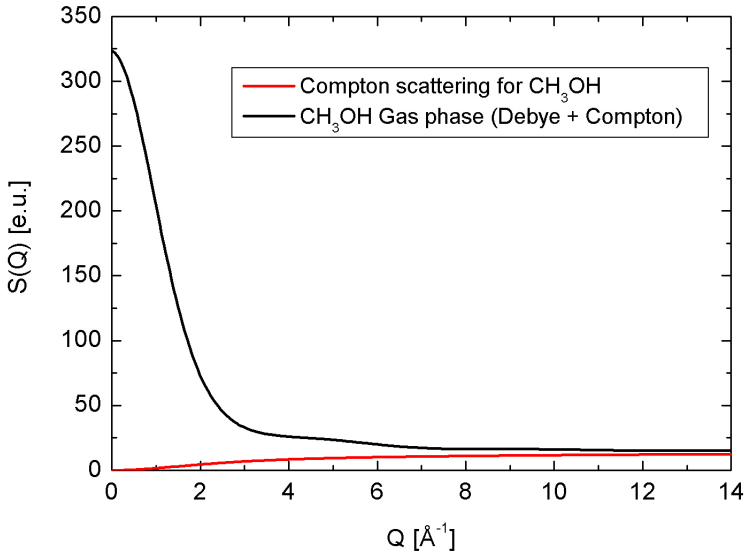

Figure 4.11: Theoretical Debye and Compton scattering intensities for pure CH_3OH.

curves showed in Fig.4.12, once the normalisation is done, the data was normalised to electron units by scaling the spectra to the curve given by the molecular gas scattering from a single solvent molecule (Fig.4.11).

We obtain in this way, scaled data in absolute units. The advantage of having the data in absolute units is that this allows to determine the percentage of excited solute molecules in the solution, and hence check the efficiency of the laser excitation.

In our experiment we were forced to use a polychromatic X-ray beam rather than the monochromatic beam due to a 550-fold gain in intensity. As a consequence the scattered intensity at a given solid angle is a sum of scattered intensities from a range of scattering vectors in the 3% bandwidth. In order to compare the data to the theoretical curves we need to take into account this polychromaticity and convolute the theoretical results with the intensity distribution of the measured spectrum of the U17 undulator.

After having applied this reduction, normalisation and scaling procedure, we obtain the transient heating curves for methanol for 100ps and 1μs shown in Fig.4.12. Averaging 10-100 difference maps per time delay gives a good estimate of the error bars for every Q, using the standard deviation from the mean value. Thus the error bars obtained account only for statistical noise and not systematic errors.

4.2.3 Interpretation: solvent response

In Fig.4.13 we present a simply physical picture of the ultrafast heating of a simple liquid. A 100fs NIR pulse is partially absorbed by the liquid. In red we indicate the molecule that have absorbed a photon: the system appears initially as a web of "hot points". The excited molecules will then release their energy through collisions and reach a locally uniform equilibrium state. The estimation of this equilibration time

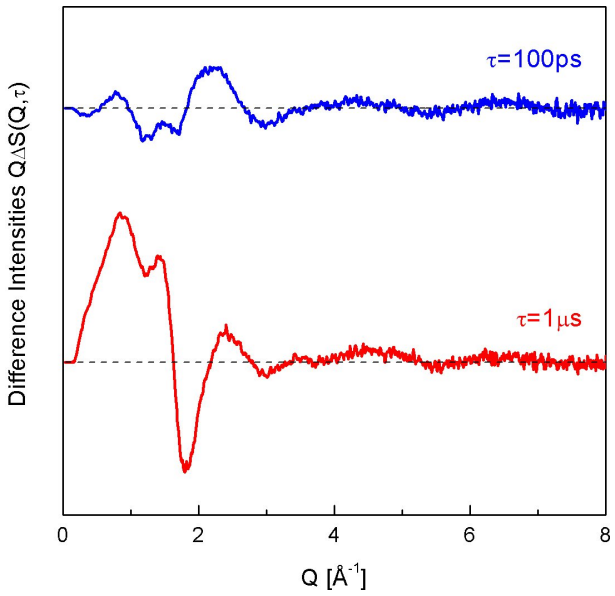

Figure 4.12: Transient heating curves for methanol for 100ps and 1μs.

is non trivial. We can use an argument based on the average distance between two excited molecules and estimate the time needed for a thermal wave to travel to half the average separation. This equilibration time is solvent dependent, and with the typical excitation levels in these studies, 1-10mM, the solvent is thermalised in 20-80ps, see below.

After this time it is meaningful to consider the solvent in local thermal equilibrium and described by three thermodynamical variables: temperature, density and pressure, T, ρ, P, linked by the equation of state. The latter allows us to consider only two free variable, for example T and ρ. The scattered intensity can hence be expressed as a function of these two variables and the induced change $\Delta S(Q,\tau)$ can be written as

$$\Delta S(t) = \left(\frac{\partial S}{\partial T}\right)_\rho \Delta T(t) + \left(\frac{\partial S}{\partial \rho}\right)_T \Delta\rho(t). \tag{4.5}$$

In doing so, the temporal evolution of the solvent response is described as a linear combination of two differentials with time dependent coefficients. It can be shown by solving the hydrodynamics equations [65] that for sufficiently short time delays $t < \tau_L = L/c$, where τ_L is the so-called Longaker-Litvak time, L is the laser beam size and c the speed of sound in the liquid, the solvent is heated at constant volume. In this CH_3OH NIR impulsive heating experiment $c = 1143m/s$ and $L \sim 50\mu m$, which gives $\tau_L \sim 44ns$. At later times, 10-100ns, the pressure relaxes, which drives the expansion of the solvent. After fast vibrational cooling of the excited methanol molecules, well below 10ps, the response of the solvent is entirely hydrodynamic. Therefore, it is relatively easy to determine the derivatives in eq.4.5, by measuring the response at two time delays. For this reason we collected, with greatly enhanced statistics, diffraction patters at 100ps and 1μs. The 100ps data are essentially $\left(\frac{\partial S}{\partial T}\right)_\rho$ multiplied by the temperature rise at

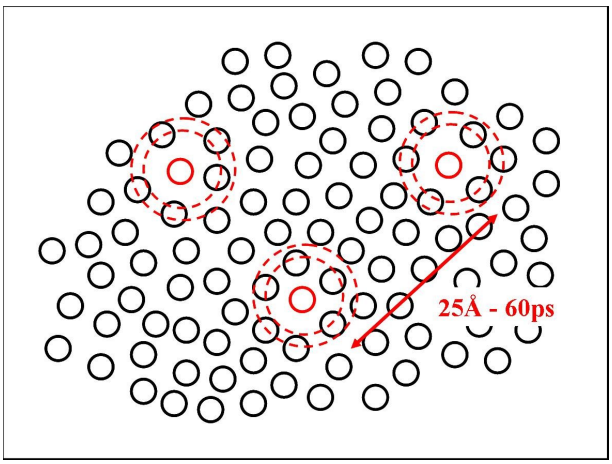

Figure 4.13: Physical picture of ultrafast heating in methanol. A 100fs NIR laser pulse is (partially) absorbed by the liquid. The red molecules have absorbed a photon and they release their excess energy to the surrounding liquid through collisions. The dashed lines represent the thermal wave moving through the liquid. After $\sim$ 60ps the "waves" have, on average, travelled to the midpoint between the two excitation centres.

this early stage of heating at constant volume, hence the second term contributing net zero, $\Delta S(100ps) = \left(\frac{\partial S}{\partial T}\right)_\rho \Delta T(100ps)$. At 1μs, when the ambient pressure is restored, the experimental signal gives the equilibrium response of the liquid $\left(\frac{\partial S}{\partial \rho}\right)_P$. A proof for this assumption can be immediately seen from the comparison between the 1μs signal and the difference signal obtained subtracting two static diffraction patterns of pure methanol collected at two different temperature at constant ambient pressure (the details of this measurements will be discuss later)(Fig.4.14).

Note the very good agreement in the shape of the curves. Moreover the scaling of the normalised static derivative on the 1μs signal allows us to determine the temperature rise ΔT, which is estimated to be $\sim 1.5K$, a value in fair agreement with the rough estimate in 4.2.

With a temperature change of $\Delta T = 1.5K$ we can estimate the concentration of excited methanol molecules. The energy absorbed is

$$E_{abs} = m_{CH_3OH} C_V \Delta T = \rho_{CH_3OH} V C_V \Delta T,$$

which means that the number of excited methanol molecules is

$$N_{abs} = \frac{\rho_{CH_3OH} V C_V \Delta T}{\hbar\omega} = \frac{\rho_{CH_3OH} V C_V \Delta T \lambda}{hc},$$

giving a density of absorbers

$$\rho_{abs} = \frac{\rho_{CH_3OH} C_V \Delta T \lambda}{hc},$$

which with $C_V = 2151 J/(Kkg)$, $\rho_{CH3OH} = 791 kg/m^3$ and $\lambda = 1700nm$ gives

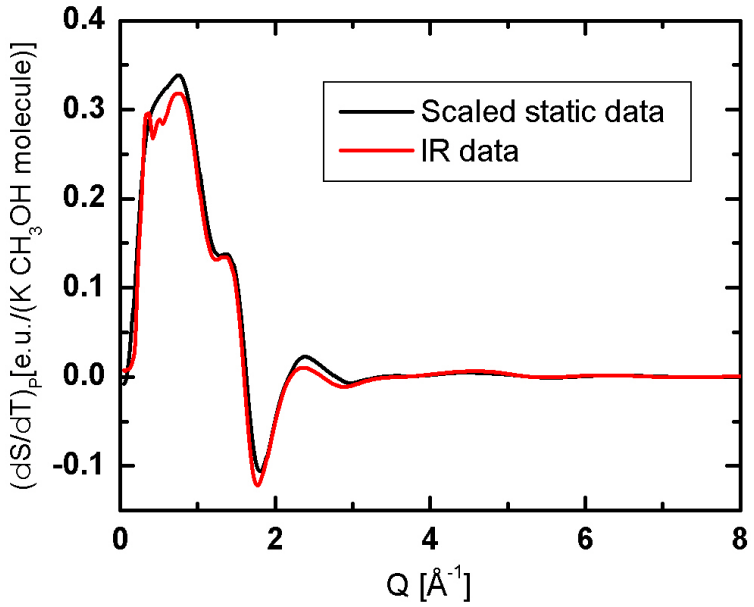

Figure 4.14: Comparison between 1μs time delay and static isobaric temperature difference data.

the density of excited molecule to $22 \times 10^{24} molecules/m^3$. The molar concentration of excited molecules is then found by dividing the number density per liter with Avogadro's number $N_A = 6.023 \times 10^{23}$ which gives 36.5mM.

As the concentration of pure methanol at ambient conditions is 24.70M, this corresponds to exciting 1 out of 677 molecules. From this concentration, if the volume per excited solute is approximated by a sphere, the distance between nearest neighbours is 44Å.

The validity of classical hydrodynamics assumes a homogeneous and isotropic sample. It is thus important to estimate the time it takes to smooth out the memory of time zero, which can be described as a collection of hot points in the liquid. Following the classical thermal diffusion theory developed by Landau and Lifshitz, a hot point in a liquid cools down in time and space following the equation

$$T(r,\tau) \propto \frac{1}{8(\pi\chi t)} exp(-r^2/(4\chi t)), \tag{4.6}$$

with $\chi = \frac{\kappa}{\rho C_V}$. Here χ is the thermometric conductivity and κ the thermal conductivity. The parameters for methanol are $\rho = 791 kg/m^3$, $C_V = 2151 J/K/kg$, $\kappa = 0.21 J/s/m/K$ and $\chi = 1.2345 \times 10^{-7} m^2/s$. The 50% point in space moves as

$$r_{50\%}(t) = 2ln2\sqrt{\chi t}.$$

From this equation we can estimate the time it takes, on average, for two neighbouring spherical thermal waves to meet, the criterion for local thermal homogeneity, which

gives ≃80ps. As the scattering data presented here are ensemble averaged by the 100ps X-ray, it is justified to use classical hydrodynamics in this work.

We still need to determine the two differentials $(\partial S(Q)/\partial T)_\rho$) and $(\partial S(Q)/\partial \rho)_T$) to describe the heat induced change in the solvent scattering as a function of the time. For the above considerations the 100ps NIR signal give us the isochoric heating differential $\left(\frac{\partial S}{\partial T}\right)_\rho$ multiplied by the temperature rise $\Delta S(100ps) = \left(\frac{\partial S}{\partial T}\right)_\rho \Delta T(100ps)$. The second derivative $(\partial S(Q)/\partial \rho)_T$) will now be calculated. Indeed, at 1μs the liquid returns to ambient pressure. Therefore the 1μs data equals $\left(\frac{\partial S}{\partial T}\right)_P$ multiplied by the temperature rise at 1μs. The differential $\left(\frac{\partial S}{\partial T}\right)_P$ can be determined experimentally from a series of static diffraction measurements at ambient pressure and different temperatures, or simulated by MD. By scaling the 1μs impulse data to the $\left(\frac{\partial S}{\partial T}\right)_P$ curve from the static measurements, we get the temperature rise $\Delta T(1\mu s)$. At this temperature the solvent is still hot, yet the temperature has lowered from the temperature at 100ps by the ratio C_V/C_P due to expansion. The experimental differentials are showed in Fig.4.15. Summarising:

$$\Delta S(t) = \left(\frac{\partial S}{\partial T}\right)_\rho \Delta T(t) + \left(\frac{\partial S}{\partial \rho}\right)_T \Delta \rho(t);$$

$$\Delta S(100ps) = \left(\frac{\partial S}{\partial T}\right)_\rho \Delta T(100ps),$$

$$\begin{aligned}\Delta S(1\mu s) &= \left(\frac{\partial S}{\partial T}\right)_\rho \Delta T(1\mu s) + \left(\frac{\partial S}{\partial \rho}\right)_T \Delta \rho(1\mu s) = \\ &= \left(\frac{\partial S}{\partial T}\right)_\rho \frac{C_V}{C_P} \Delta T(100ps) + \left(\frac{\partial S}{\partial \rho}\right)_T \Delta \rho(1\mu s) = \\ &= \Delta S(100ps)\frac{C_V}{C_P} + \left(\frac{\partial S}{\partial \rho}\right)_T \Delta \rho(1\mu s),\end{aligned} \tag{4.7}$$

which gives

$$\left(\frac{\partial S}{\partial \rho}\right)_T \Delta \rho(1\mu s) = \Delta S(1\mu s) - \frac{C_V}{C_P}\Delta S(100ps).$$

$\Delta\rho$ at $1\mu s$ can be calculated from the linear expansion relation, with $\alpha_p = -1.49 \times 10^{-3}\mathrm{K}^{-1}$

$$\Delta \rho(t) \simeq -\rho_0 \alpha_p \Delta T(t),$$

for time after the thermal expansion ($t > 300ns$) [65, 57].

We can now compare the MD simulated and the experimental differentials, observing a quite big discrepancy at low Q.

These experimental solvent differentials were first used to account for the solvent response to heating induced during the relaxation of photo-excited $C_2H_4I_2$ in methanol [64]. These fits were first done with the MD simulated differentials [9]: in Fig.4.17 we show the comparison of the two analysis and the striking improvements brought from

4.2. Experimental determination of the solvent response: the impulsive heating of CH_3OH with NIR laser pulses

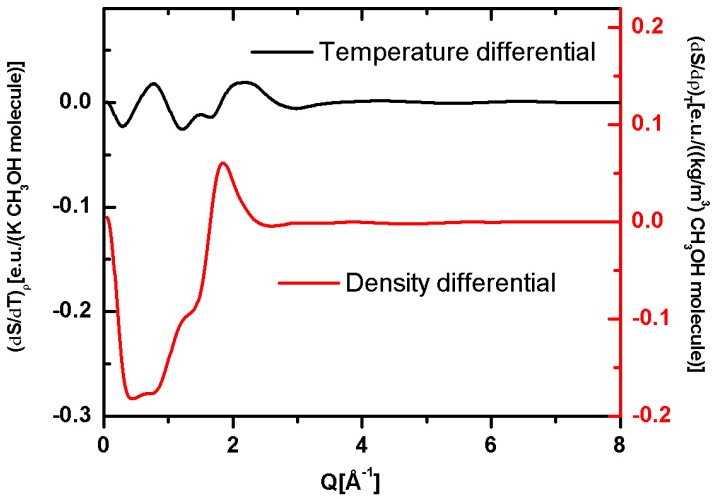

Figure 4.15: The impulsive solvent differentials $(\partial S/\partial T)_\rho$ (black) and $(\partial S/\partial \rho)_T$ (red) for methanol obtained from NIR experiment.

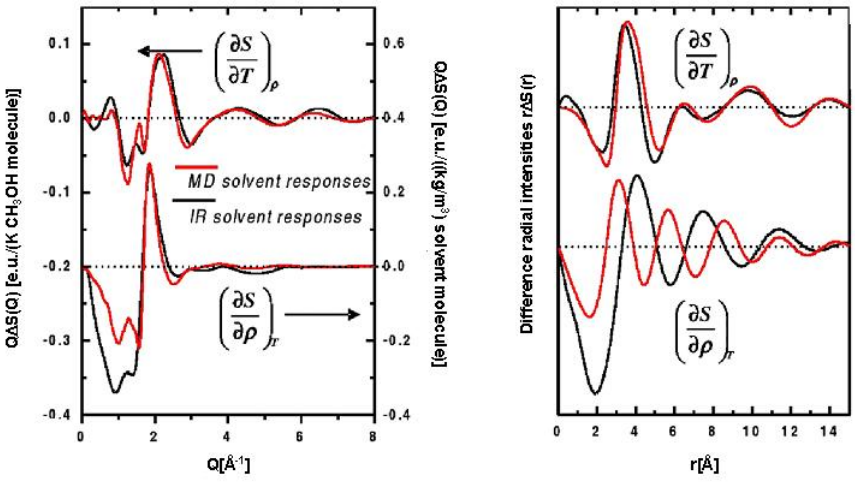

Figure 4.16: Experimental difference intensities vs MD differentials in Q and real space.

the experimental terms, in particular at low Q at time delays after 30ns. The total χ^2 of the least-squares fit is reduced by 30% when MD solvent terms are replaced by the experimental ones.

We are now armed with experimental solvent differentials that will allow us to account for the CH_3OH response to heating induced by the relaxation of HgI_2 and $HgBr_2$, as we will see in the next chapter.

4.2.4 The static solvent differential $\left(\frac{\partial S}{\partial T}\right)_P$ for methanol

As we saw in the previous section it is necessary to know $(\partial S/\partial T)_P$ for the absolute scaling of the impulsive differentials from the NIR. This term can be either simulated by MD, as we did (3.2) for CCl_4, or measured experimentally. We obtained this differential from a series of separate static diffraction measurements on pure methanol at the same (ambient) pressure, but at different temperatures. A monochromatic X-ray beam at 26keV was sent through liquid methanol contained in a temperature adjustable sample cell designed for temperature control by the Sample Environment Group at the ESRF. Diffraction patterns were taken at four different temperatures: 15.0, 17.5, 20.0, 22.5 °C. We can see in the following figures some pictures of the sample cell. The sample is contained in a $300\mu m$ thickness quartz capillary which is inserted in an aluminium block. Temperature control on the sample relied on two Peltier devices. A water-chiller was used to cool down the two Peltier. A thermocouple placed within the sample chamber monitored the temperature, with a precision of 0.01°C. Between the aluminium chamber and the holder of the sample cell a 10mm nylon spacer was inserted to avoid heat dispersion. The entrance and exit windows were made of 0.75μm thick kapton foil. The data were corrected for angular dependent absorption in the phosphor screen and normalised at high Q. We obtained the differences signals (averaging over 20-30 images per temperature), by subtracting the radial diffraction patterns and then normalising at 1K. The curves are shown in Fig.4.19. Note the linearity and that the curves are similar in shape to the impulsive one shown in Fig.4.12, except for a small damping in amplitude for the asymmetric 2.5% bw pink beam used in the 1μs curve.

4.3 Conclusions

We have shown the static high-energy diffraction data for CCl_4 and Br_2 in CCl_4, from which a very precise structure determination of the pure solvent and solution was achieved. We then focused our attention on the cage, the solvent-solute correlation terms and compared them with MD simulations. The information obtained will drive the analysis of the time resolved structure of Br_2 in CCl_4 which will be discussed in the next chapter.

The study of the impulsive heating of pure methanol was also presented. We only showed the data at 100ps and 1μs, but showed how they can be used to transformed into generic solvent differentials needed to determine the time dependence of the temperature rise during a chemical reaction. We showed the improvements in the fits using

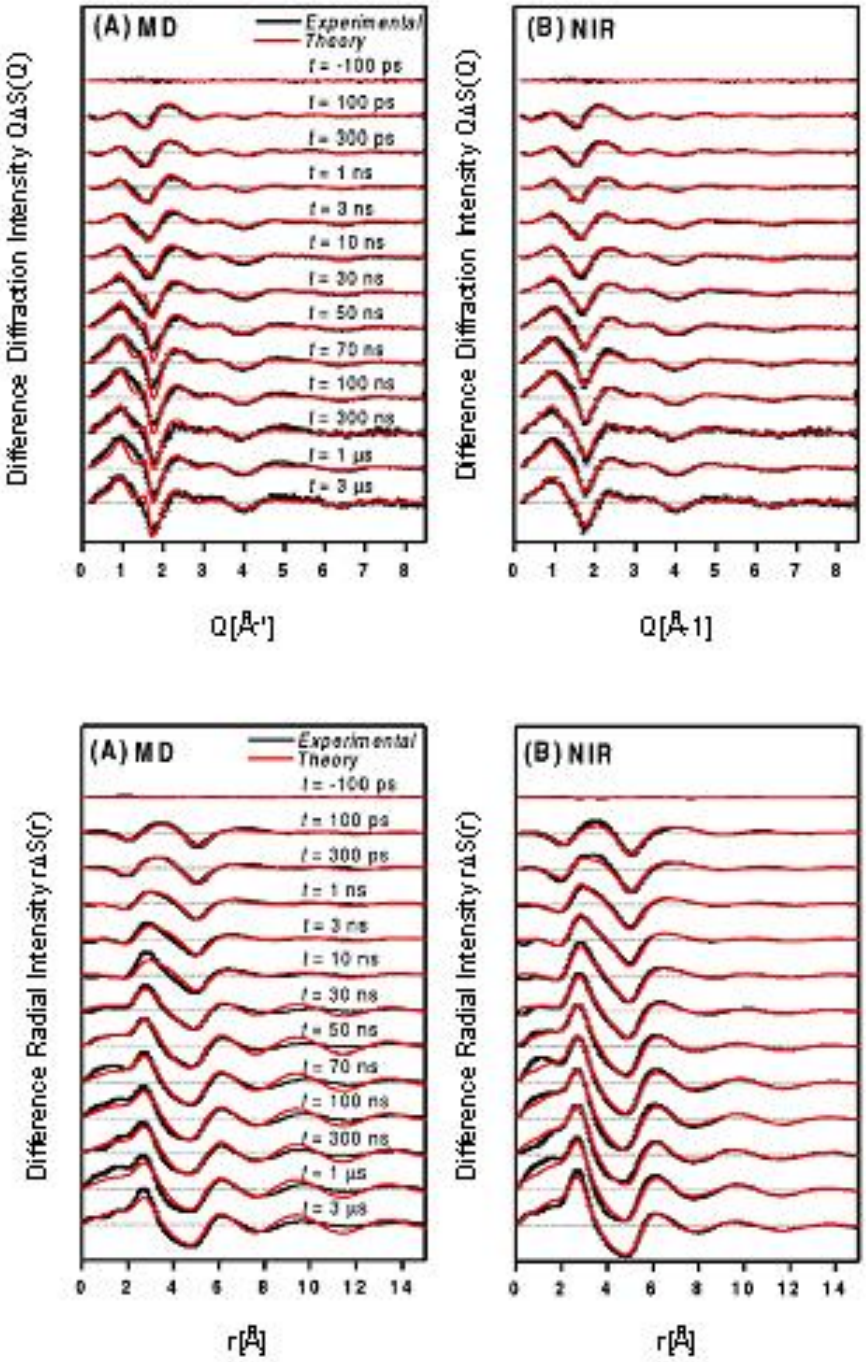

Figure 4.17: Time-resolved diffraction signal as a function of time delay for $C_2H_4I_2$ in methanol [9]. The upper panel shows the global fit with all the reaction components. Theory curves are red, experimental ones black. To the left, the solvent components were taken from MD, while on the right, the solvent components are experimental. The improvement is clear especially at low Q and for data after 30 ns. In the low panel the same comparison is shown in real space.

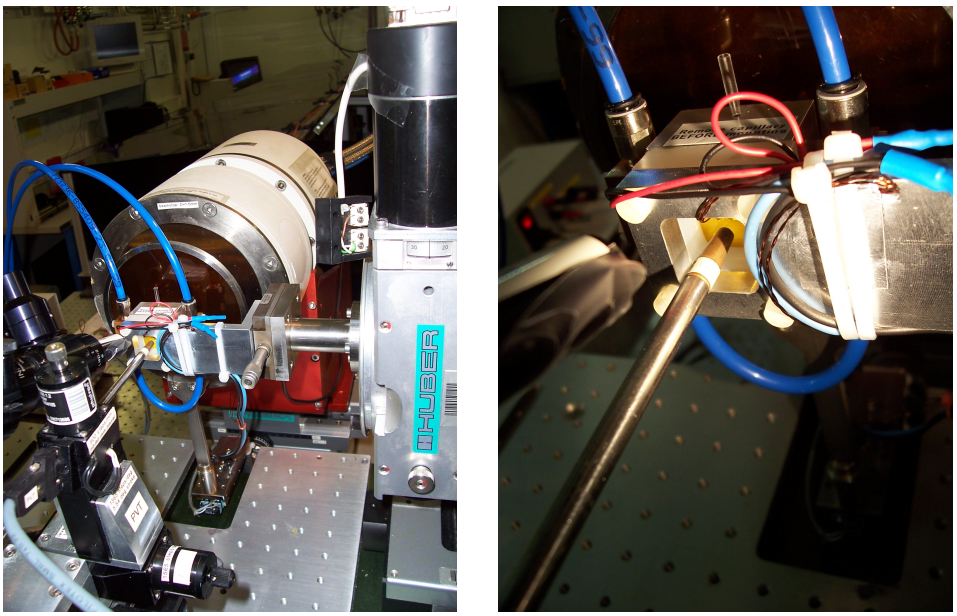

Figure 4.18: Views of the temperature controlled sample cell.

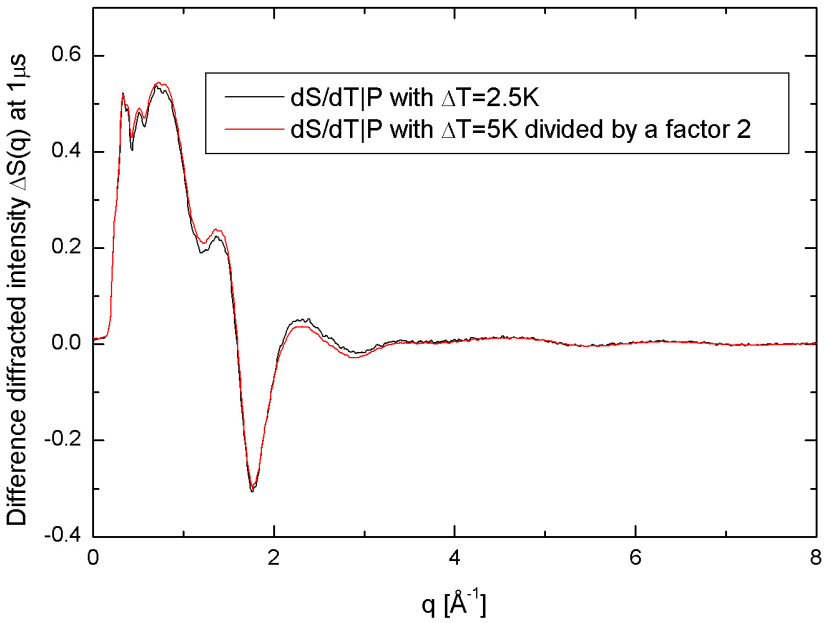

Figure 4.19: The static $(\partial S/\partial T)_P$ differential determined from temperature scans with monochromatic beam at 26keV.

the experimental differentials as compared to MD [9, 64]. These experimental measurements gives us a more direct comparison with time resolved data. Consequently, in the next chapter these experimental differentials will be used to account for the solvent response during the recombination process of photodissociated HgI_2 and $HgBr_2$ in methanol. We will also show an extremely recent experiment on solvent response of pure CCl_4 which was measured by the ID09B team while I was writing this thesis. For this solvent, we could not use NIR radiation, but the heating was induced through two-photon absorption using 400nm radiation. The most obvious and elegant consequence of these experiments is to take advantage of the tuneability of the laser and perform two experiments on the same solution, exciting selectively the solute and thereafter the solute by a change in wavelength of the laser. By a suitable scaled subtraction approach it should become possible to "undress" the solute from the bulk.

For the NIR experiment on pure CH_3OH a complete set of data for time delays from 100ps to 1μs were collected. These data can be used to answer other interesting questions:

- can the solvent response be described at any time delay as a linear combination of the two differentials as in the equation below?

$$\Delta S(t) = \left(\frac{\partial S}{\partial T}\right)_{\rho} \Delta T(t) + \left(\frac{\partial S}{\partial \rho}\right)_{T} \Delta\rho(t) \tag{4.8}$$

- Can we model the data theoretically and describe the hydrodynamics of the system, i.e. the evolution as a function of the time of the density and temperature of the solvent? [86]

- What can we learn from the real space analysis? Is it possible to understand rearrangements on the atomic length scale induced by the heating in methanol?

These questions show how this experiment opens new perspectives on atomic scale structure and hydrodynamics of pure liquids that can be investigated by ultrafast time resolved X-ray diffraction.

Chapter 5

In this chapter we finally show the Time Resolved X-ray Diffraction data collected for Br_2 in CCl_4, HgI_2 and $HgBr_2$ in CH_3OH. After illustrating the complete fitting procedure we present the obtained results for the reaction dynamics of the studied systems. The Br_2 in CCl_4 relaxation dynamics is compared with the I_2 one, in the same solvent, studied by Plech et al. [1]. The more challenging experiments of HgI_2 and $HgBr_2$ in CH_3OH are discussed in parallel and analysed in the framework of the MD and experimental measured solvent response based global fitting procedure, shading light on the actual reaction pathways.

Résumé du chapitre 5

Dans ce chapitre conclusif, nous allons révèler les données expérimentales obtenues grâce à la diffraction des rayons X résolue dans le temps sur les solutions de Br_2 in CCl_4, HgI_2 et $HgBr_2$ in CH_3OH. Après avoir expliqué la procédure adéquate complète utilisée, les résultats obtenus de la dynamique des réactions des systèmes étudiés sont présentés. La dynamique de relaxation du Br_2 photo excitée dans CCl_4 est confrontée avec celle du I_2 dissolue dans le même solvant étudiée par Plech et al. Les expériences plus ambitieuses performées avec les deux molécules HgI_2 et $HgBr_2$ dissolue dans CH_3OH sont comparées pas à pas et analysées dans le cadre de la procédure du "global fitting" basée sur les simulations de la Dynamique Moléculaire et sur l'étude espérimental de la réponse du solvant, qui nous permet finalement d'identifier les parcours de recombinaison pendant l'évolution de la réaction.

Chapter 5

Dissociation and recombination dynamics of Br_2, HgI_2 and $HgBr_2$ in solution: the data, analysis and results.

The time resolved X-ray diffraction data collected for the study of the dissociation and recombination dynamics of Br_2 in CCl_4 and HgI_2 and $HgBr_2$ in CH_3OH will now be examined. The general description of the data collection strategy and the experimental set-up for liquid diffraction has been already presented in Chapter2 (see sections 2.2, 2.3) and the different experimental parameters used in the three experiments have been reported in Tables 2.2, 2.3, 2.4, 2.5 in section 2.5. The data reduction, normalisation and scaling procedures that we need apply to correctly obtain the difference diffraction curves starting from the 2-D CCD images collected have been already discussed in the previous chapter while describing the NIR experiment on pure methanol (section 4.2.2). In this chapter we will thus discuss only some peculiar aspects of each experiment and then focus our attention on the models used to theoretically describe and fit the data before finally examine and discuss the results.

5.1 Formal model of the difference X-ray diffraction signal from a solution during a chemical reaction

In order to formally express the difference signal from a solution during a chemical reaction we will first summarise some fundamental concepts. Basically we now want to present the formal expression that explicitly shows the information in the difference signals, the timescales and the different contributions we need to include to theoretically model the structural parameters and the parameters describing the reaction dynamics.

The main question is: once we optically trigger a chemical reaction in solution what do the X-rays see? As explained in the first chapter, when we photo-excite a chromophore by an ultrafast (from hundreds of fs to some ps) laser pulse, the molecule breaks into non-bonded atoms or forms a hot molecule with a bigger bondlength. Immediately after the excitation the solution can be thought as a web of hot spots in the solvent, where the temperature distribution is thus highly non uniform but becomes locally uniform in about 50ps at typical solute concentrations. Our time resolution is limited to ∼100ps, from the temporal width of the X-ray pulse. This means that we are blind to bond breakage dynamics and that the in-cage recombination dynamics and the thermal smearing in the solvent are on the borderline of being resolved. What we can determine once the thermal equilibrium is reached, is the atomic composition and structure of the reaction products, and to follow the diffusive recombination (tenth of ns) of the possible transient structures formed in solution. Specifically we can determine how the concentration of these species evolve with time until the end of the reaction, check if it is a reversible process or not and see how the solvent changes its density due to thermal expansion, on the scale of time of the pressure wave propagation in the solvent (typically hundreds of ns), in order to accommodate the new and higher temperature in a larger volume. Assuming that

- we can model the structural contribution of the different species assuming that the evolving structures are independent of the thermodynamical variables,
- in the high dilution limit solute-solute correlations can be neglected,
- the time needed for the solvent to rearrange around the new transient molecular structures is faster then our resolution,

the diffraction signal can be split into two terms, a solute term and a solvent term, the latter depending only on a temperature and density versus time:

$$S(Q,t) = \sum_k N_k(t) S_k(Q) + S_{solv}(Q, T(t), \rho(t)) \tag{5.1}$$

where k represents all possible solute structures and $N_k(t)$ their number as a function of time, i.e. the population dynamic. Consequently the difference patterns, can be written as:

$$\begin{aligned} \Delta S(Q,t) = &\sum_k N_k(t) S_k(Q) - N_0 S_0(Q) + \\ &+ \left(\frac{\partial S(Q)}{\partial T}\right)_\rho \delta T(t) + \left(\frac{\partial S(Q)}{\partial \rho}\right)_T \delta\rho(t). \end{aligned} \tag{5.2}$$

where N_0 is the number of excited parent molecules. Note that non excited solutes cancel out in $\Delta S(Q)$ and that $S_k(Q)$ and $S_0(Q)$ includes the solute-solvent terms. As $S_k(Q)$ is time independent we assume explicitly that the time dependence of $\Delta S(Q)$ is due to changes in populations plus a moving solvent structure. In other words all transition states are ultrafast and only visible through the temperature rise in the

solvent. The situation is thus that we do not expect to see atoms move in the solute structures, whereas we easily resolve the expansion of the solvent. The dynamics has thus two dependent terms: the chemical structures with time dependent concentrations and a physical term expressing the hydrodynamics of the solvent. Of course these two terms are not independent as the reaction dynamics release heat into the solvent as a time dependent heat source. To theoretically build up a difference signal as in eq.5.2, we need to include every possible transient structure that we obtain from the DFT and MD simulations. Then we need to give an expression for the density, and temperature evolutions $\Delta T(t)$ and $\Delta\rho(t)$. One can show that $\Delta T(t)$ and $\Delta\rho(t)$ can be expressed as a function of $\Delta P(t)$, which is a convolution integral of the time dependent heat source $\frac{\partial f_Q(t)}{\partial t}$ and the pressure response to an "instantaneous" heating, i.e. $Q(r,t) = Q(r)f_Q(t)$, where $f_Q(t)$ is the Heavyside function $f_Q(t) = 1$ when $t > 0$ and $f_Q(t) = 0$ when $t \leq 0$. Defining $\sigma = (C_V - C_P)\frac{\chi_T}{\alpha_P}$, where χ_T is the isothermal compression coefficient, α_P is the isobaric thermal expansion coefficient, and C_P is expressed per mole we have [9, 57]

$$\Delta P(t) = \int_{-\infty}^{t} \frac{\partial f_Q(t')}{\partial t} \delta P_{inst}(t')dt' \tag{5.3}$$

$$\Delta T(t) = \frac{f_Q(t) - \sigma\Delta P(t)}{C_P} \tag{5.4}$$

$$\Delta\rho(t) = \rho_0[\chi_T\Delta P(t) - \alpha_P\Delta T(t)] \tag{5.5}$$

with ΔP in Pascal, ΔT in Kelvin and $\Delta\rho$ in kg/m^3.

Without going into details, $\delta P_{inst}(t)$ (as well as the ensuing $\delta T_{inst}(t)$ and $\delta\rho_{inst}(t)$) can be obtained semianalytically by solving the linearised hydrodynamics equations for r=0, i.e. in the centre of the laser pulse which is considered to have a gaussian profile [43, 57, 87, 86]. In Fig.5.1 we show the behaviour as a function of time of pressure, temperature and density for instantaneous heating on the short time scales, the interesting ones for the considered chemical reactions. We observe the plateau of all the three functions: on time scales of the ms though the thermal energy diffuses and the system comes back in the same thermodynamical state as before the excitation.

To complete the description of the effects produced by the heat in the sample we need the two differentials $(\partial S(Q)/\partial T_\rho)$ and $(\partial S(Q)/\partial\rho)_T$: in Chapter 4 we saw how we can either measured or simulate these two terms. The $f_Q(t)$ function is linked to the population dynamics by:

$$f_Q(t) = \frac{1}{R}\left[h\nu\Delta N_0 - \sum_k N_k(t)\Delta E_k\right] + \frac{1}{R}h\nu N_{VC}(1 - e^{-t/\tau_{VC}}). \tag{5.6}$$

In this expression R the ratio between solvent molecules and solute molecules, N_A the Avogadro's number, ΔN_0 is the initial number of excited chromophores, ΔE_k the energy of the different species with respect to the ground state (in J/molecule), as calculated by DFT calculations (section 3.1). The first term (in square parenthesis) of eq.5.6 accounts for the heat released by the reaction, while the second one accounts for ultrafast geminate recombination through vibrational cooling in the cage. Normally we

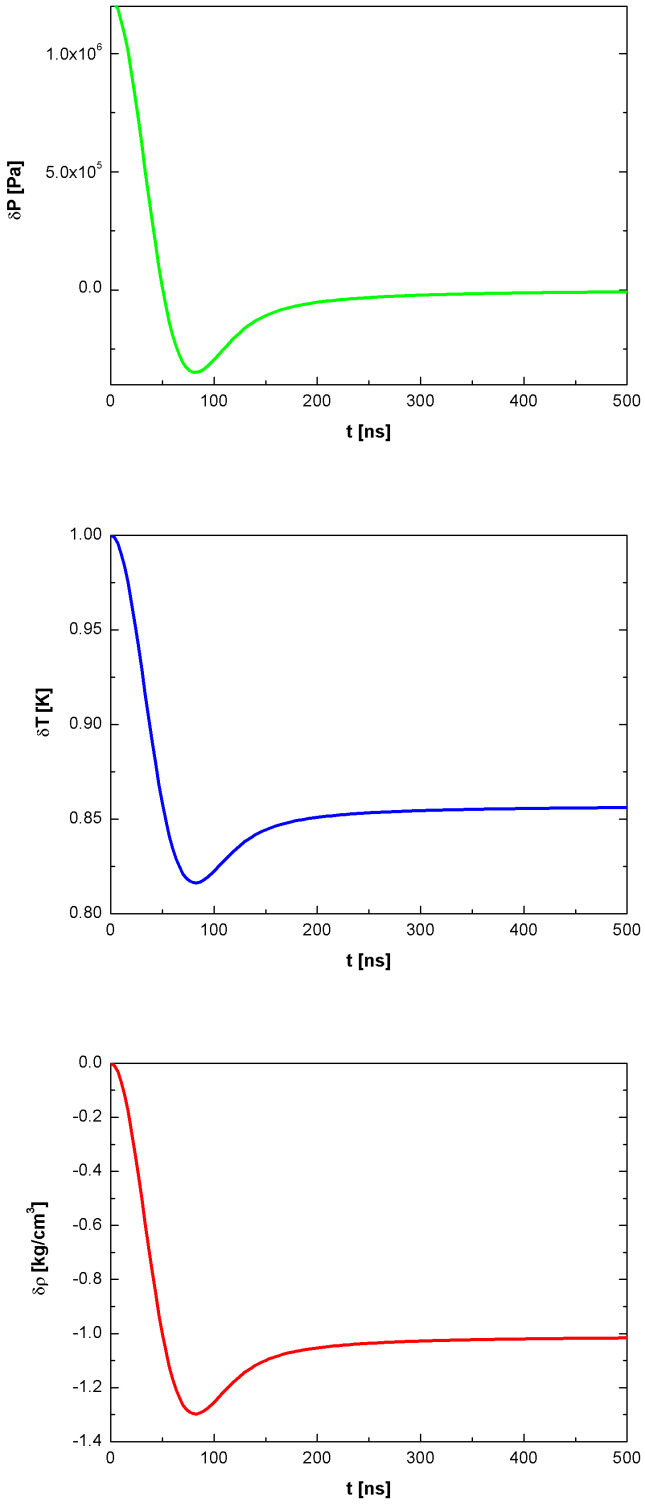

Figure 5.1: Time dependence in the centre of the laser beam for the thermodynamical variables according to linearised hydrodynamics.

cannot resolve the structural signal from fast recombination in the cage, but we see it indirectly through the temperature rise in the solvent. So in the reactions considered in this thesis we fix τ_{VC} to the laser literature value or, if not available, set it to 10ps. Putting together all this information we have a model for our difference pattern which include all the physical and chemical components in the reaction. A global fitting procedure can then be made based on least-squares fitting, where the χ^2 variable is built up on on the entire measured time delays series

$$\begin{aligned} \chi^2 &= \sum_{j=timedelays} \chi_j^2 \\ \chi_j^2 &= \sum_i \left(\frac{\Delta S_{theory}(Q_i, \tau_j) - \Delta S_{exp}(Q_i, \tau_j)}{\sigma_{i,j}} \right)^2 \end{aligned} \tag{5.7}$$

where $\sigma_{i,j}$ is the error on the experimental curves calculated as standard deviation of the repetitions of the same time delay.

5.2 Br_2 in CCl_4

The first system I worked on was Br_2 in CCl_4, which followed the pioneering work on I_2 in CCl_4 by Plech et al. [1]. As we said the experimental parameters, the data collection strategy and the data reduction have been already discussed (see sections 2.2, 2.3, 2.4.1, 2.5). The working concentration of 138mM, i.e. $1Br_2$:$75CCl_4$ was experimentally chosen according to the considerations reported in section 2.4.2: the diffraction signal was indeed checked at different concentrations in order to reach the best compromise between having a good S/N but still keeping the high dilution assumption. Note that 138mM concentration is unusually high for our measurements, which is due to the fact that the molar extinction coefficient for Br_2 at 400nm is quite low. The molar extinction coefficient of Br_2 at 400nm is indeed $\epsilon = 130 M^{-1} \cdot cm^{-1}$ ([16]) while for instance the molar extinction coefficient of I_2 at 520nm ([1]) is $\epsilon = 800 M^{-1} \cdot cm^{-1}$) ([68]).

5.2.1 Data and data analysis

In Fig.5.2 we present the time resolved diffraction signals as a function of time delays obtained for Br_2 in CCl_4.

In panel (a), we observe first of all the 2-D difference maps: and in particular as a check of the accurate timing we observe that the image at -100ps shows no difference intensity. Then at positive times, we observe difference features emerge and progress with time. As the $\Delta S(Q,\tau)$ curves are direct experimental data, the sine Fourier transform $r\Delta S[r,\tau]$ of the $Q\Delta S(Q,\tau)$, shown in panel (c) in Fig.5.2, normalised and integrated with a damping factor $exp(-Q^2\alpha)$, $\alpha = 0.03$ Å ^{2} (eq.2.25) measure the average change in the radial atom-atom distributions, which is dominated by the motion of the pairs Br-Br, Cl-Cl, and Br-Cl, as a function of time. This representation provides a more

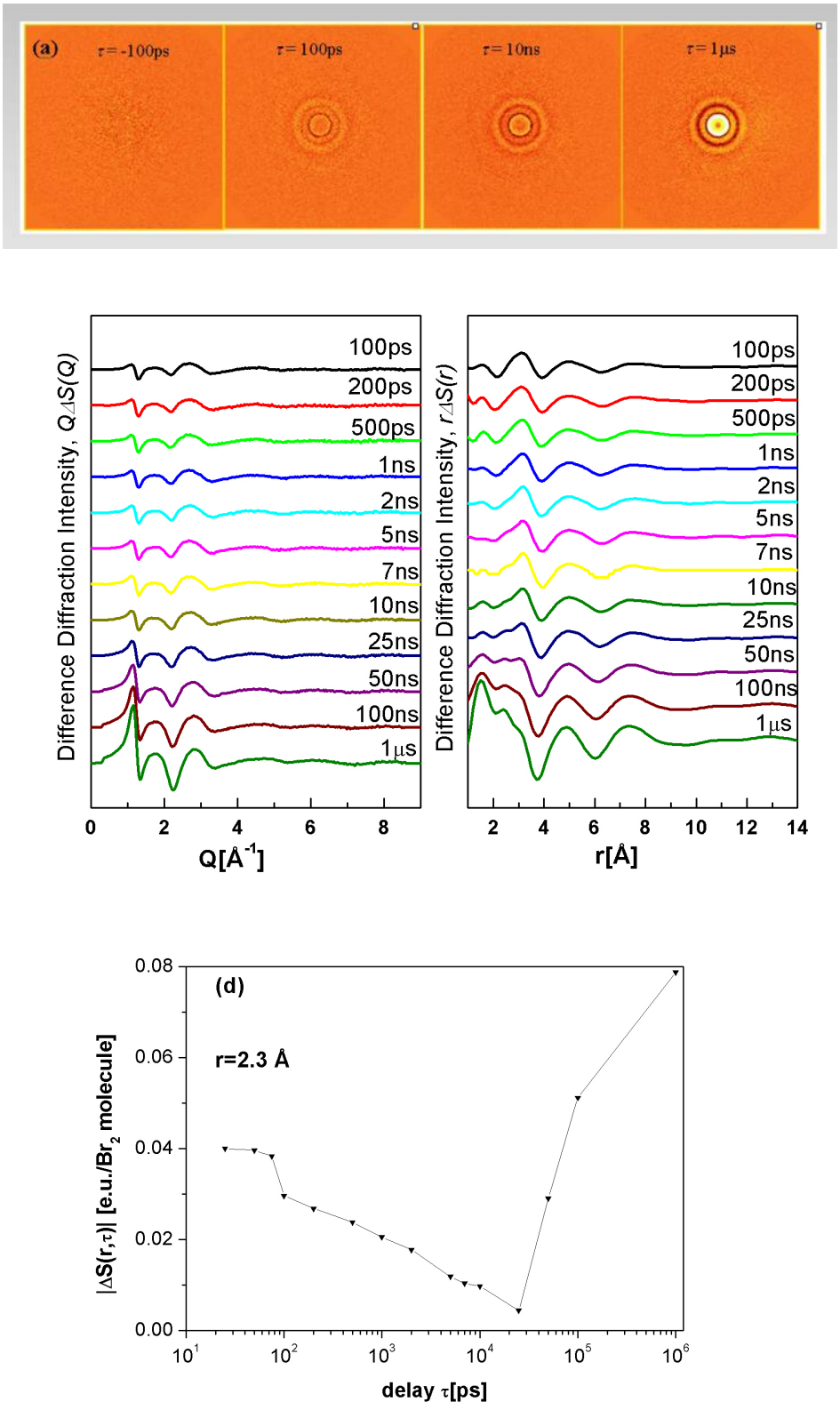

Figure 5.2: Time resolved diffraction signal as a function of time delays for Br_2 in CCl_4. (a) Raw difference images for time delays $\tau = -100ps, 100ps, 10ns, 1\mu s$. (b) Difference diffraction intensities. (c) Difference radial distribution functions. (d) τ-resolved scan of the absolute value of the difference diffraction intensities at r=2.3Å.

intuitive picture of the structural changes in real space. There are three contributions to the measured difference signal: the structural change of the solute, the solvation cage, and the structural rearrangement of the solvent. The high Q range, Q>4.3Å^{-1} probes predominantly the naked solute structures as they relax progressively towards the ground state. By contrast, the low Q range, Q<4.3Å^{-1}, probes both the thermal excitation of the solvent, which is heated by relaxing solute molecules, and the new cage structures. Correspondingly, the lowest r region probes the solute and solute-solvent dynamics, while the high r region is dominated by solvent dynamics. We want to focus our attention at first on the high Q (low r) region, and discuss the structural evolution of the (naked) bromine molecules. The first minimum at 2.3Å at early times can be assigned to the depletion of the $Br_2(X)$ ground state from the laser excitation. Some of the excited molecules reach the A/A' electronic states and a maximum appears at 3.1Å. Note that the depth of the Br_2 hole is a measure of the concentration of dissociated Br_2 molecules: at early times the hole is deep and the depth decreases with time as the recombination proceeds. The hole area should equal the area of the positive bromine peaks after radial integration (weight factor $4\pi r^2$). The relative peak areas for the 2.3 and 3.1Å indicates that part of the 3.1Å peak comes from the solvent. From laser spectroscopic study, [70], the recombination process through vibrational cooling along the X PES can be described by an exponential time constant of 140ps. From 7 to 10ns the negative peak at 2.3Å stays constant, which indicates that very few bromine molecules recombine to the ground state. In the time window 25ns to 1μs, all the excited bromine molecules recombined to the ground state and the negative peaks at 2.3Å disappear; the solution start to expand and the density decreases due to the heat release. Fig.5.2 (c) shows the τ-resolved scans of the absolute values of the difference signal $|\Delta$ S(r, $\tau)|$ at r=2.3Å. At $\tau \leq 25ns$, the τ-resolved signals decrease with time, $|\Delta$ S(r, $\tau)|$ probes the relaxation and recombination of excited bromine molecules; starting from 25ns, the signals increase with time, and $|\Delta S(r,\tau)|$ probes the thermal expansion of the solvent. To obtain a quantitative description of the evolution of the bromine molecule in the α, β, and γ states, the experimental data were modelled, according to the previous discussions (5.1) writing $\Delta S(Q,\tau)$ as:

$$\Delta S(Q,\tau) = \Delta S(Q,\tau)_{bromine} + \Delta S(Q,\tau)_{solvent},$$

with

$$\Delta S(Q,\tau)_{bromine} = n_\alpha(\tau)\Delta S_{Br_2,\alpha}(Q) + n_\beta(\tau)\Delta S_{Br_2,\beta}(Q) + n_\gamma(\tau)\Delta S_{Br_2,\gamma}(Q)$$

and

$$\Delta S(Q,\tau)_{solvent} = (\partial\Delta S(Q)/\partial T)_\rho \Delta T(\tau) + \partial\Delta S(Q)/\partial\rho)_T \Delta\rho(\tau)$$

where n_X is the concentration of the specie X. The solute contribution $\Delta S(Q,\tau)_{bromine}$ and the solvent structure differentials were simulated from MD. The MD structure factor of CCl_4 and its derivatives with respect to temperature at fixed pressure or fixed volume, and the theoretical diffraction signals from bromine in the CCl_4 solvation cage in the ground or excited states or, for atomic Br in solution, were evaluated, as

we previously discussed using the MOLDY program (section 3.2). For the details of the simulations performed on Br_2 in CCl_4 we refer to section 3.3, where this system was used as example for describing how to calculate theoretically all the contributions to model the scattering signals.

In Fig.5.3 we show the experimental and theoretical curves for various reaction channels at early, media and late time delays to demonstrate the structural evolution of the excited Br_2. Statistical least-square refinement χ^2 was used in the fit of the experimental data with theory at each time point:

$$\chi^2 = \sum_{Q_{min}}^{Q_{max}} \left(\frac{\Delta S_{exp}(Q,\tau) - \Delta S_{theory}(Q,\tau)}{\sigma(Q)} \right)^2$$

where $\Delta S_{exp}(Q,\tau)$ is the difference experimental data at a given time delay τ, $\Delta S_{theory}(Q,\tau)$ is the difference molecular scattering intensity, $\sigma(Q)$ is the standard deviation at each Q position. χ^2 was calculated to evaluate the quality of the fit and the procedure was repeated until the best fit between experiment and theory was reached, that is, the χ^2 value was minimised. By varying the occupancies of bromine at α, β, and γ states and applying the least square refinement, the population change of Br_2 molecules at α, β, and γ states as a function of time delay τ was obtained and shown in Fig.5.3 (c). The results show that 55% of the excited bromine molecules recombine along the X PES through vibrational cooling, 35% are trapped to the A/A' excited states and recombine geminately, and only 10% of excited bromine molecules escape the solvent cage and recombined nongeminately, indicating that the potential barrier of the CCl_4 solvation shell is quite efficient in trapping the bromine atoms in the cage. The solid curves shown in Fig.5.3 (c) are calculated according linking the concentration of the species during the reaction:

$$n_\alpha = 1 - n_\beta(\tau) - n_\gamma(\tau),$$

$$n_\beta(\tau) = n_\beta \exp(-\tau/\tau_\beta),$$

$$n_\gamma(\tau) = n_\gamma/(1 + 2k[Br]\tau),$$

where n_β and n_γ are the initial populations of the states β and γ, which are the populations at 25ps in the present study. τ_β is the lifetime of the excited A/A' state, 5.5ns for bromine. k is the rate constant for non-germinate recombination and [Br] the initial bromine concentration of γ state. The lifetime of 25ns and the concentration of 14mM for the γ state were used in the calculation.

In Fig.5.4 it is possible to observe the τ-resolved scans with fixed Q=1.1Å^{-1}. At Q<4.3Å^{-1}, the signal increases with time. The photoexcited bromine molecules relax back to the ground states, releasing energy to the solvent, which makes the solvent expand, as observed in the case of iodine [1]. From what we said in section 2.2.3, the change in (mass) density of the solvent is the small r-limit of $\Delta S(r,\tau)$ [69, 46]:

$$\Delta S[r,\tau] = -\Delta\rho(\tau)$$

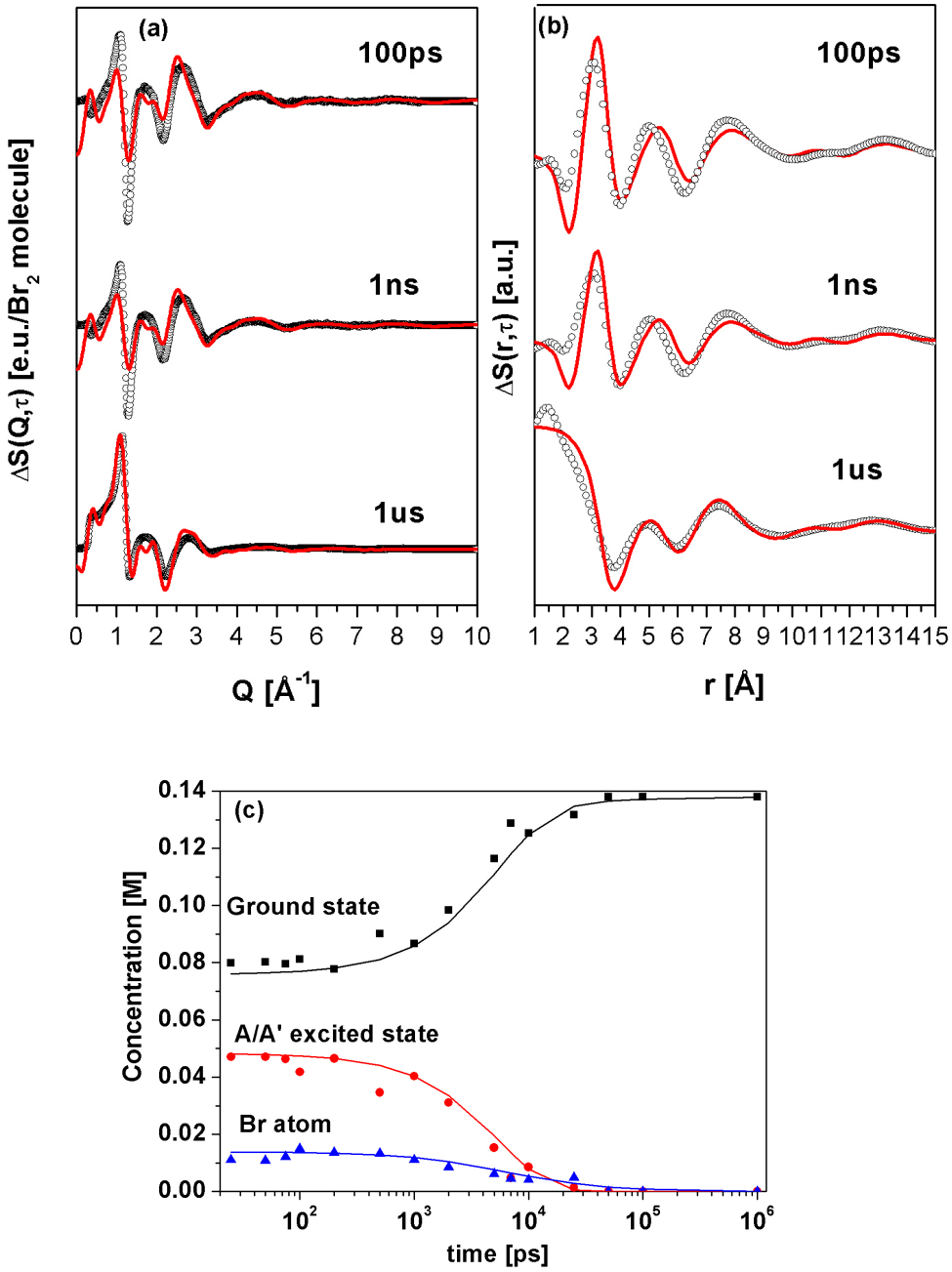

Figure 5.3: (a) The Q-resolved scans $\Delta S(Q,\tau)$ for the time delays 100ps, 1ns and 1μs. (b) The change in the atom-atom pair distribution $\Delta S(r,\tau)$ for τ=100ps, 1ns and 1μs. The labelled curve shows the experimental data, and the solid curve is the full model. (c) The population change of the α, β, and γ states with time: the scatter curves are determined by fitting the experimental data with the full model with least square refinement, the solid curves are calculated from theory.

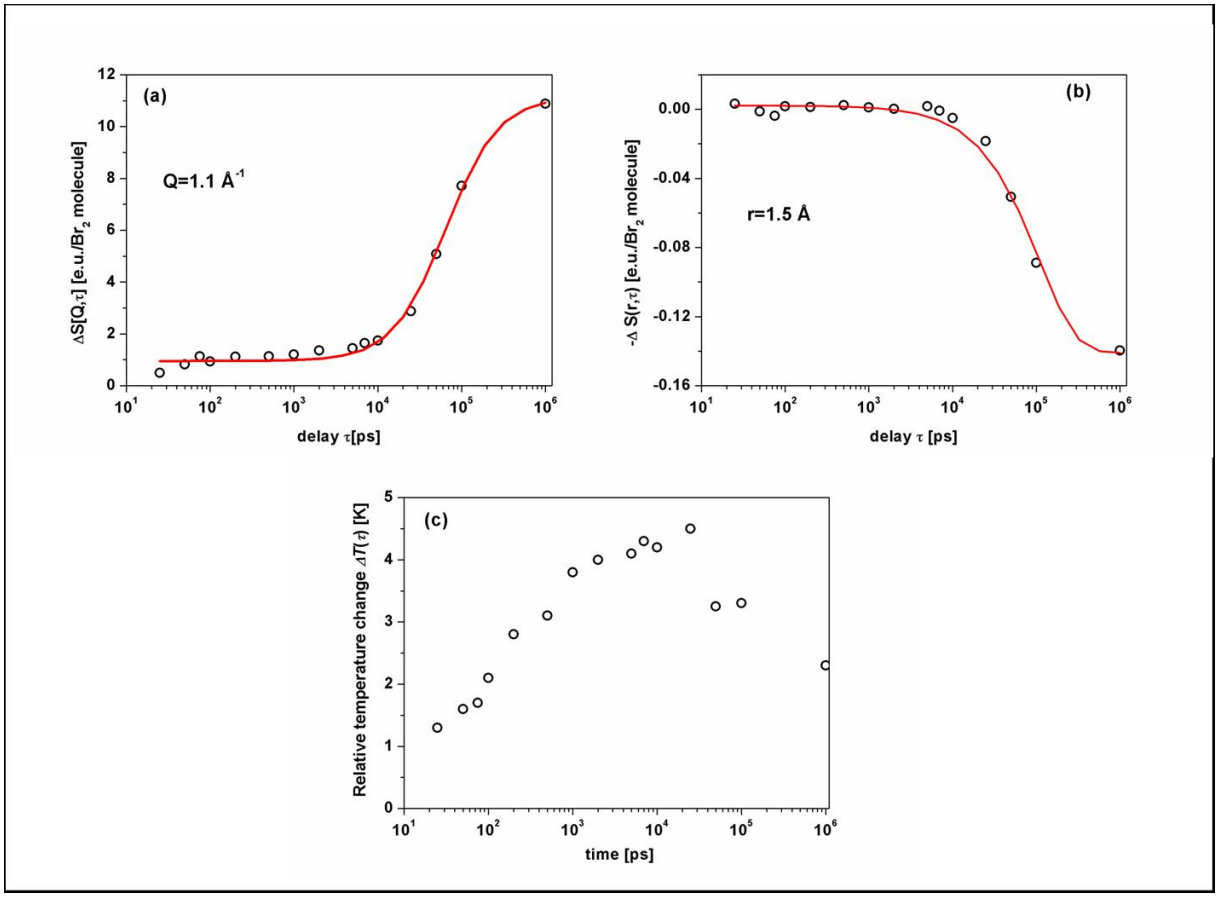

Figure 5.4: Structural dynamics of the solvent. (a) The τ-resolved scans $\Delta S(Q,\tau)$ at Q=1.1Å^{-1}, the signal of the solvent increases with time due to the relaxation of energy from excited bromine. (b) The τ-resolved scans $\Delta S[r,\tau]$ at r=1.5Å, indicating the density of the solvent decrease due to thermal expansion starting from 10ns. The curves are a guide for the eyes. (c) The solution temperature change with time, $\Delta T(\tau)$.

if the sine Fourier transform of the experimental curves in Q-space $Q\Delta S(Q,\tau)$ is properly normalised according to eq.2.25. Using the difference experimental signal $\Delta S[r,\tau]$ at r=1.5Å, the variation of the mass-density can be followed in real time as shown in Fig.5.4 (b). The photoproducts revert to the ground state through collisions with the solvent, the solvent takes up the excess energy and expands. The vibrational cooling process reacts its $1/e$ point after 140ps, and the relaxation of the A/A' states finish after 5.5ns. The thermal expansion starts after 10ns: the energy released to the solvent at earlier times induces the temperature and pressure changes at constant volume. When the thermal expansion starts after $\sim$ 10ns, the density of the solvent drops as shown in Fig.5.4 (b), while the pressure keeps constant. The temperature change with time, $\Delta T(\tau)$, was obtained by fitting the experimental data with the theoretical model as shown in Fig.5.4 (c). The temperature reaches its maximum around 25ns, where the temperature has risen of 4.5K which is higher than the of 3K observed in the I_2/CCl_4 experiment. This is in part due to the excitation wavelengths, 400nm and 520nm, respectively. Fig.5.2(c) shows that two minima at 3.8Å and 6.1Å appear at early times and their amplitude grow with time. The two negative peaks are from a broadening, at constant volume, of the intermolecular $Cl..Cl$ distances of the CCl_4 molecules. These two distances coincide with the two CCl_4 intermolecular peaks that we found in the high energy X-ray diffraction experiment on pure CCl_4 as shown in Fig.4.3. What should be noted is that, the structural rearrangement of the solvent is not an artifact of direct laser heating; it results intrinsically from the recombination of hot bromine molecules and atoms, which were also observed in the iodine experiment [1]. The energy transferred from the excited solute molecules to the solvent gives a tiny structural perturbation in space of a few mÅ, but considering the larger number of solvent molecules, the signal becomes comparable to that of the solute.

5.2.2 Br_2 vs I_2 in CCl_4

The branching ratio for cage escape (γ state) and recombination into the ground (α state) and excited (β state) states were determined to be 10%, 55% and 35% respectively for bromine in the present study. For comparison, 20% of excited iodine molecules recombine into excited A/A' states, and 14% escape the cage [1]. The comparable amount of dissociated molecules (10% for I_2, 14% in the case of Br_2) can be understood in terms of the comparable kinetic energy of the atoms, respectively $\simeq$0.9eV for I_2 and $\simeq$1.2eV for Br_2. This energy is estimated as $E_{laser} - E_{dissociation}$, with E_{laser}=2.4eV (520nm) for I_2, where $E_{dissociation} \simeq$ 1.5eV [1] and E_{laser}=3.1eV (400nm) for Br_2 which has $E_{dissociation} \simeq$ 1.9eV, (see Fig.1.1). The 5.5ns lifetime of A/A' state for bromine is much longer than that for iodine of 2.7ns. The longer lifetime of bromine is attributed to the deeper A/A' well depth than that of iodine [70]. We note that these X-ray populations are different from the laser spectroscopic studies for both iodine and bromine, which showed that 60% of bromine and 30-40% of iodine molecules are trapped in the A/A' excited states [15, 14, 18]. In the following tables (Tab.5.1, Tab.5.2) we summarise the main experimental parameters and the results of the relaxation dynamics for Br_2 and I_2 in CCl_4 studies.

Fig.5.5 compares I_2 and Br_2 in CCl_4 at very early time points in real space. We

	Br_2 **in** CCl_4	I_2 **in** CCl_4 **[1]**
Concentration	138mM ($1Br_2$:$75CCl_4$)	29mM ($1I_2$:$357CCl_4$)
Laser excitation energy	3.1eV (λ=400nm)	2.4eV (λ=520nm)
Dissociation energy	1.9eV	1.5eV

Table 5.1: Summary of the main parameters for Br_2 and I_2 in CCl_4 studies.

Recombination channels	Br_2 **in** CCl_4	I_2 **in** CCl_4 **[1]**
Vibrational Cooling (α state)	55%	66%
Excited A/A' (β state)	35%	20%
Cage escape (γ state)	10%	14%
Temperature rise	4.5K	3K

Table 5.2: Summary of the results of the relaxation dynamics studies of Br_2 and I_2 in CCl_4.

will later how time delays shorter than the 100ps can be obtained (see Conclusions). The low r region shows the structural evolution of the solute molecules. The negative

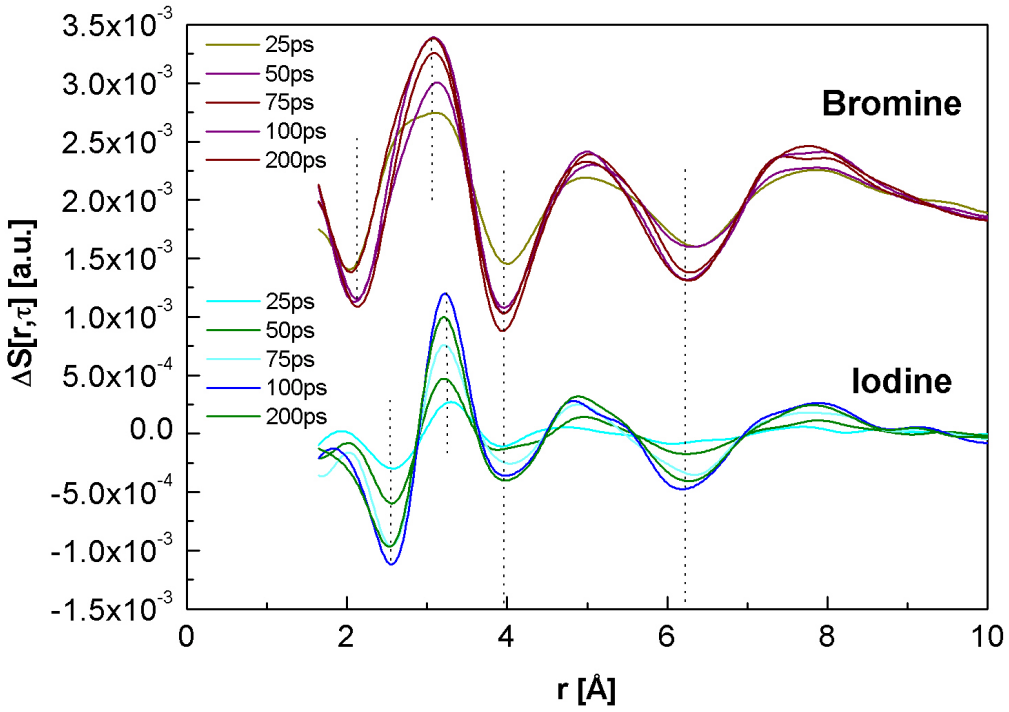

Figure 5.5: Comparison of structural evolutions of I_2 and Br_2 in CCl_4 at early time points.

peaks of 2.3Å and 2.7Å are the ground state structures of bromine and iodine in CCl_4, the positive peaks of 3.1Å and 3.2Å show the bromine and iodine in the A/A' states.

We noted that the negative peaks at 3.8Å and 6.1Å in the high r region are (near) identical in shape, thus independent of the solute, which confirmed the conclusion that they come from structural rearrangement of the pure CCl_4 solvent. The pure solvent reaction in Br_2/CCl_4 is stronger than that of I_2/CCl_4. This comes from the higher laser photon energy (3.1eV of 400nm) used in the present experiments, while 2.4eV of 520nm was used for iodine. What should be pointed out is that the positive peak at 3.1Å of bromine is much broader than that of iodine. We tend to assign the broader peak of bromine in the A/A' state to a contribution from the solvent.

Fig.5.6 compares the τ-resolved scan at Q=4.3Å^{-1}, where the CCl_4 contribution is low, between bromine and iodine. The τ-resolved signals decrease with time in the iodine experiments, while the Br signals are constant or increase with time.

The $\Delta S(q,\tau)$ signal at Q=4.3Å^{-1} predominantly probes the relaxation "naked" iodine molecules[1]. The results shown in Fig.5.6 indicates that the high Q signals in the bromine experiments can not be considered as a "naked" bromine signal, but rather integrates both Br and CCl_4 dynamics. The Br_2 experiment shows thus that the structural recombination and relaxation with Z=35 is more difficult to isolate reliably than that of iodine with Z=53 from the CCl_4 solvent signal.

5.2.3 Discussion

The model proposed above is only in fair agreement with our measurements. The main reason for that is that the early time differential, derived from MD, is of insufficient precision to allow quantitative conclusions about the reaction mechanism to be made. The temperature rise was thus found from fitting four components to the $\Delta S(Q,\tau)$. So the solvent response is not taken correctly into account. The next step to improve this result will be then to proceed in the same way as we did for CH_3OH, i.e. inducing thermal heating on the pure solvent and experimentally measuring the solvent response. Due to the difference in the molecular structure, and in particular to the lack of hydrogen in CCl_4, we could not use NIR as we did for methanol (section 4.2, [64]).

The strategy adopted in a very recent experiment to directly measure the solvent response for CCl_4 consisted in inducing heating in the pure solvent through two-photon absorption, using 400nm radiation. Using the same approach we discussed for the methanol experiment (4.2), my beamline colleagues determined the two differentials $(\partial S/\partial T)_\rho$ and $(\partial S/\partial \rho)_T$, which are shown in Fig.5.7, together with the same differentials obtained from MD simulations.

As we stressed before, several factors influence the accuracy of the simulations, such as the theoretical potentials used, the difficulty in modelling certain force fields efficiently, the use of a finite ensemble of molecules. We can attribute to these limits the discrepancies we observe comparing the experimental differentials with the MD ones (Fig.5.7).

For these reasons is desirable to obtain the solvent-only term experimentally. In Fig.5.8 we compare the fits of the $\Delta S(Q, 100ps)$ performed using the MD and the experimental differential $(\partial S/\partial \rho)_T$ (that as we explained at this time delay is directly measured and is the only solvent contribution) instead of the MD simulated term. We

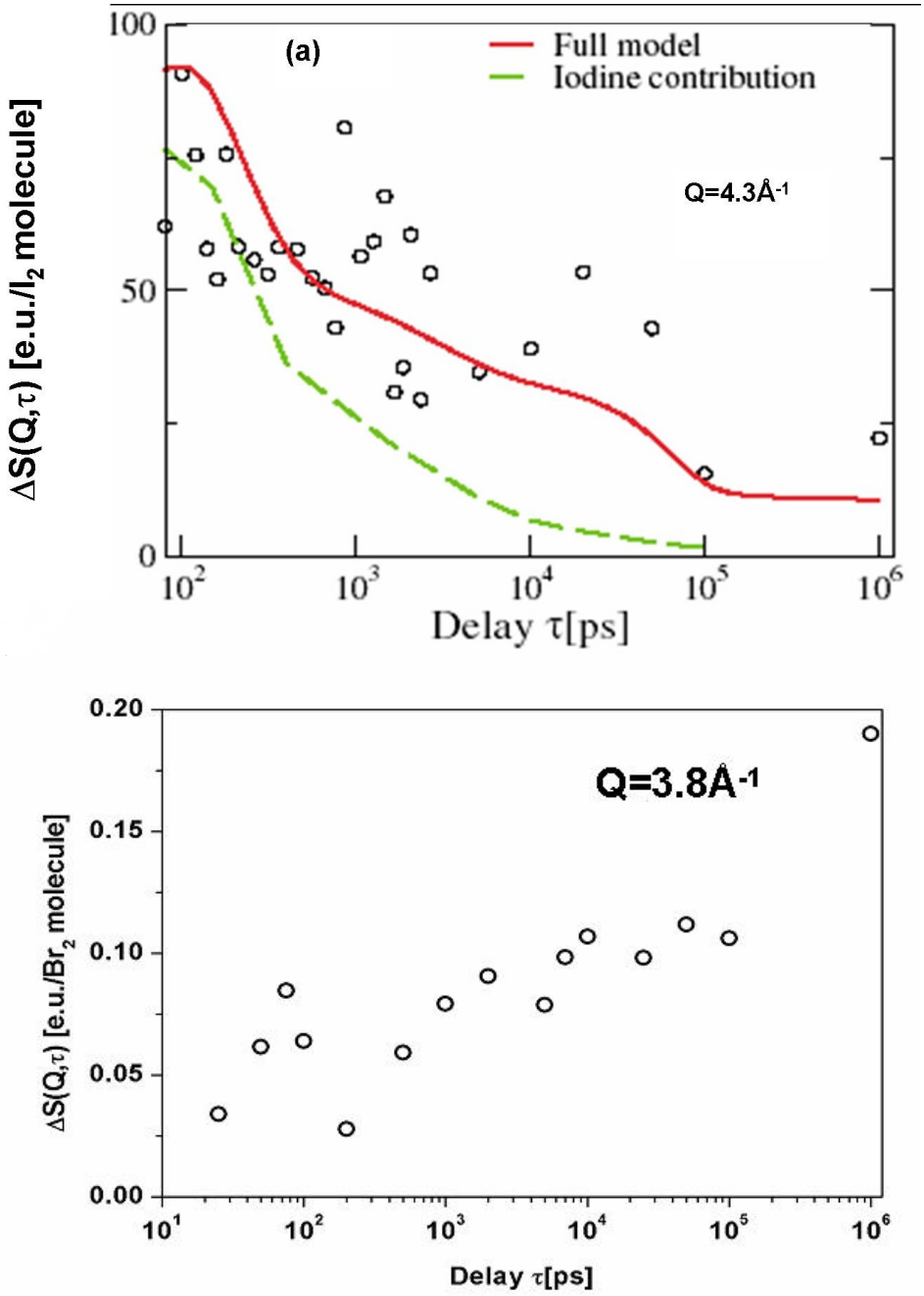

Figure 5.6: The τ-resolved scans $\Delta S(q,\tau)$ at Q=4.3Å^{-}1. Comparison between (a) I_2 in CCl_4 and (b) Br_2 in CCl_4.

can observe the significant improvements in the fit introduced determining experimentally the solvent response.

In order to conclude the study on Br_2 in CCl_4, a global fitting analysis, from which it will be possible to extract all the parameters for the reaction dynamics, using these experimental solvent's differentials is now in progress. These experimental curves will be also used to re-analyse the I_2 in CCl_4 data.

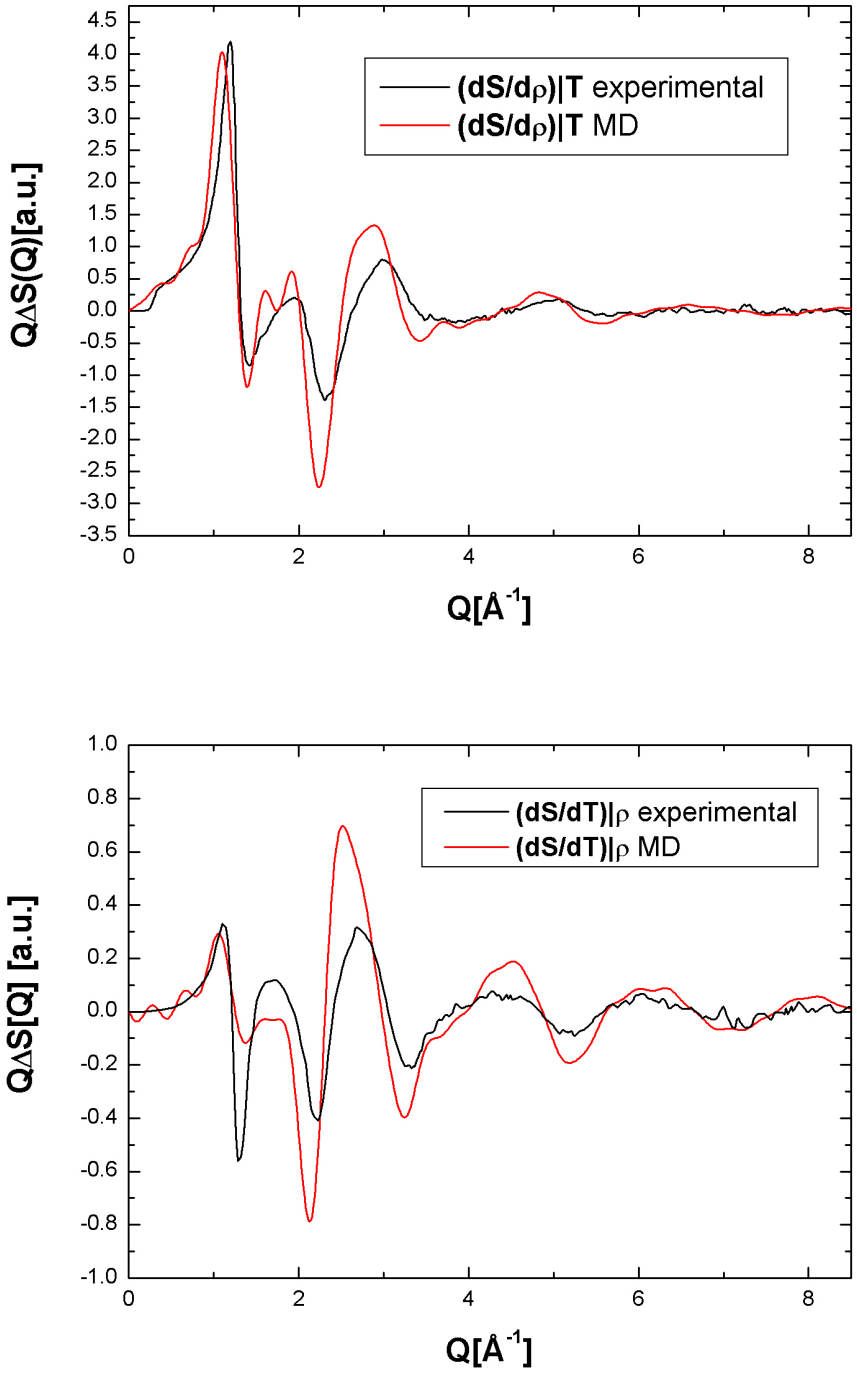

Figure 5.7: In the upper plot we show the comparison between $(\partial S/\partial \rho)_T$ differentials for CCl_4 obtained from MD simulations and experimentally measured from multiphoton absorption. In the lower one the comparison between $(\partial S/\partial T)_\rho$ differentials for CCl_4 obtained from MD simulations and experimentally measured from multiphoton absorption.

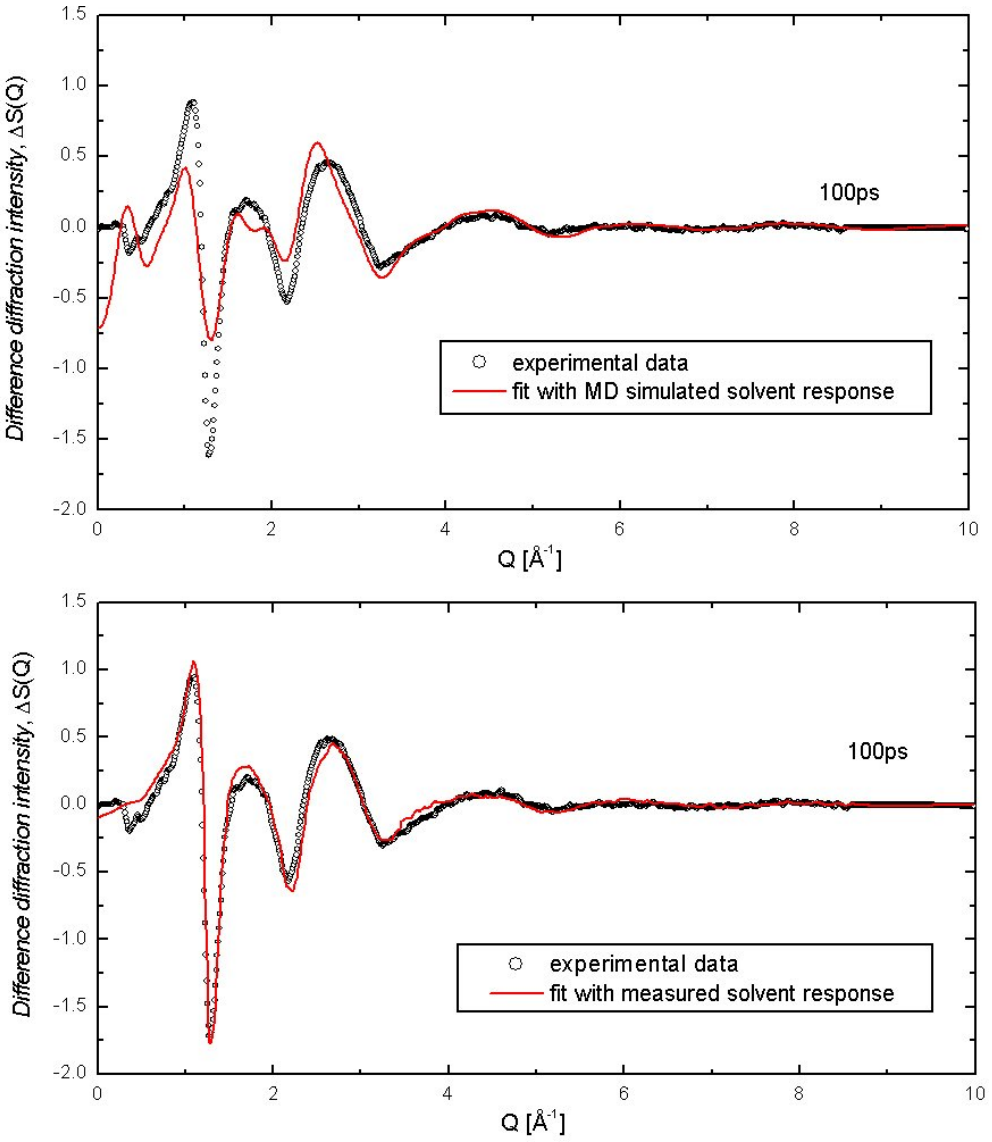

Figure 5.8: Difference diffraction intensity from Br_2 in CCl_4 at 100ps. Comparison between the fit performed using the MD simulated $(\partial S/\partial \rho)_T$ differential (upper panel, same as in (Fig.5.3)) and the fit performed using the experimental differential measured as response of the pure CCl_4 to the heating induced by multiphohoton absorption.

5.2.4 Conclusions

We have described our attempts to study the dissociation and recombination of laser excited bromine molecules by means of 100ps X-ray diffraction from a synchrotron. From our results we can summarise the physical process in this way: 55% of Br_2^* molecules recombine directly through vibrational cooling along the X-potential, 35% are trapped in the A/A' states, while 10% escape the solvation cage and form neutral Br atoms.

The time scales of the recombination of excited bromine molecule at different states coincide with the laser spectroscopic studies.

The thermal expansion and temperature change of the solvent, due to the energy

release from the recombination of excited solute molecules, were detected in real time. We can attribute the oscillations at 3.8Å and 6.1Å in the higher r region to the intermolecular Cl..Cl structural rearrangement of the CCl_4 solvent during the thermal expansion, which are independent of the solute properties. The intermolecular structure of CCl_4 measured from high energy X-ray scattering confirms this conclusion. The temperature rise of the solution is 4.5K, which is higher that of 3K in the iodine case. Compared to the iodine experiments, the stronger solvent oscillation and higher temperature rise could be attribute to the higher energy of the laser photons used in the present study.

5.3 HgI_2 and $HgBr_2$ in CH_3OH

Moving to triatomic molecules, we tried to elucidate the recombination dynamics of HgI_2 and $HgBr_2$ dissolved in CH_3OH, with the motivation reported in Chapter 1 (section 1.2). For experimental details, data collection and data reduction we refer again to sections 2.2, 2.3, 4.2.2 and to Tables 2.2, 2.3, 2.4, 2.5 in section 2.5. Nevertheless we want here to stress two experimental aspects we dealt with during this data collection: the determination of the concentration for the two solutions and the refinement of the temporal overlap between the laser and the X-ray pulse.

5.3.1 Determination of the HgI_2 and $HgBr_2$ concentrations

In order to determine the laser excitation wavelength for the two molecules we had first of all at our disposal from literature, the ultraviolet absorption cross section HgI_2 and $HgBr_2$ in gas phase [79].

Due to the slightly different potentials in the liquid phase, we observed a shift of these peaks. We measured the optical absorption spectra for both HgI_2 and $HgBr_2$ in methanol at 5mM and in a 1mm thick cuvette. In the following plot, Fig.5.10, the absorbance is scaled to $300\mu m$, which is the typical sample thickness in our experiments.

For $HgBr_2$ in gas phase the absorption spectrum exhibits a broad peak at ∼225nm: in the liquid phase this peak is sharper and red-shifted at 238.5nm (with the wavelengths available with our spectrophotometer it is not possible to resolve the first peak observed in the gas phase.) For HgI_2 instead a first peak in gas phase is observed at ∼220nm and a second one at ∼265nm. In the liquid phase we observe a peak at ∼229nm followed by a peak at ∼270nm. This peak value for HgI_2 in CH_3OH at 270nm is very close to the third harmonic (267nm) of the fundamental wavelength of our Ti:sapphire laser system, which was then chosen as suitable excitation wavelength.

The concentration of HgI_2 in solution was then experimentally determined through concentration titration tests, according to the considerations explained in section 2.4.2. We tried indeed different values such that, without observing changes in the shape of the signal from solute-solute interactions, we got the best signal to noise ratio at 10mM. As the molar concentration of methanol is 24.70M, this implies a mixing ratio of $1HgI_2$:$2500CH_3OH$.

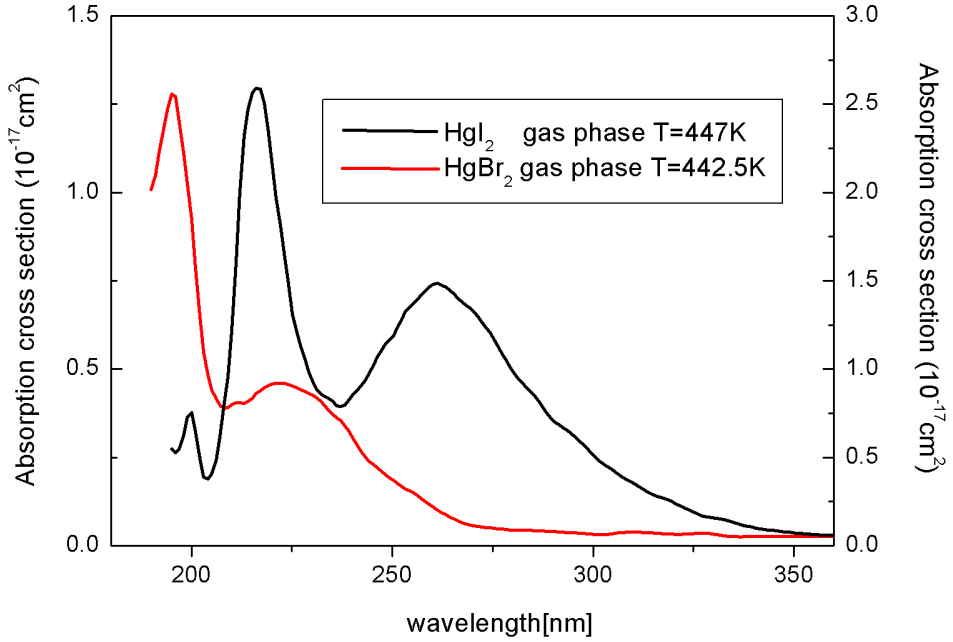

Figure 5.9: Ultraviolet absorption cross section HgI_2 and $HgBr_2$ in gas phase from [79].

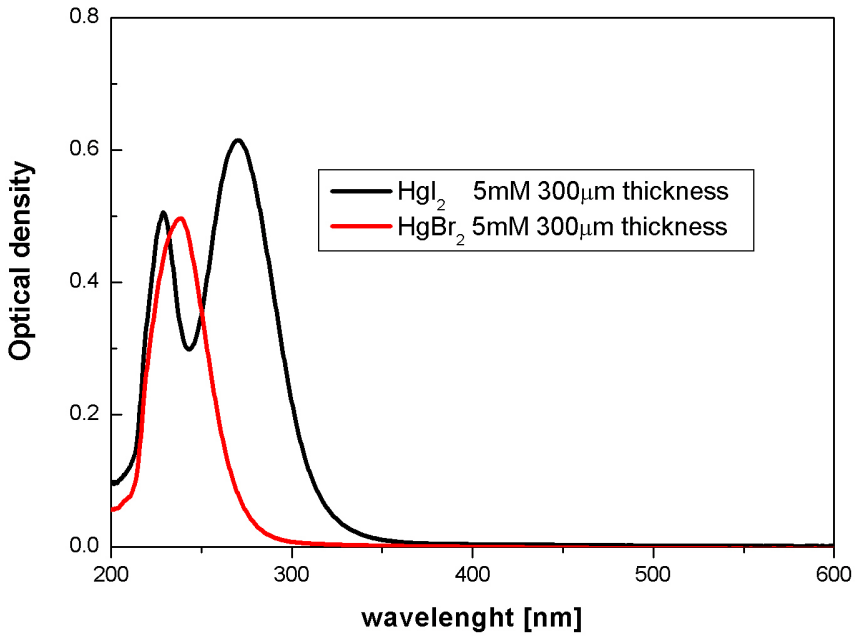

Figure 5.10: Optical absorption spectrum of HgI_2 and $HgBr_2$ in methanol.

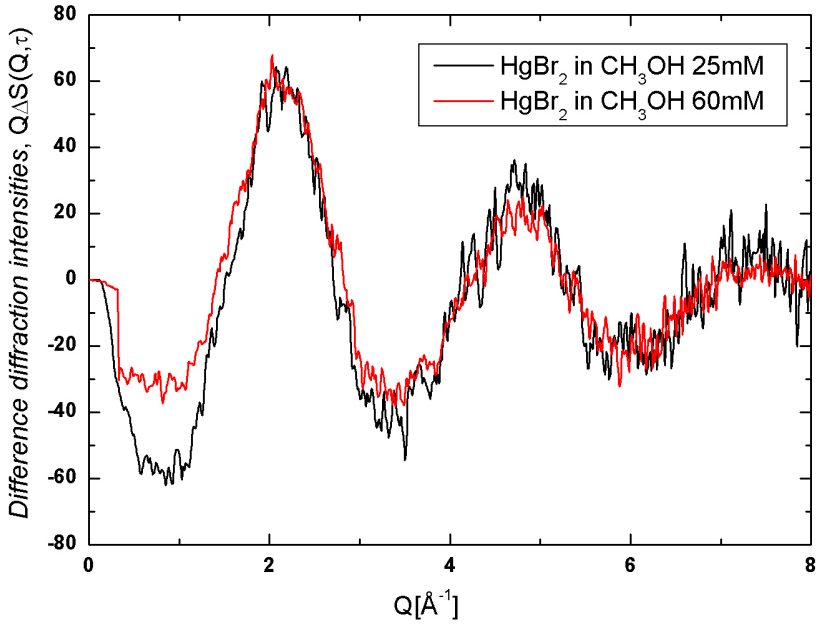

Figure 5.11: Comparison between the $Q\Delta S(Q, 100ps)$ for a 25mM and a 60mM solution to determine the working concentration in our experiment.

In the case of $HgBr_2$ the absorbance at 267nm is 6 times lower than for HgI_2. (Fig.5.10). Thus, without performing a systematic concentration titration test, we checked the diffraction signal of $HgBr_2$ at 60mM (a concentration 6 times higher than the HgI_2 concentration), and at a different concentration (25mM), in order to carefully check to be still in the high dilution limit. In Fig.5.11 we show a comparison between the difference intensities at 100ps for the 25mM and a 60mM $HgBr_2$ solution. After scaling the curves to e.u./solute molecule, the shape of the two curves are basically the same, which allows us to think that in this concentration range, we can neglect solute-solute interactions; nevertheless, in the experiment we kept the lower concentration of 25mM, i.e. a mixing ratio of $1HgI_2$:$1000CH_3OH$.

5.3.2 Refining the temporal overlap between X-ray and laser pulses.

In section 2.3.4 we discussed how it is experimentally possible to refine the spatial overlap between X-ray and laser pulses through the Figure of Merit procedure. In the HgI_2 experiment we used the same approach to refine also the temporal overlap between the pulses, which is generally measured by the fast GaAs detector, with a FWHM resolution of 10-20ps. In Fig.5.12 we show, how this was done experimentally. We started by observing that the evolution of the dissociation signal is a Gauss integral or rather an error function of this overlap. As we explained before, negative time delays

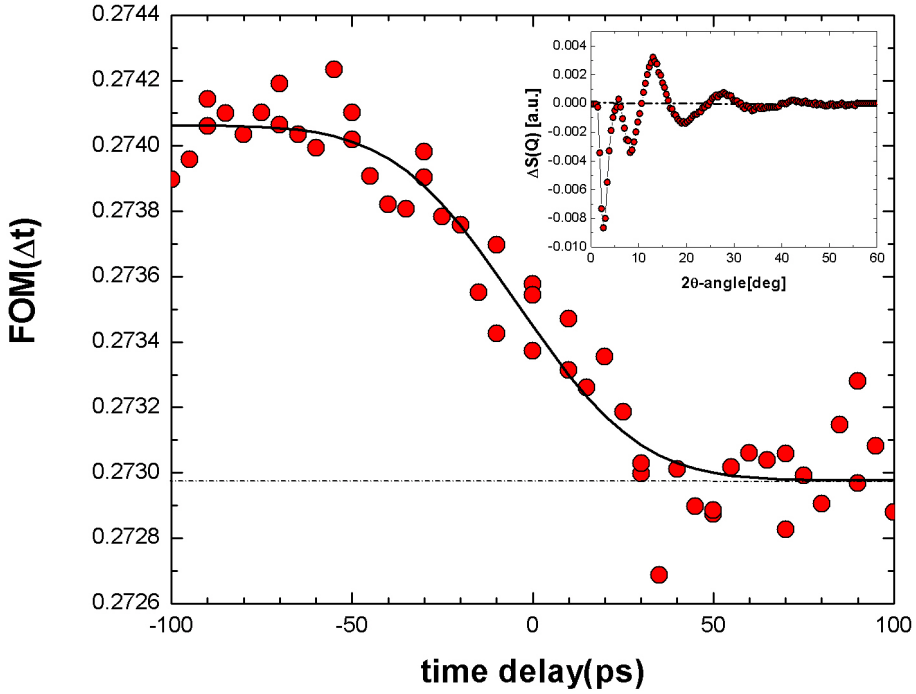

Figure 5.12: Experimental refinement of time zero in the HgI_2 experiment through the definition of the figure of merit FOM. A typical $\Delta S(Q,\tau)$ curve is shown in the insert.

are defined such that the X-ray arrives on the sample before the laser pulse, probing in this way the non-excited sample. When a dissociation event happens it produces a negative signal at low Q values. For the $HgI_2 \rightarrow HgI + I$ Debye transition the laser on minus laser off signal is negative from 0-11°. If the detector is moved out such that the edge of the detector is about 12°, we can define an inner (pixel) disk 2θ<11° and outer disk 11°<2θ<12°. As the laser timing is scanned across time zero, the inner disk integral will decrease with time whereas the outer disk will remain constant due to the isobestic point at 11°. We can assign a number to every CCD image, FOM, defined as the ratio $I(2\theta < 11°)/I(11° < 2\theta < 12°)$ From the definition thus this number will be decreasing as a function of the time delay. Indeed, for negative time delay the X-ray will be probing only non dissociated molecule, while at 100ps, the excited molecules, the number of which is constant during the scan, will be recorded with the full X-ray intensity. If we assume that the dissociation is instantaneous, and that the X-ray pulse $I(t)$ is Gaussian, the FOM scan can be fitted to the error function $erf(t)$ as shown in Fig.5.12. The figure shows that the mid-point of the $erf(t)$ function is -4ps, which is in good agreement with the first measurement with the GaAs detector. The delay time was then corrected for this shift which is in fact comparable with the shift in bunch phase during a fill of the synchrotron.

The -100ps and -200ps time points collected respectively for HgI_2 and $HgBr_2$ allows us to doublecheck the accurate timing between the laser and X-ray pulses, as shown in

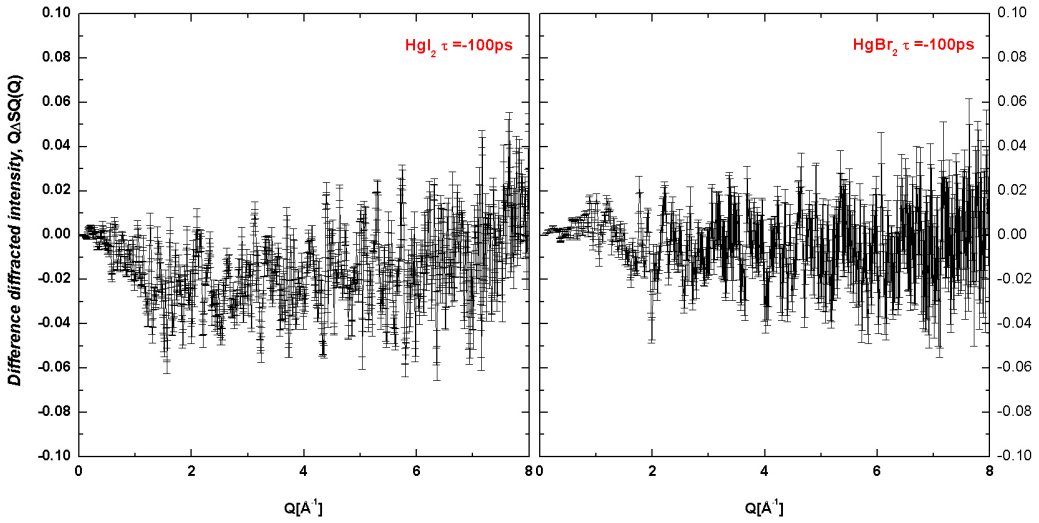

Figure 5.13: Difference diffraction intensities from HgI_2 and $HgBr_2$ for negative time delays: the absence of structures in the signal is a check of the timing between the laser and the X-rays and the stability of the entire experiment including the beamline.

Fig.5.13

5.3.3 Experimental difference maps in Q and real space

As we explained in the data reduction procedure 4.2.2, according to which the data collected for HgI_2 and $HgBr_2$ has been treated, first of all from the absolute units scaling we can determine the fraction of photo-excited solute molecules: in the 10mM concentration of HgI_2 34% of the molecules are excited by the laser pulse, while the photo-excited molecules in the 25mM $HgBr_2$ solution is only $\sim$ 7%. This striking result that lower solute concentration produces a higher excited solute concentration shows the importance of having a low in-depth absorption gradient. If the temperature difference between the entry and the exit of the beam laser is too big, the sample turns non-linear.

In the following plots $\Delta S(Q,\tau)$ have been multiplied by the scattering vector, Q, to magnify the intensity variation at higher Q. The corresponding radial distribution functions $r\Delta S[r,t]$, which probes the radial electron density change as a function of interatomic distance r, was obtained according to eq.2.25 (and performed introducing also the damping factor $exp(-Q^2\alpha)$, $\alpha = 0.03$ Å^2 for HgI_2 analysis and $\alpha = 0.01$Å^2 for $HgBr_2$).

Because in both cases the high-Z solute atoms scatter the X-ray more strongly than the low-Z atoms in methanol, the solute changes stand out in the radial distribution

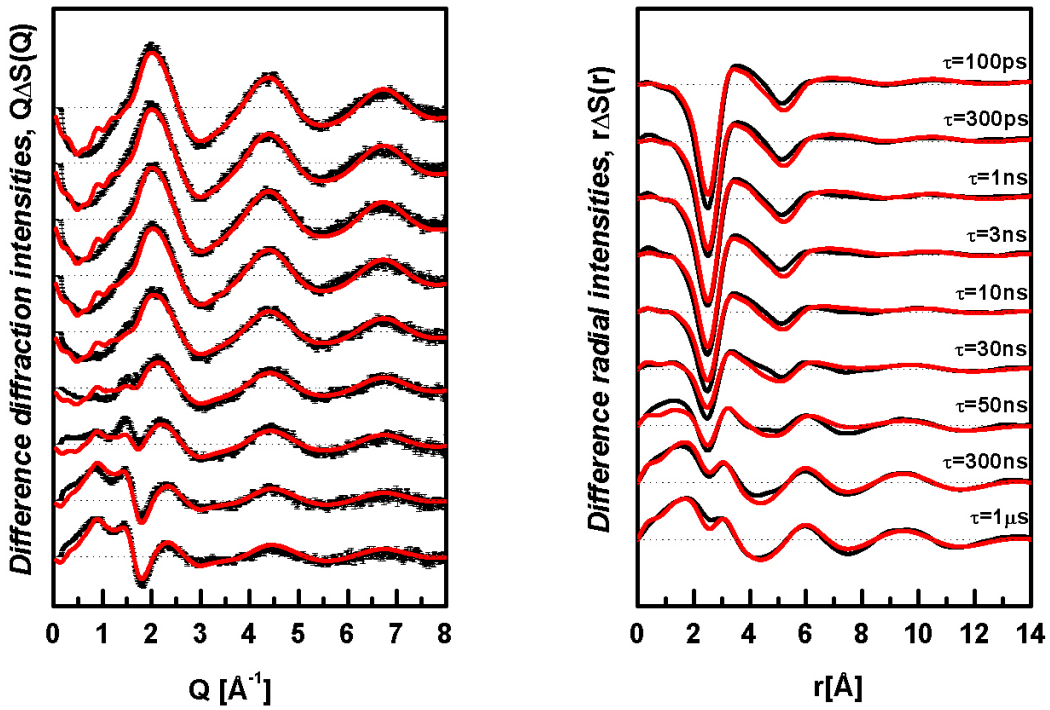

Figure 5.14: Time-resolved diffraction signal as a function of time delay for HgI_2 in methanol. On the left we show the experimental difference intensities (black curves). The theoretical fits to the model, for the dissociation channel $HgI_2 \rightarrow HgI + I$ are also shown (red-curves). In the right panel we show the (normalised) real space transforms of the data (black curves) and the theoretical fits (red-curves)

.

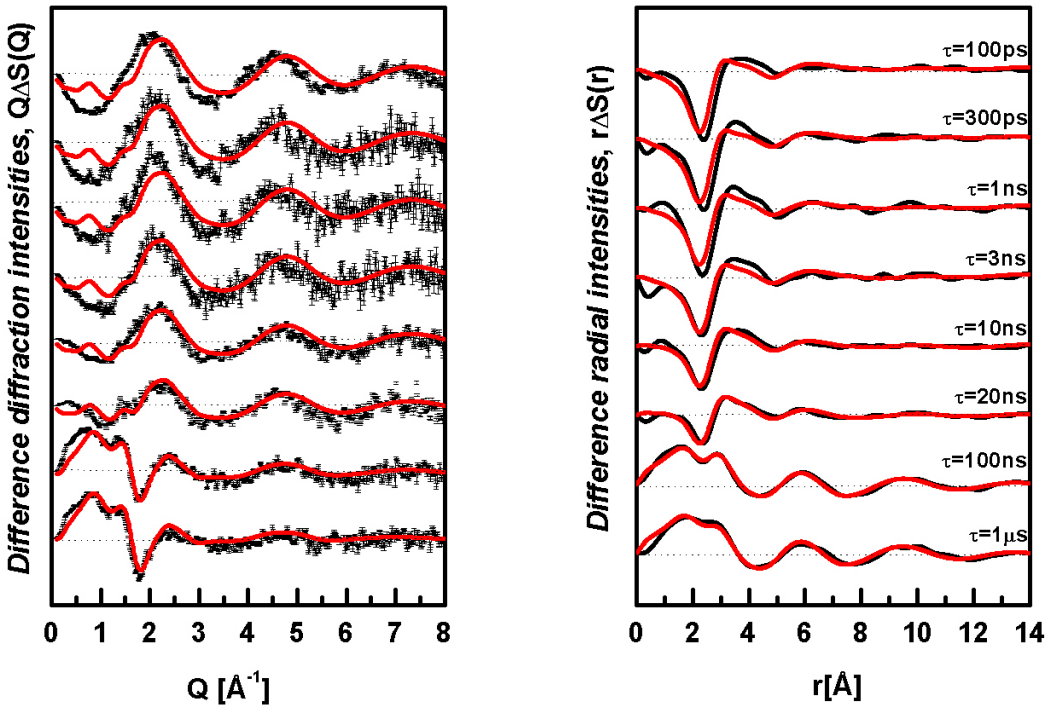

Figure 5.15: Time-resolved diffraction signal as a function of time delay for $HgBr_2$ in methanol. On the left the experimental difference intensities (black curves) are shown together with the theoretical fits (red-curves). In the plot on the right we show the associated (normalised) sine-Fourier transforms to real space. The experimental curves are black and the theoretical fits are red.

functions (section 2.2.4).

The RDFs curves exhibit both negative and positive peaks. In the case of HgI_2 there are strong depletions of correlation at 2.65 and 5.30Å with a corresponding rise at 3.50Å at early times. We find the same features, at different correlation distances, for the $HgBr_2$ curves: here we observe two minima at 2.28 and 4.94Å and a maximum at 3.63Å. The structural parameters of HgI_2 are well known and also confirmed by the DFT calculations made for this study and mentioned before (Table 3.3).

Thus we can easily assign the two negative peaks to the bond breakage of $Hg-I$ in HgI_2. More specifically, 5.30Å corresponds to the depletion of $I\cdot\cdot I$ internuclear pairs in HgI_2, and 2.65Å corresponds to HgI depletion and formation of $Hg-I$ pairs.

The structures of the $HgBr_2$ molecule have been investigated in several theoretical studies and experimentally by gas phase electron diffraction. Some of the results are summarised in [72]. These studies favoured a linear equilibrium geometry, however, the mercury-halogen distances range widely, from 2.378Å to 2.44Å. Our DFT calculations for $HgBr_2$ in methanol gave the distances shown in Tab.3.3. The attribution of peaks and valleys in the case of $HgBr_2$ is more uncertain. This might be in part attributed to the lower signal to noise ratio of this data. Nevertheless, the experimental minimum at 2.39Å is attributed to the breakage of the Hg-Br bond in the $HgBr_2$ molecule, which as a calculated value of 2.35Å. The second minimum at 4.94Å is obviously related to the depletion of the Br-Br correlation, expected at 4.69Å. The discrepancy might be due to interference with methanol cage peak at 3.63Å which tend to shift the Br-Br correlation to larger r. In the discussion below we will comment further on these discrepancies.

In both cases a detailed analysis should include the solute-solute, solute-solvent, and the solvent hydrodynamics and in the following sections we will develop a model that accounts for these contributions.

5.3.4 Global fitting of the diffraction curves

We modelled the experimental difference signals according to section 5.1. This was done for HgI_2 and $HgBr_2$, using a program written by Marco Cammarata [9], in which the model is least-squares fit against the experimental data using the minimisation package MINUIT from CERN [9, 71]. In order to decrease the number of free parameters and to have a self-consistent model, the changes in population are linked by system of linear differential equations that describes the chemical process. They can deal with unimolecular reaction, such as the decay of an excited state to a different state or the breakage of molecule into smaller molecules, or bimolecular reactions, where two molecules meet and form a bigger one. Clearly, during these processes the number of every atomic species is conserved, which limits the number of possible reactions. Energetic/chemical considerations can be used as well to constrain the free parameters. We will now write the system of linear equation for HgI_2 and $HgBr_2$, the systems in which we applied this global analysis. Expressing, to be general, the halogen atom as X, considering $t > t_{diss}$ (i.e. t>1-10ps) the equations describing the population changes can be written as

$$\begin{aligned}
\frac{\partial[HgX_2]}{\partial t} &= D_1[HgX][X] \\
\frac{\partial[HgX]}{\partial t} &= -D_1[HgX][X] \\
\frac{\partial[X_2]}{\partial t} &= D_2[X]^2 \\
\frac{\partial[X]}{\partial t} &= -D_1[HgX][X] - 2D_2[X]^2
\end{aligned} \tag{5.8}$$

Initial conditions to the system are:

$$\begin{aligned}
[HgX]_0 &= f \\
[X]_0 &= f \\
[HgX_2]_0 &= \left(f_{(HgX_2)_{b.e.}} - f\right) \\
\Delta\rho &= 0 \\
\Delta T &= \Delta T_0(f)
\end{aligned} \tag{5.9}$$

where D_1 (in $[1/(\mathrm{s}\cdot\mathrm{mM})]$ the bimolecular recombination coefficient for the channel $HgX + X \rightarrow HgX_2$, and D_2 for the reaction channel $X + X \rightarrow X_2$. f is the concentration of dissociated HgX_2 molecules (excluding the molecules recombined through vibrational cooling) and $f_{(HgX_2)_{b.e.}}$ the concentration of HgX_2 before the excitation. As we saw the response of the solvent is then linked to the populations of the species as a function of time; the geminate recombination that we cannot see with our experimental time resolution is included in the equation of the heat released as a function of time, where the rate constant for the vibrational cooling is also taken into account (Eq.5.6). In this way we are only considering as putative channels and transient species the formation of HgX and X and the bimolecular recombination of dissociated X atoms in bimolecular X_2 molecules, neglecting, only for the moment, the possible formation of the isomer state $HgX - X$ that we considered in the general presentation of the plausible photo-recombination channels.

By integrating these equations, linked to the thermodynamical variables through Eq.5.6, (using for the integration the above mentioned program written by Marco Cammarata [9] and updated for HgI_2 by Jae Hyuk Lee at KAIST) we have a parametrised model for $\Delta S(Q,\tau)$ which we can fit to the experimental data and hence determine the rate constants and the laser beam size [9, 71]. The details and results concerning the MD simulations performed on these two systems to obtain the fundamental vectors to build up a theoretical $\Delta S(Q)$ according to Eq.5.2 were described in section 3.4.

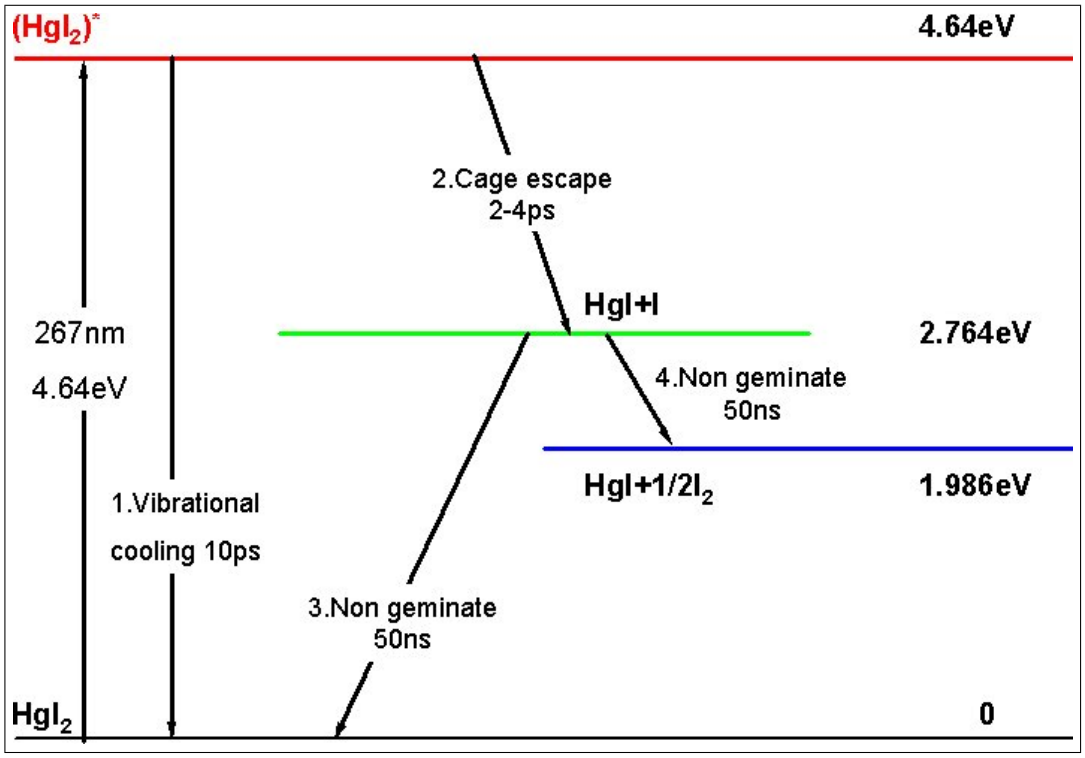

Figure 5.16: Schematic diagram of the reaction dynamics of photo-excited HgI_2 in CH_3OH.

5.3.5 Structural Dynamics and Energy dissipation

The two diagrams in Fig.5.16 and 5.17 summarise the energies and time scales for the dominant pathways of the reaction dynamics of HgI_2 and $HgBr_2$ in CH_3OH.

From the global fit we can determine populations and the rate constants of all the chemical species. For the time scales of the processes involved we know that after 100ps, the concentration of (effectively) dissociated species is at the highest level as the fast geminate recombination process is over in less than 10ps. As a result the dominant species after 100ps are the photo-products HgX and X. From the resulting plots (Fig.5.18, 5.19), we can immediately conclude that the reaction dynamics for the two molecular systems is exactly the same: after the two-body dissociation which is completed in less than 10ps ([81, 82]), we observe the appearance of HgX radicals that recombine non geminately with X atoms that have escaped from another solvent cages to form new parents molecules HgX_2. About 71% of the transient radicals HgI present in solution at 100ps after the two-body dissociation, recombines with an I atom to reform the parent molecule HgI_2, while $\sim 89\%$ of the dissociated $HgBr$ recombines with Br atoms reforming the parent molecule. On the other hand, 29% of the iodine atoms and 11% of the bromine atoms combine to form respectively I_2 and Br_2. From the global fitting we determine a bimolecular rate constant of $1.0 \times 10^{11} M^{-1}s^{-1}$ for the nongeminate formation of HgI_2, value that we assume as fix parameter in the analysis procedure of $HgBr_2$ data. The rate constant for bimolecular iodine-iodine recombination is found to be of the order of $10^{10} M^{-1}s^{-1}$ while the bromine atoms combine to form Br_2 molecules with a rate constant of the order of $\times 10^{11} M^{-1}s^{-1}$.

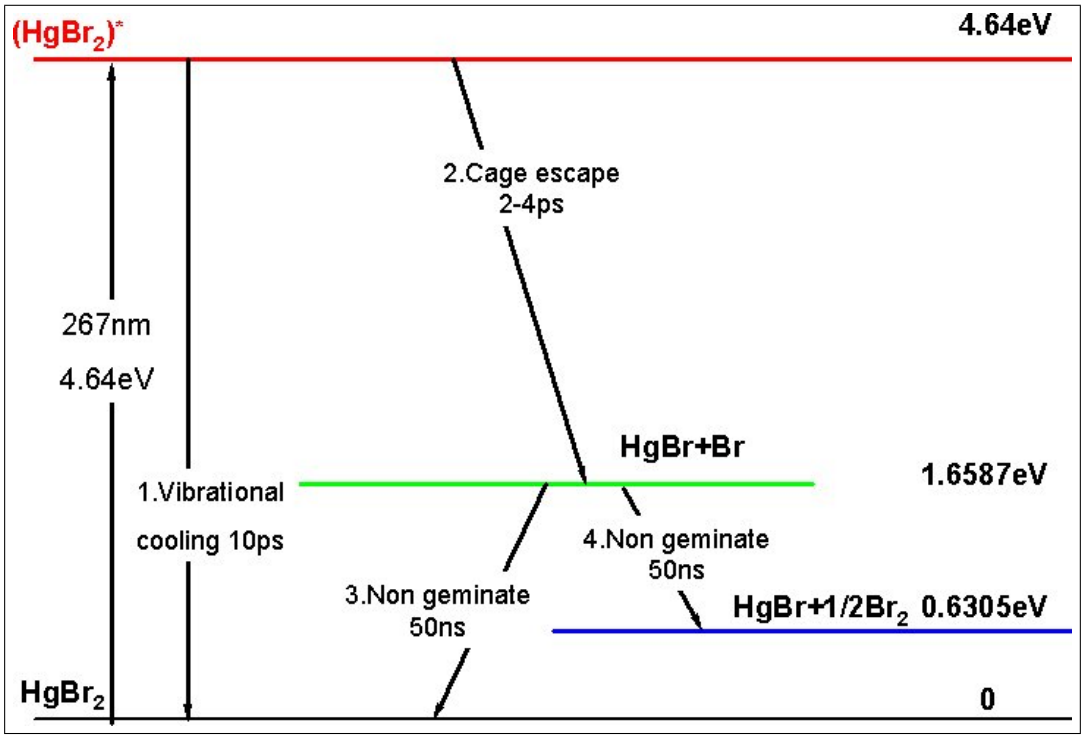

Figure 5.17: Schematic diagram of the reaction dynamics of photo-excited $HgBr_2$ in CH_3OH.

We can compare these values to the time constant available in the literature: for the nongeminate recombination of I_2 in CCl_4 solution a value of the order of $10^{10}M^{-1}s^{-1}$ [83] was measured. Moreover it can be noticed how the HgX_2 forms faster than X_2, in both cases, implying that the activation energy for the formation of HgX_2 is lower than that for X_2. As result of the global fitting we get as well the evolution of temperature and pressure as a function of the time during the reaction.

In Fig.5.18, 5.19, we show the temperature evolution as a function of time, and it is worth to stress the duality between the decay in the excited state population and the rise in temperature. At 1μs we observe the density decrease after the thermal expansion. In the case of HgI_2 the density of the solvent decreased, at 1μs by $0.83kg/m^3$, which corresponds to a temperature change of 0.71K, for $HgBr_2$ the density decreased by $0.47kg/m^3$ with a temperature rise of 0.41K. In the plots the baseline stems from the geminate ultrafast reaction pathway. Indeed, even if we can not observe this very fast process, we can detect it though its signature from the temperature rise in the solvent and thus estimate the percentage of the excited molecule that actually dissociate.

Having determined the concentration of the solutes (HgX_2, HgX, X_2) and the DFT energies E_k shown in table 5.3 we can now calculate the energy transferred to the solvent, ΔE at the end of the reaction, at $\simeq 1\mu$s as

$$\Delta E = E_0 - \sum_k f_k E_k,$$

where E_0 is the laser energy, which in both the experiment, is $E_0 = 4.64eV$.

Transitions and Energies E_k
$HgI + I \rightarrow HgI_2$ + 2.764eV
$I + I \rightarrow I_2$ + 1.556eV
$HgBr + Br \rightarrow HgBr_2$ + 1.397eV
$Br + Br \rightarrow Br_2$ + 2.0563eV

Table 5.3: Energies calculated from density functional theory for the chemical transitions.

The energy transferred to $1cm^3$ of sample will be ΔE multiplied by the number density n_{HgX_2} of the excited solute molecules, given by the observed concentration of HgX and X species at 100ps (Fig.5.18, 5.19).

$$\Delta E/cm^3 = \Delta E \times n_{HgX_2}$$

and from it we calculate the temperature rise of $1cm^3$ as

$$\Delta T = \frac{\Delta E}{C_P \rho}$$

(where for methanol $\rho_{CH3OH} = 791kg/m^3$ and $C_P = 2.531J/K/g$) finding $\Delta T_{HgI_2} =$ 0.22K and $\Delta T_{HgBr_2} = 0.075$K.

As we said we experimentally observe a $\Delta T_{HgI_2} = 0.71$K and $\Delta T_{HgBr_2} = 0.41$K from the amplitude of $\Delta S(Q, 1\mu s)$. This discrepancy indicates that a large fraction of excited molecules recombine geminately: we estimate that 66% of the initial HgI_2^* and 81% of the initial $HgBr_2^*$ molecules decay into the ground state via in cage vibrational cooling and release their energy to the solvent by means of collision on the 10ps time scale [84] whereas the remaining 34% and 19% dissociates respectively into HgI + I and HgBr + Br. If the experiment could be done with 1ps resolution, the early $\Delta S(Q)$ curves between 1-10ps would probably film the contraction of the Hg-I bond in real time. With our 100ps resolution, we only observe the afterglow of excess of heat from this ultrafast process. In the 10mM concentration of HgI_2 we find that 34% of the molecules are excited by the laser pulse, while the only $\sim 7\%$ are excited in the 25mM $HgBr_2$ solution. Amongst these excited molecules in the two cases, from energetic consideration we estimate that 66% of the excited HgI_2 molecules and 81% of the excited $HgBr_2$ molecules recombinate via fast geminate recombination, while 34% for HgI_2 and 19% for $HgBr_2$ actually undergo to dissociation. We discussed the dynamics of the dissociated species as a function of the time shown in Fig.5.18, 5.19. Amongst the dissociated molecules, $\sim 71\%$ of the transient radicals HgI recombines with an I atom to reform the parent molecule HgI_2 and 29% of iodine atoms recombine together forming I_2 molecules. $\sim 89\%$ of the dissociated $HgBr$ recombines with Br atoms reforming the parent molecule, while 11% of the dissociated bromine atoms combine to form respectively Br_2.

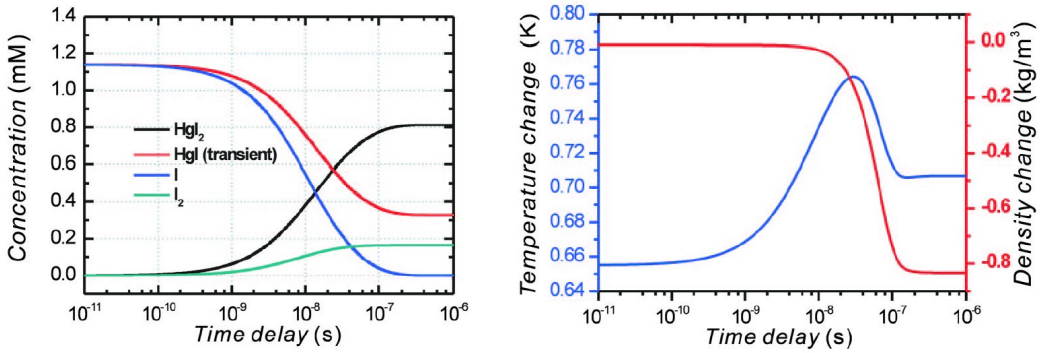

Figure 5.18: On the left, the population changes of the transient molecular species as a function of time after photodissociation of HgI_2 in methanol. On the right, the change in the solvent density (red) and temperature (blue) during the $HgI + I$ recombination process.

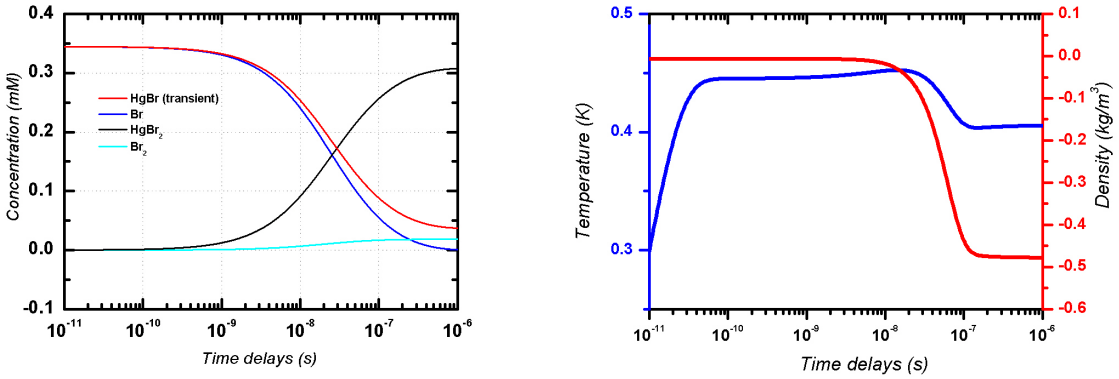

Figure 5.19: On the left, the population changes of the transient molecular species as a function of time after photodissociation of $HgBr_2$ in methanol. On the right, the change in the solvent density (red) and temperature (blue) during the $HgBr + Br$ recombination process.

	Concentration	**Excited molecules**
HgI_2	10mM	33%
$HgBr_2$	25mM	7%
	$\Delta\rho(1\mu s)$	$\Delta T(1\mu s)$
HgI_2	$0.83kg/m^3$	0.71K
$HgBr_2$	$0.47kg/m^3$	0.41K
	Dissociated molecules (amongst the excited)	**Recombination via vibrational cooling (amongst the excited)**
HgI_2	34%	66%
$HgBr_2$	19%	81%
	Recombination HgX+X (amongst the dissociated)	**Recombination X+X (amongst the dissociated)**
HgI_2	71%	29%
$HgBr_2$	89%	11%
	Recombination coefficients HgX+X	**Recombination coefficients X+X**
HgI_2	$1 \times 10^{11}(M^{-1}s^{-1})$	$1 \times 10^{10}(M^{-1}s^{-1})$
$HgBr_2$	$1 \times 10^{11}(M^{-1}s^{-1})$	$1 \times 10^{11}(M^{-1}s^{-1})$

Table 5.4: Summary of the results describing the recombination dynamics of HgI_2 and $HgBr_2$ in CH_3OH. Note the agreement between the value found from the fit for the recombination coefficients of the I+I channel and the value in [83]. The result found for the bimolecular rate constant of the HgI+I recombination was used as fixed parameter in the $HgBr_2$ study.

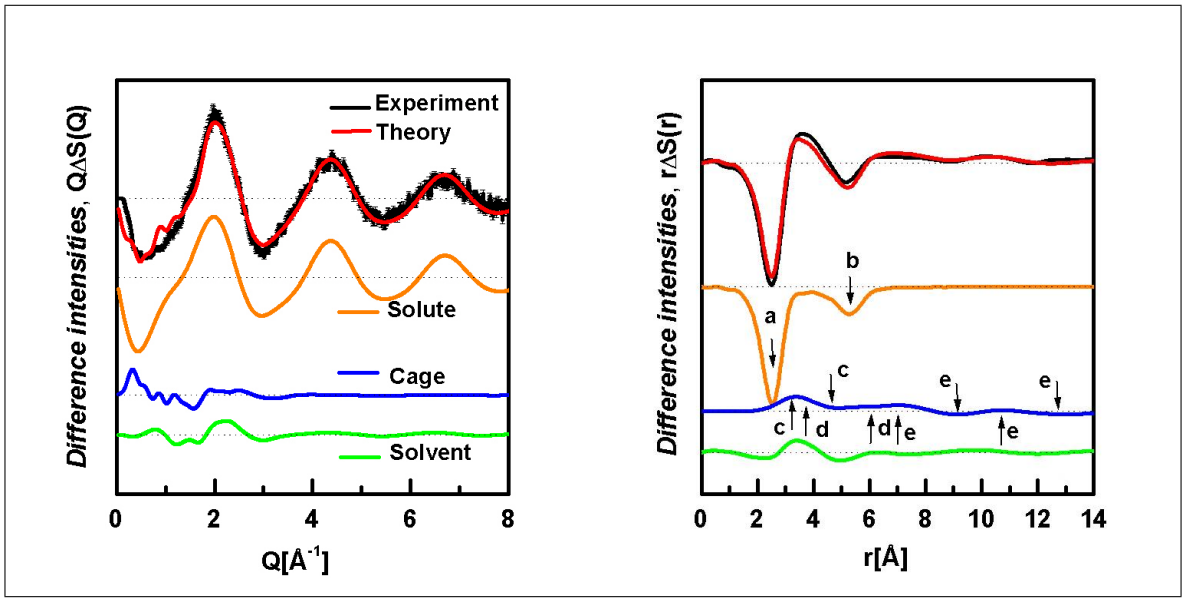

Figure 5.20: Contributions from the solute-only, the solute-solvent (cage) and the solvent-solvent correlation to the difference intensity for HgI_2 in methanol at 100ps and the associated radial distribution functions. The curve fitting is based on MD and experimental solvent differentials, and includes thus intra and intermolecular contributions from the solutes and the solvent. The experimental curves are black and theoretical ones are red. The components are also shown: solute without cage (orange), cage effects (blue), and solvent contribution (green). The assignments of the major peaks and valleys in real space are given as follows: (a) Hg-I of HgI_2, (b) I..I of HgI_2, (c) Hg..solvent, (d) I..$O_{solvent}$, (e) I..solvent.

5.3.6 Decomposition of data into structural elements

Now we will examine the individual components in the theoretical curves: the solvent only, the change in the solvation cage, and the hydrodynamic response of the solvent.

In Fig.5.20, 5.21, we show this decomposition of the model curve for 100ps. Because of the heavy Hg and I/Br atoms in the solute, solute dynamics dominate over those from the cage and the solvent. However, the contributions from the cage and the solvent are significant in the low Q region. From the real space curve $r\Delta S(r)$ in Fig.5.20 a more direct structural picture can be obtained. In HgI_2, the negative peak at $\approx$ 2.65Å is mainly from the depletion of the Hg-I bond in HgI_2 and formation of a new Hg-I bond in the transient at 2.770Å, while the second negative peak near 5.30Å is attributed to the I..I distance in the parent molecules. The maximum observed at $\approx$3.50Å is explained by the elongated bondlength in the Hg-I radical and the new liquid packing around HgI and I (cage effect).

First of all cage escape creates a vacuum that, as we could say, nature does not like, which is then filled up by solvent molecules, which brings the solvent closer to the solutes.

As we already pointed out the quality of both data and fits are best for HgI_2 which could be due to its stronger diffraction signal as compared to $HgBr_2$. Consequently, even if we can identify the reaction dynamics of the main recombination pathway in the recombination process, the attribution of bond distances and correlations from the

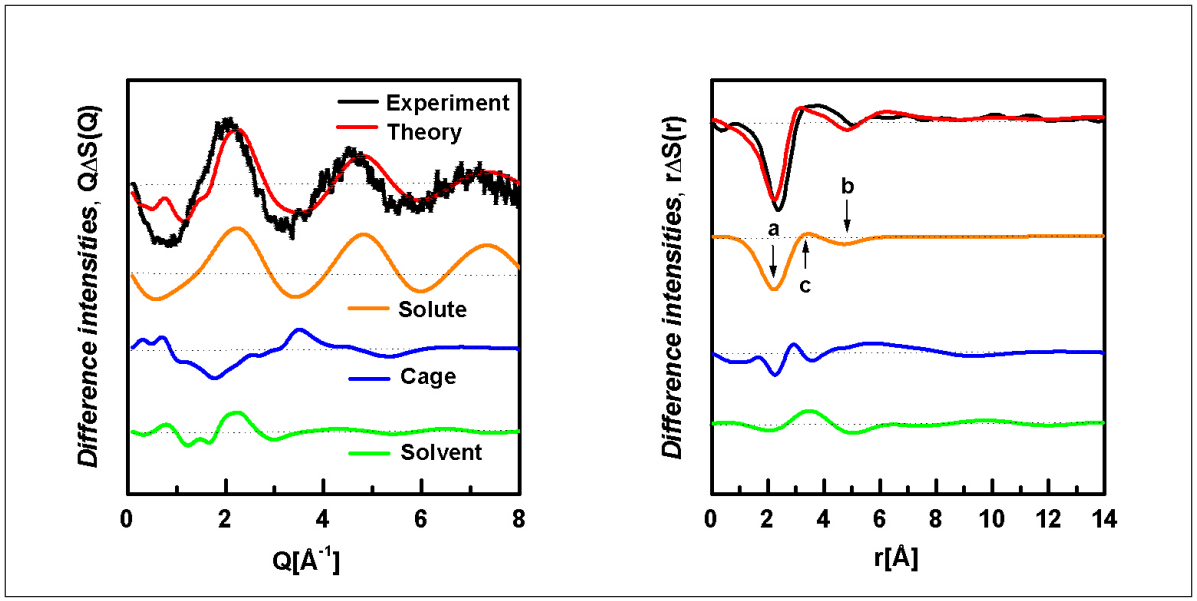

Figure 5.21: Contributions from the solute-only, the solute-solvent (cage) and the solvent-solvent correlation to the difference intensities for $HgBr_2$ in methanol at 100ps and the associated radial distribution functions. The curve fitting is based on MD and experimental solvent differentials, and includes thus intra and intermolecular contributions from solutes and the solvent. The experimental curves are black and the theoretical ones are red. The components are also shown: solute without cage (orange), cage effects (blue), and solvent contribution (green).

radial curves is less convincing. Nevertheless in the limits discussed in section 5.3.3 we attribute the minimum position at 2.28Å, to the breakage of the Hg-Br bond and the second minimum at 4.94Å to disappearance of the Br-Br correlation within the $HgBr_2$ molecule. As in HgI_2, the positive peak from the cage structure tells us that the solvent comes closer to the average excited atom.

However the quality of the cage simulation is probably not good enough due to insufficient statistics in the MD simulations, to draw conclusions about the misfit in that region.

In both cases the observed correlations in the bulk solvent are due to the structural change associated with isochoric heating. At atomic level the atom-atom correlations are broadened, without a change in their centre of mass. The peaks in the excited state $g_{\alpha,\beta}$ functions decrease which leads to minima in the difference functions at those points in r-space.

5.3.7 HgI_2: determination of the primary reaction pathway

Before performing the global fit analysis for all time delays we considered all plausible dissociation pathways in order to let the fits select the actual ones. The $Q\Delta S(Q,\tau)$ curves at early time delays (100ps, 300ps, and 1ns) were fitted to a series of candidate pathways using MD based diffraction curves for the various solutes. The diffraction curves were obtained from MD calculation with the solutes immersed in 512 solvent molecules (see Chapter3). The solutes geometries were obtained from density functional

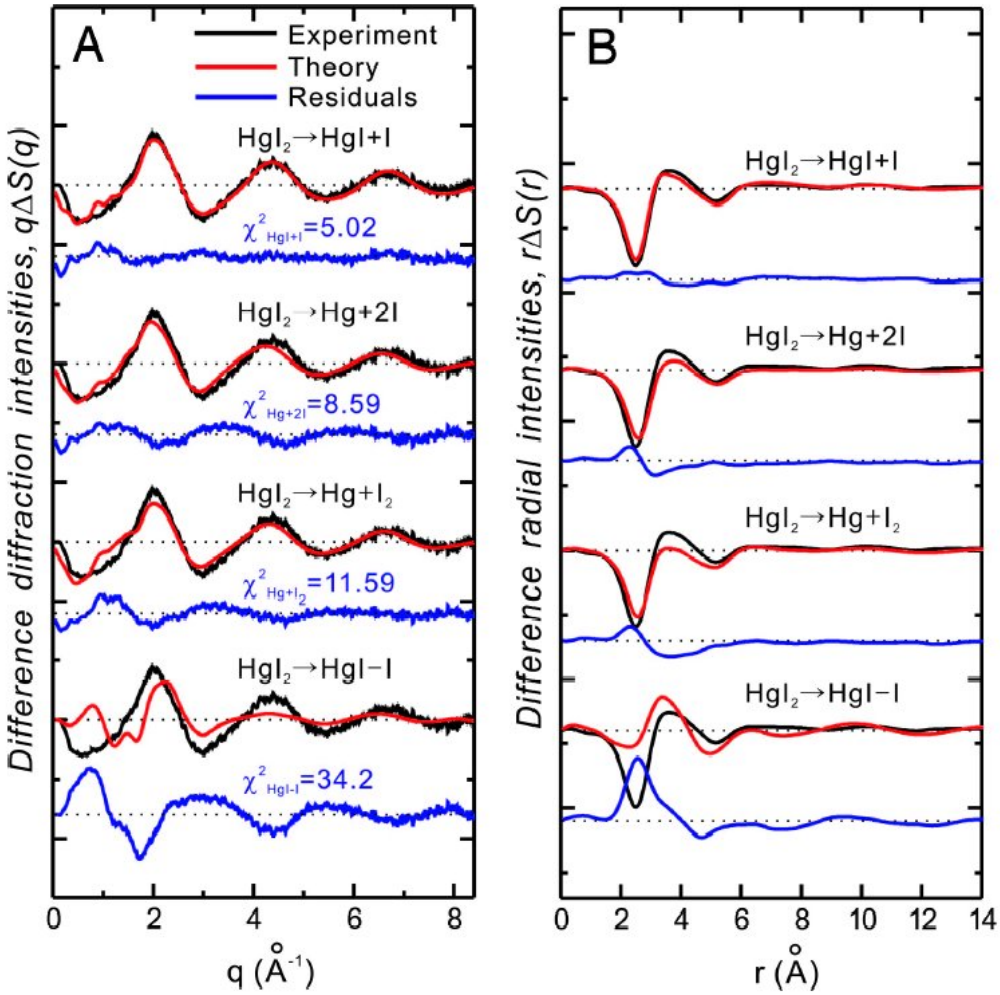

Figure 5.22: Determination of the photodissociation pathway of HgI_2 in methanol. Theoretical (red) and experimental (black) difference intensities for candidate channels in Q and in real space. In blue the residues, and the χ^2 values for each channel from the global fitting at 100ps are also indicated. The best fit is obtained from the dissociation channel $HgI_2 \rightarrow HgI + I$.

theory-optimised geometries and relative energies, according to Table 3.3.

Because three-body dissociation is energetically impossible with one-photon excitation at 267nm (448.2 kJ/mol), it is of interest to check whether our analysis can exclude this channel.

In Fig.5.22 we show the comparison between $Q\Delta S(Q,\tau)$ at 100ps and the corresponding fit results for various trial pathways. The residuals between the experimental data and the fits along with χ^2_{total} values are displayed for each pathway. The poor agreement between experiment and theory for the isomer channel precludes this pathway.

The fit for the $HgI_2 \rightarrow HgI + I$ channel perfectly matches the experimental data over the whole Q range as compared with other reaction channels. The fits for $HgI_2 \rightarrow Hg + 2I$ and $HgI_2 \rightarrow Hg + I_2$ in the high Q region have a rather good figure of merit, but the fit is less good than the two-body dissociation channel. In fact, the $Q\Delta S(Q)$

curves from the solute-only contributions show very small differences at high Q [21]. In the fits for these channels, the residual errors are greater around the positive peak near 2Å^{-1} and around the negative peak at 3Å^{-1} than the fit for $HgI_2 \rightarrow Hg + 2I$ channel. In Fig. 5.20, one can see that the contribution from the solvent to these peaks is non negligible. Thus, the apparent disagreements of the peak at 2 and 3 Å^{-1} for $HgI_2 \rightarrow Hg + 2I$ and $HgI_2 \rightarrow Hg + I_2$ channels indicate that the solvent contribution in these channels is inconsistent with the associated transfer of energy to the solvent. These results establish that the $HgI_2 \rightarrow HgI + I$ reaction is the dominant pathway at 100ps after 267nm photodissociation of HgI_2 in methanol and that the solvent contribution helps to discriminate between candidate channels when the energetics is included. More importantly, when a mixture of $HgI_2 \rightarrow HgI + I$, $HgI_2 \rightarrow Hg + 2I$, $HgI_2 \rightarrow Hg + I_2$, was fitted together against the $Q\Delta S(Q,\tau)$, the contributions of $HgI_2 \rightarrow Hg + 2I$ and $HgI_2 \rightarrow Hg + I_2$ converged to zero. We also considered the contribution of parent molecule with bent geometry from previous studies [85], which deteriorated the fits being the distance between I atoms in the bent structure (5.00 Å) slightly smaller than in the linear geometry (5.30 Å). This finding illustrates the structural sensitivity of the TRXD technique.

5.4 Comparisons and limits of the $HgBr_2$ experiment.

The nice and complete results obtained in the study of HgI_2 in CH_3OH [32] reported in this section drove us naturally towards the investigation of a similar system as $HgBr_2$, with only one atomic substitution. For both data sets, the data collection and following data analysis were done in the same way to facilitate comparisons. The photodissociation mechanism was assumed to be the same, apart from the different DFT energy levels. The dominant recombination pathway was found to be two body dissociation, as confirmed by the quality of the fits in the high angle region using simple Debye gas-phase transitions. As we noticed though the global fits were of very different quality: why are the HgI_2 model so much better than the $HgBr_2$? Is the molecular structure of $HgBr_2$ not described correctly by DFT in methanol? Is the Hg-Br radical in an unexpected electronic state? Does it react with the solvent? We have not been able to answer these questions in this work.

The lower quality of the $HgBr_2$ data is due, in part, to fewer CCD images that were collected, 30 repetitions for $HgBr_2$ vs 60 for HgI_2 for each time delay. In addition we suspect that some instability in the liquid jet set-up is responsible for having more outliers most likely due to the open jet nozzle getting dirty.

First of all it is natural to interrogate ourselves about the possibility of having additional transient species in the solution beyond the simple two-body model, with anomalous curve shapes: this hypothesis could be excluded after inspection of Fig.5.23. The absorbance, indeed, at the chosen wavelength, seems to be quite negligible for Br_2 compared to the parent molecule; making us exclude the hypothesis of having excited formed Br_2 and create possible additional chemistry in the studied solution.

Secondly, in the case of $HgBr_2$ we gained a much lower excitation efficiency, without observing during the experiment any significant drop in the laser power.

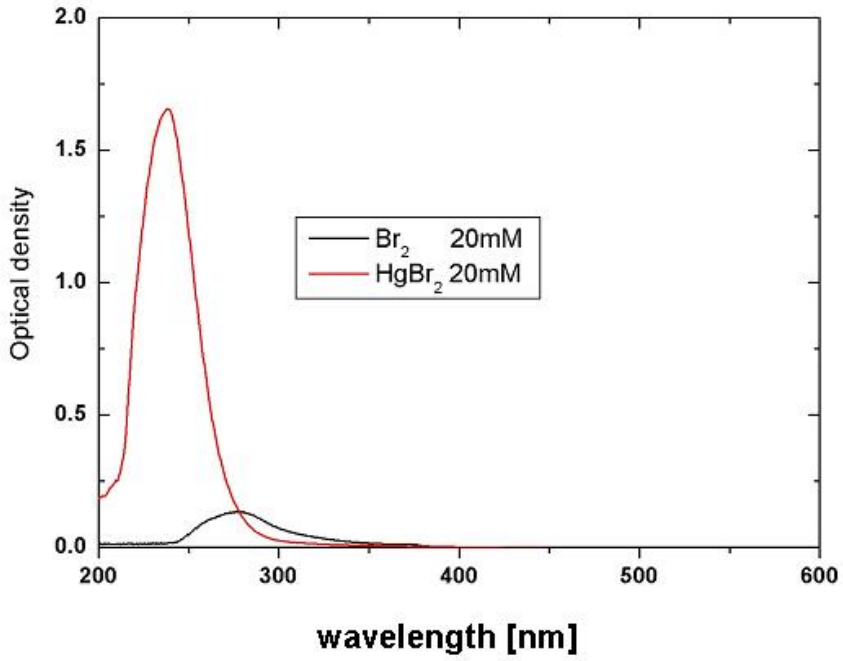

Figure 5.23: Comparison between the measured absorption spectrum of $HgBr_2$ and Br_2 in methanol.

A difference in the two experiments was the determination of the working concentration. Indeed, as we explained in section 5.3.1, in the case of HgI_2 we determined it experimentally looking at the best observed signal with a systematic concentration titration. For the $HgBr_2$, starting from the comparison with the HgI_2 we determined a "safe" range of concentration in which the high dilution limit was valid and the solute-solute correlations could be considered negligible, but then in this range we chose not to work at the highest concentration. Seemingly, it would have been important to use a higher concentration such to get a better S/N, according also to what we showed in section 2.4.2. This reason may explain the lowest quality of the $HgBr_2$ data compared to the HgI_2 ones.

Concerning the fits, the worse quality in the early time points is definitely to be attributed to the uncertainty of the bondlengths used in the model. Indeed, as we already said, this bondlength ranges widely from 2.378Å to 2.44Å. Even a slightly bent geometry was tried in a first high angle analysis but lead to poor fits of the oscillations.

New DFT calculations were performed by Ihee's group at Kaist at the time of writing this thesis. They predict linear geometries with a bondlength of 2.506Å for Hg-Br bond in $HgBr_2$ and 2.621Å for the Hg-Br bond in $HgBr$. Hopefully, together with new experiments with higher signal to noise ratio, the $HgBr_2$ model will undoubtedly improve.

Conclusions

In these pages a summary of the accomplished results is given. From the presented studies concerning Br_2, HgI_2, and $HgBr_2$ we showed how it is possible, by means of Time Resolved X-ray Diffraction, to achieve the goals we presented in the Introduction of this work, in the studies of the atomic motions of small molecules in solution during a photoinduced chemical reactions. Outlook towards possibilities for increasing the time resolution of the experiments and for better disentangling and understanding the different contributions present in the experimental signals are then briefly discussed.

Conclusion

La conclusion résume d'abord les résultats accomplis. Grâce aux résultats obtenues sur les solution de Br_2, HgI_2, et $HgBr_2$, nous avons démontré que la technique de la diffraction de rayons-X résolue dans le temps a permis d'apporter des réponses aux interrogations présentées dans l'introduction de ce travail dans l'étude des mouvements atomiques des molécules dissolues au cours d'une réaction chimique. Quelques perspectives y sont également présentées dans le but d'améliorer la résolution temporelle de ces expériences et d'améliorer la compréhension des différentes contributions aux signaux expérimentaux.

Conclusions

During this project we pursued the challenging aim of the observation of transient molecular structures, atomic motions and rearrangements of photo-excited molecules in liquid phase through Time Resolved X-ray Diffraction. The achieved results concerning Br_2, HgI_2, and $HgBr_2$ show how it is possible, by means of this technique, to

- identify which reactions take place and discriminate between possible recombination channels;
- reconstruct the comprehensive reaction dynamics of molecules in solution spanning from picoseconds up to microseconds;
- achieve information on the time scales of the different recombination or relaxation pathways;
- follow in time the evolution of the transient species as well as of the solvent thermodynamics.

In Chapter 1 we showed (Fig1.3) the improvements in the quality of the data since 2000, obtained thanks to the polychromatic beam now available on ID09B. This allowed the clearer experimental observation of the studied processes and led to a more established data reduction and analysis procedure. The results achieved bring to the possibility of studying more complicated chemical reactions during which several and more complex structural transients can be observed, as for instance molecules with important biological interests. Clearly, in reactions with more pathways and a higher number of unstable molecular transients, faster time scales could be involved: for these studies a higher time resolution will be required. During this work we continuously stressed the role played by the solvent in the reaction dynamics. We faced the difficulty of disentangling the different contributions in the diffraction signal and separate the diffraction signal coming from the photoproducts and the (induced) changes in the solvent. But there, the complexity innate in the non-selectivity of the diffraction technique discloses all its richness: the diffraction patterns revealed not only the composition and structure of the photoproducts but they also allow us to observe the liquid cages and the solvent response to the heating during the development of the reactions. Nevertheless, in order to study more complex reactions, or for example in order to study organic photo-systems with lower solvent contrast, it is thus crucial also to find the most accurate method of disentangling the different contributions included in the diffraction signals.

We want to discuss here how it is possible to proceed in these studies, increasing the time resolution, subtracting the heating of the solvent and resolving the cage structure from the naked solute.

Time slicing: towards faster processes

As we said, the temporal length of the synchrotron X-ray pulse limits our time resolution to $\simeq$ 100ps. We want to give here a demonstration of how a higher time resolution can be reached with the pump and probe set-up used and discussed in this work. In the Br_2 in CCl_4 experiment presented in this thesis, indeed, we collected data for shorter time delays, starting from 25ps, through what we call "time slicing" technique, which consists simply of setting the timing between the X-ray and laser pulse such that the laser pulse is placed inside the X-ray pulse, as schematically shown in Fig.5.24.

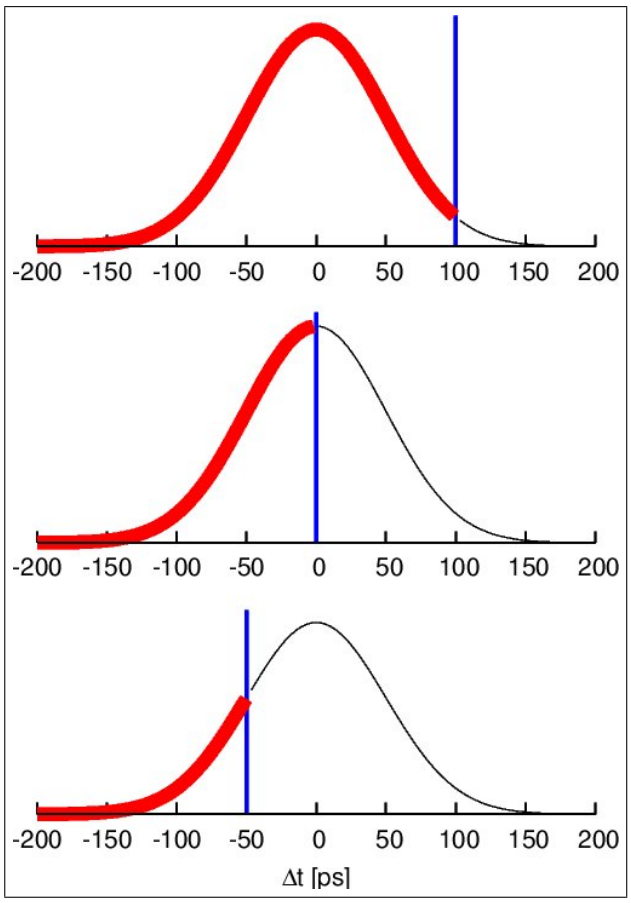

Figure 5.24: "Time slicing": only the X-ray photons coming after (red line) the laser pulse (blue line) will probe excited sample, contributing to the diffraction signal, while the others (in black) will see only unexcited sample, contributing only to the noise.

In fact in the 25ps and 50ps time delays, the (co-linear) laser pulse splits the X-ray pulse temporally in two parts. The leading edge of the X-ray pulse will see the unexcited sample whereas the trailing edge will see the excited sample with a truncated X-ray pulse. Note that the excited state is recorded with a weaker X-ray pulse which reduces

the S/N ratio and hence the utility of the time slicing. Nevertheless the data in Fig.5.25 we show how the technique can be used to get a first glimpse of sub 100ps dynamics. Indeed, we observe clearly already at 25ps structural features in the difference signal. In order to study faster phenomena, such as the breakage of a molecule and its fast

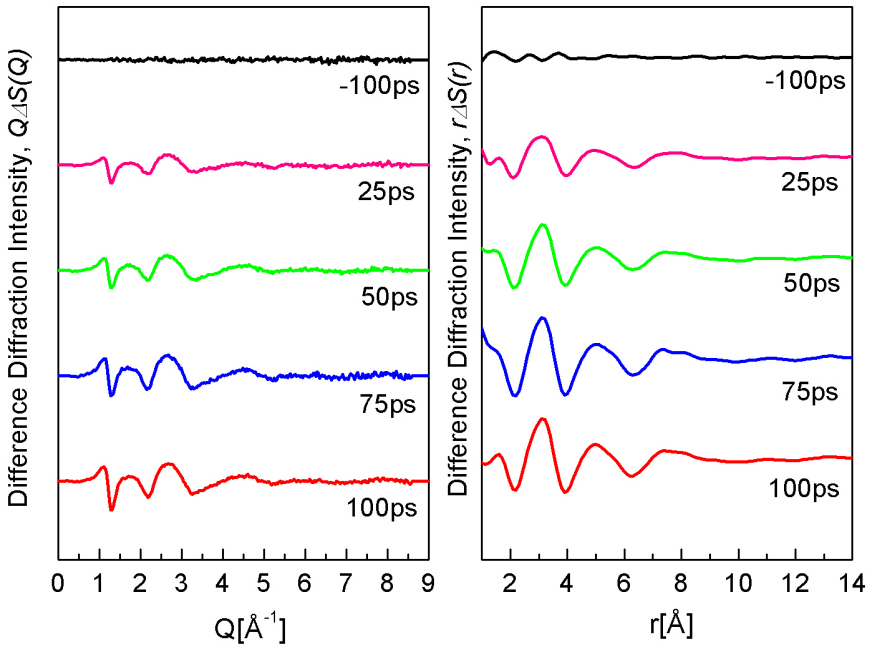

Figure 5.25: $\Delta S(Q,\tau)$ and $\Delta S[r,\tau]$ of Br_2 in CCl_4 collected through the time slicing technique. We are able to observe difference features clearly emerging at 25ps.

recombination, a major future goal would be to improve even more this temporal resolution. Indeed, as we saw in this work, with our time resolution we can follow in time the products of a chemical reaction and the development of the reaction itself, while with a higher resolution also the beginning of the reaction could be visualised. Even if this will not be possible with a synchrotron, the future sources, such as the free electron laser and laser-produced X-rays promise a time resolution of 100fs, opening possibly new investigations in the the time window of bond breaking phenomena and molecular vibrations.

Disentanglement of the solvent heating and cage contributions in the diffraction signal: towards the naked solute structure

In Chapter 4 and 5, we showed the experimental solvent differentials measured for CH_3OH inducing ultrafast impulsive heating using NIR radiation and the CCl_4 differentials obtained in response of heating induced through multiphoton excitation. We demonstrated how these experimental curves can be used to model the induced heating from the solute rearrangements during a photoinduced chemical reaction (Fig.4.17,

Fig.5.8). In principle, using these experimental differentials, it could be possible to directly subtract the solvent contribution off from the solution data and directly deduce the structure of the caged solutes during the reaction. In fig.5.26 we can see the differences between the 200ps difference maps of the pure solvent and of a solution of I_2 in CCl_4, which are the fingerprint of the presence of the solute.

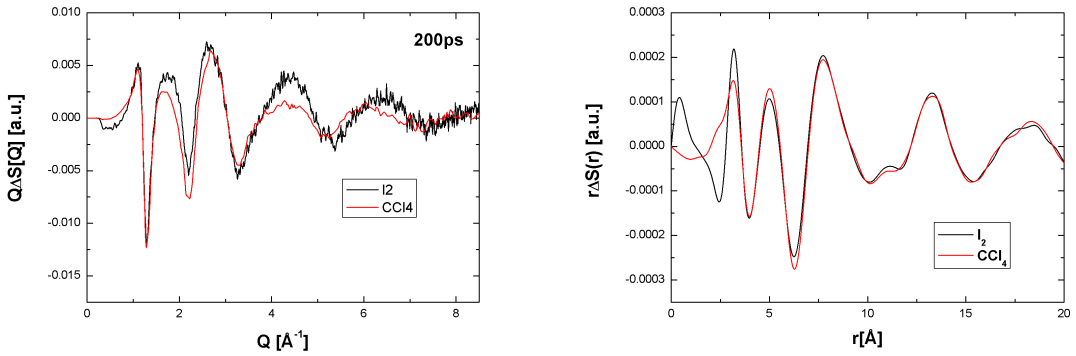

Figure 5.26: Comparison between 200ps difference maps of pure CCl_4 and a solution of I_2 in CCl_4.

This first comparison shows that it is now experimentally possible to separate very accurately the contribution from the photoproducts and the (induced) change in solvent temperature and experimentally obtaining the structure of the caged solutes during the reaction, undressing the photoproduct from the bulk. Thanks to the wide tuneability of the femto-second laser it is also possible to think to these experiments even in a more elegant way, i.e. exciting only the solute or only the solvent in the same solution only changing the laser wavelength in two different experiments performed on the same sample.

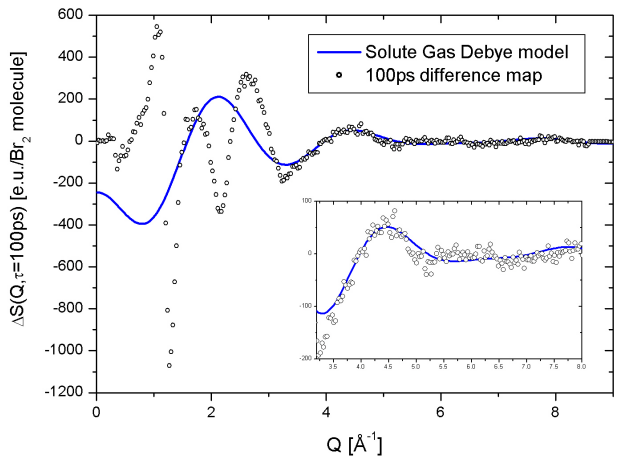

Figure 5.27: Comparison between the experimental $\Delta S(Q, 100ps)$ and the Debye molecular gas-phase transition. We already referred to the Q>4Å^{-1} region as "molecular gas-phase region", where the solvent and the cage contributions are very small and the naked solute structure dominates.

Once the solvent heating is subtracted, the cage contribution (I-Cl, C-Cl correlations) is nevertheless still present in the signal. Higher Q data could help in reducing this term. Indeed, at high Q the cage contribution is very low as we can see in Fig.5.27. With this aim, in order to extend the Q-range multilayer optics are being studied and developed on ID09B, which would allow to use higher energies selected from the higher harmonics of the undulator spectrum. High Q data represent a new goal, with new experimental challenges to deal with to obtain very good quality data, as, for instance, the lower diffuse intensity at high Q and the higher Compton scattering contribution.

The open problems we stressed, together with the perspectives mentioned above to possibly solve them, give an insight into the future possibilities that the technique offers in order to push beyond the present limitations to get more complete and new information and move onto new fields of investigation. With the results shown in this work we gave a contribution to demonstrate the power of the Time Resolved X-ray Diffraction technique in visualising atomic motions and following in time photo-induced chemical reaction in solution.

Bibliography

[1] A. Plech, M. Wulff, S. Bratos, F. Mirloup, R. Vuilleumier, F. Schotte and P.A. Anfinrud, *Phys. Rev. Lett.* **92**, 125505, (2004).

[2] D. A. Reis et al., *Phys. Rev. Lett.* **86**, 3072 (2001).

[3] A. Rousse et al., *Nature*, **410**, 65 (2001).

[4] S. Techert, F. Schotte, M. Wulff, *Phys. Rev. Lett.* **86**, 2030, (2001).

[5] F. Schotte, M. Lim, T. A. Jackson, A.V. Smirnov, J. Soman, J. Olson, G. N. Phillips, M. Wulff, P. A. Anfirud, *Science*, **300**, 1944, (2003).

[6] R. Neutze, R.Wouts, S. Techert, J. Davidsson, M. Kocsis, A. Kirrander, F. Schotte, M.Wulff, *Phys. Rev. Lett.* **87**, 195508 (2001).

[7] V. Srajer, T. Teng, T. Ursby, C. Pradervand, Z. Ren, S. Adachi, W. Schildkamp, and D. Bourgeois, *Science* **274**, 1726 (1996).

[8] F. Schotte, M. Lim, T. A. Jackson, A.V. Smirnov, J. Soman, J. Olson, G. N. Phillips, M. Wulff, and P. A. Anfirud, *Science* **300**, 1944 (2003).

[9] H. Ihee, M. Lorenc, T. K. Kim, Q.Y. Kong, M. Cammarata, J.H. Lee, S. Bratos, M. Wulff, *Science* **309**, 1223, (2005).

[10] T.J. Chuang, G.W. Hoffman, K.B. Eisenthal, *Chem. Phys. Lett.* **25**, 201, (1974).

[11] H. L. Harris, M. Berg, C. B. Harris, *J. Chem. Phys.* **84**, 788, (1986).

[12] N. Alan Abul-Haj, D. F. Kelley, *J. Chem. Phys.* **84**, 1335, (1986).

[13] D. F. Kelley, N. Alan Abul-Haj,D.J. Jang, *J. Chem. Phys.* **80**, 4105, (1984).

[14] L.H. MacDonald, R.L. Strong, *J. Phys. Chem.* **95**, 6940, (1991).

[15] R.L. Strong, *J. Am. Chem. Soc.* **87**, 3563, (1965).

[16] L. Nugent-Glanford, M. Scheer, D.A. Samuels, A.M. Mulhisen, E.R. Grant, X. Yang, V. Bierbaum, S. Leone, *Phys. Rev. Lett.* **87**, 193002, (2001).

[17] R. S. Mulliken, *J. Chem. Phys.* **55**, 288, (1971).

[18] R. Zhu, and J. M. Harris, *Chem. Phys. Lett.* **186**, 183, (1991).

[19] R. Zhu, and J. M. Harris, *J. Phys. Chem.* **97**, 6650, (1993).

[20] S. Bratos, F. Mirloup, R. Vuilleumier, M. Wulff, A. Plech, *Chem. Phys.* **304**, 245, (2004).

[21] A. Geis, M. Bouriau, A. Plech, F. Schotte, S. Techert, H.P. Trommsdorff, M. Wulff, D. Block, *Journal of Luminescence*, **94**, 493, (2001).

[22] R.O. Pierce, *Wied. Ann.* **6**, 597, (1879).

[23] M. Sandström , *Acta Chem. Scand.* **7**, (1978).

[24] J.H. Parkes, *Appl. Phys. Lett.* **31**, 192, (1977).

[25] E.J. Schimitschek, J.E. Celto, *Opt. Lett.*, **2**, 64, (1983).

[26] T. Baumert, S. Pedersen, A.H. Zewail, *J. Phys. Chem.* **97**, 12447, (1993).

[27] M. Dantus, R.M. Bowman, M. Gruebele, A.H. Zewail, *J. Phys. Chem.* **91**, 7437, (1989).

[28] D. Zhong, A.H. Zewail, *J. Phys. Chem. A*, **102**, 4031, (1998).

[29] N. Pugliano, A.Z. Szarka, S. Gnanakaran, M. Triechel, R.M. Hochstrasser, *J. Phys. Chem.* **103**, 6498, (1995).

[30] N. Pugliano, D.K. Palit, A.Z. Szarka, R.M. Hochstrasser, *J. Phys. Chem.* **99**, 7273, (1993).

[31] M. Volk, S. Gnanakaran, E. Gooding, Y. Kholodenko, N. Pugliano, R.M. Hochstrasser, *J. Phys. Chem. A*, **101**, 638, (1997).

[32] T.K. Kim, M. Lorenc, J.H. Lee, M. Lo Russo, J. Kim, M. Cammarata, Q.Y. Kong, S. Noel, A. Plech, M. Wulff, H. Ihee, *PNAS*, **103**, 9410, (2006).

[33] R.W. Wadt, *J. Chem. Phys.* **72**, 2469, (1980).

[34] J. Maya, *IEEE J. Quantum Electron*, **QE-14**, 464 (1978).

[35] J.A. Mc Garvey, N.H. Cheung, A.C. Erlandson, T.A. Cool, *J. Chem. Phys.* **74**, 5133, (1981).

[36] M. Lim, M.F. Wolford, P. Hamm, R. M. Hochstrasser, *Chem. Phys. Lett.* **290**, 355, (1998).

[37] G.A. Bowmaker, "*Spectroscopy of inorganic-based materials*", Wiley, New York, (1987).

[38] B.E. Warren, "*X-ray Diffraction*", Dover, New York (1969).

[39] J. Als-Nielsen, D. McMorrow, "*Element of Modern X-ray Physics*", Wiley, New York (2001).

[40] F. Hajdu *Acta Cryst.* **A28**, 250, (1971).

[41] G. Palinkas, *Acta Cryst.* **A29**, 10, (1973).

[42] http://www.esrf.eu

[43] J.P. Hansen, I.R. McDonald, "*Theory of Simple Liquid*", Academic Press, New York (1997).

[44] S. Bratos, F. Mirloup, R. Vuilleumier, M. Wulff, *J. Chem. Phys.*, **116**, 10605, (2002).

[45] A.H. Narten, H.A. Levy, *Science*, **165**, 447, (1969).

[46] M. Wulff, S. Bratos, A. Plech, R. Vuilleumier, F. Mirloup, M. Lorenc, Q.Y. Kong, H. Ihee, *J. Chem. Phys.* **124**, 034501, (2006).

[47] M. Cammarata, M. Lorenc, T.K. Kim, J.H. Lee, Q.Y. Kong, E. Pontecorvo, M. Lo Russo, G. Schirò, A. Cupane, M. Wulff, H.Ihee, *J. Chem. Phys.* **124**, 124504, (2006).

[48] A. Plech, R. Randler, A. Geis, M. Wulff, *J. Synchrotron Rad.* **9**, 287, (2002).

[49] F. Schotte, S. Techert, P. Anfinrud, V. Srajer, K. Moffat, M. Wulff, "*Third generation Hard X-ray Synchrotron Radiation Sources : Source Properties, Optics and Experimental Techniques*", Edited by Dennis M. Mills.

[50] A. Geis, M. Bouriau, A. Plech, F. Schotte, S. Techert, H.P. Trommsdroff, M. Wulff, D. Block, *J. Lumin. 94*, 493, (2001).

[51] M. Wulff, A. Plech, L. Eybert, R. Randler, F. Schotte, P.A. Anfinrud, *Faraday Discussion* **122**, 13, (2003).

[52] S. Mobilio, G. Vlaic, "*Conference Proceedings, Synchrotron Radiation: Methodologies and Applications*", Vol. 82, SIF, Bologna, 2003.

[53] L. Eybert, M. Wulff, W. Reichenbach, A. Plech, F. Schotte, E. Gagliardini, L. Zhang, O. Hignette, A. Rommeveaux and A. Freund. "*The toroidal mirror for single-pulse experiments on ID09B*", SPIE Vol. 4782, p 246-257 (2002).

[54] P. Allen, D. J. Tildesley, "*Computer Simulation of Liquids*", Clarendo Press, Oxford, (1989).

[55] K. Refson, *Moldy User's Manual*, (2004).

[56] W. Hoover, *Phys. Rev. A* **31**, 1965, (1985).

[57] F. Mirloup, "*Diffraction des rayons X résolue en temps. Dissociation et recombinaison de l'iode en solution*", Ph.D. thesis, unpublished, (2004).

[58] E.M. Duffy, D.L. Severance, W.L. Jorgensen, *J. Am. Chem. Soc.* **114**, 7535, (1992).

[59] D.R. Lide, H.V. Kehiaian: "*CRC Handbook of Thermophysical and Thermochemical Data*", CRD press (1994).

[60] M.J. Frisch, G.W. Trucks, *Gaussian 94*, P. PA, ed. Elsevier, (1995).

[61] J.B. Foresman, A. Frisch, "*Exploring Chemistry with Electronic Structure Methods*", Gaussian Inc., Pittsburgh PA, (1996).

[62] W.J. Hehre, L. Radom, P.v.R. Schleyer, J.A. Pople, "*Ab Initio Molecular Orbital Theory*", John Wiley & Sons, New York, (1986).

[63] A.D. Becke, *J. Chem. Phys.* **98**, 5648, (1993).

[64] M. Cammarata, M. Lorenc, T.K. Kim, J.H. Lee, Q.Y. Kong, E. Pontecorvo, M. Lo Russo, G. Schirò, A. Cupane, M. Wulff, H.Ihee, *J. Chem. Phys.*, **124**, 124504, (2006).

[65] P.R. Longaker, M.M. Litvak, *J. Appl. Phys.* **40**, 4033, (1969).

[66] M. Falk and E. Whalley, *J. Chem. Phys.* **34**, 1554, (1961).

[67] http://www.esrf.fr/computing/scientific/FIT2D/.

[68] J. Tellinghuisen, *J. Chem. Phys.*, **58**, 2821, (1973).

[69] F. Mirloup, R. Vuilleumier, S. Bratos and M. Wulff, "*Femtochemistry and Femtobiology*, Elsevier, Amsterdam, (2004).

[70] N. Alan Abul-Haj, D. F. Kelley, *Chem. Phys. Lett.* **119**, 182, (1985).

[71] CERN, Minuit; Function Minimization and Error Analysis, http://wwwasdoc.web.cern.ch/wwwasdoc/minuit/minmain.html.

[72] N.B. Balabanov, K.A. Peterson, *J. Chem. Phys.* **119**, 23, (2003).

[73] H. Braune, S. Knoke, *Z. Phys. Chem. Abt. B* **23**, 163, (1933).

[74] A. H.Gregg, G. C. Hampson, G. I. Jenkins, P. L. F. Jones, L. E. Sutton, *Trans. Faraday Soc.* **33**, 852, (1937).

[75] P. A. Akishin, V. P. Spiridonov, *Kristallografiya* **2**, 475, (1957).

[76] L. R. Maxwell, V. M. Mosley, *Phys. Rev.* **57**, 21, (1940).

[77] R. Z. Deyanov, K. P. Petrov, V. V. Ugarov, B. M. Shchedrin, N. G. Rambidi, *J. Struct. Chem.* **26**, 58, (1985).

[78] K. Kashiwabara, S. Konaka, and M. Kimura, *Bull. Chem. Soc. Jpn.* **46**, 410 (1973).

[79] J. Maya, *J. Chem. Phys.* **67**, 11, (1977).

[80] M. Haughney, M. Ferrario, I.R. McDonald, *J. Phys. Chem.* **91**, 4934, (1987).

[81] J. Somloi, D.J. Tannor, *J. Phys. Chem.* **99**, 493, (1995).

[82] J.S. Baskin, A.H. Zewail, *J. Phys. Chem.* **98**, 3337, (1994).

[83] R. Marshall, N. Davidson, *J. Chem. Phys.*,**21**, 2086, (1953).

[84] W.M. Kwok, C.S. Ma, A.W. Parker, D. Phillips, M. Towrie, P. Matousek, D.L. Phillips, *J. Chem. Phys.* **113**, 7471, (2000)

[85] F. Gaizer, G. Johansson, *Acta Chem. Scand.* **22**, 3013, (1968).

[86] E. Pontecorvo, "*Time-Resolved X-rays Scattering Technique: Liquid Structure Response to fs-perturbation*", Ph.D. thesis, unpublished, (2007)

[87] M. Cammarata, "*Transient species in solution: a time resolved x-ray study*", Ph.D. thesis, unpublished, (2007)

Acknowledgments

I am indebted to many people who nicely and patiently followed every step of this work during these three years, teaching me a lot and supporting me.

Of course I would like to start thanking all the ID09B group at the ESRF. First of all my supervisor, Michael Wulff, for this big opportunity of working here on such an interesting and challenging project. His striking enthusiasm for his work is definitely something that I will keep as an example.

Thanks to Qingyu Kong and Maciej Lorenc for having taken care of me since the first day I arrived on ID09, for the time, the discussions, the help, and especially thanks for the smiley, kind and friendly way in which they gave their contribution to this work.

A special acknowledgement goes to Marco Cammarata. His passion and his talent in his work are simply unquestionable. Working with him I really tried, bothering him constantly, to take advantage of all his competences and help. And I also managed, little by little, beamtime after beamtime, to find a very generous and sincere friend.

Thanks to Emanuele Pontecorvo, especially for the time spent together on the beamline and for his friendship.

Thanks to Friederike Ewald for all her support, in particular during the writing up of the thesis, for the infinite patience, the generosity in spending her time helping me, and for the careful and helpful comments to this work.

I should really thank many people from the ESRF, who helped me with their professional competences. Amongst the many I will unfortunately forget, thanks to Laurent Eybert, Laurent Claustre, Wolfgang Reichenbach. A special thank to Peter Van der Linden and Werner Schmid for the big help in designing and setting-up the cell we used in our static temperature controlled measurements.

This work is the result of many pleasant and fruitful collaborations. In particular I would like to thank Harry Ihee, TaeKyu Kim, JaeHyuk Lee, for the amount of work, for the discussions, and for their fast and always precise answers to any question.

A last, important acknowledgement to Prof. Savo Bratos and Rodolphe Vuilliemieur, for the richness of their comments.